KAM TORI FROM TWO-LINE ELEMENT SETS:
A COMPARISON TO SGP4

THESIS

Kenneth J. Stuart, Captain, USAF

AFIT-ENY-MS-17-M-293

DEPARTMENT OF THE AIR FORCE
AIR UNIVERSITY

AIR FORCE INSTITUTE OF TECHNOLOGY

Wright-Patterson Air Force Base, Ohio

DISTRIBUTION STATEMENT A.
APPROVED FOR PUBLIC RELEASE; DISTRIBUTION UNLIMITED.

AFIT-ENY-MS-17-M-293

KAM TORI FROM TWO-LINE ELEMENT SETS:
A COMPARISON TO SGP4

THESIS

Presented to the Faculty

Department of Aeronautics and Astronautics

Graduate School of Engineering and Management

Air Force Institute of Technology

Air University

Air Education and Training Command

In Partial Fulfillment of the Requirements for the

Degree of Master of Science in Astronautical Engineering

Kenneth J. Stuart, B.S., MBA

Captain, USAF

March 2017

AFIT-ENY-MS-17-M-293

KAM TORI FROM TWO-LINE ELEMENT SETS:
A COMPARISON TO SGP4

Kenneth J. Stuart, B.S., MBA
Captain, USAF

Committee Membership:

William E. Wiesel, Ph.D.
Chair

Lt Col Christopher D. Geisel, Ph.D.
Member

Capt Joshuah A. Hess, Ph.D.
Member

AFIT-ENY-MS-17-M-293

Abstract

Simplified General Perturbations 4 (SGP4), the current analytical model for daily tracking of objects in Earth orbit, provides at best kilometer-level accuracy with an average error growth of 1 to 3 kilometers per day. An improved analytical model with increased accuracy is necessary to reliably track the ever-growing number of objects in Earth orbit. This research examines if a Kolmogorov-Arnold-Moser (KAM) torus constructed from SGP4 two-line element (TLE) sets provides a more consistent orbit prediction than SGP4. One year of TLEs are processed as pseudo observations to identify the time rate of change of orbital elements for eight objects in different Earth orbits. The rates are then used to calculate torus basis frequencies, and an attempt is made to construct a torus for each test case. A least squares algorithm is implemented to fit SGP4 position vectors to the surface of the derived torus. The orbit path along the surface of the torus is compared to the orbit produced by SGP4 via a root-mean-square analysis. The results show that KAM tori basis frequencies can be extracted from TLEs, but SGP4 position vectors are not valid sources of pseudo observation data for the KAM torus analytical model with the current methodology.

To all who seek to advance knowledge and understanding, whether your domain is science, philosophy, art, or any other field of discovery, by examining the wonders of creation you reveal the mind of God.

This work is dedicated for the glory of the God of the Bible.

Table of Contents

Page

List of Figures

Figure Page

List of Tables

List of Symbols

Symbol	Definition
$\boldsymbol{a}$	curve fit coefficients vector
a	semi-major axis
B*	ballistic coefficient
$\boldsymbol{d}$	data vector
e	eccentricity
i	inclination
J	action variable
M	mean anomaly
M_0	mean anomaly at epoch
n	mean motion
$\boldsymbol{P}$	curve fit coefficients covariance matrix
$\boldsymbol{p}$	momentum vector
$\boldsymbol{Q}$	data covariance matrix
Q	angle variable
$R_\oplus$	Earth radius
$\boldsymbol{r}$	position vector
$\boldsymbol{T}$	curve fit time matrix
$\boldsymbol{t}$	time vector
t	time increment
$\boldsymbol{v}$	velocity vector

Symbol	Definition
w	torus frequency
θ_s	Greenwich mean sidereal time
$\mu_\oplus$	Earth gravitational parameter
ν	true anomaly
ρ_0	reference atmospheric density
τ	period
Ω	right ascension of the ascending node
ω	argument of perigee

List of Acronyms

Acronym	Definition
AFSPC	Air Force Space Command
CDM	Conjunction Data Message
DoD	Department of Defense
ECI	Earth-Centered Inertial
EGM96	Earth Gravitational Model 1996
GEO	Geosynchronous Orbit
GMST	Greenwich Mean Sidereal Time
GOES	Geostationary Operational Environment Satellite
GPS	Global Positioning System
GRACE	Gravity Recovery and Climate Experience
HST	Hubble Space Telescope
JFCC Space	Joint Functional Component Command for Space
JSpOC	Joint Space Operations Center
KAM	Kolmogorov-Arnold-Moser
LEO	Low Earth Orbit
MSE	Mean Square Error
NASA	National Aeronautics and Space Administration
RMSE	Root Mean Square Error
SDP4	Simplified Deep Space Perturbations 4
SGP	Simplified General Perturbations
SGP4	Simplified General Perturbations 4

Acronym	Definition
SP	Special Perturbations
SSA	Space Situational Awareness
SSN	Space Surveillance Network
TEME	True Equator Mean Equinox
TLE	Two-Line Element Set
TU	Time Units
USSTRATCOM	United States Strategic Command
UTC	Coordinated Universal Time
WGS 84	World Geodetic Survey 84

KAM TORI FROM TWO-LINE ELEMENT SETS:
A COMPARISON TO SGP4

I. Introduction

Motivation

Reasonable decisions are informed by relevant and accurate data. A decision to act requires actionable data. In most situations, a leader presented with a 1-in-10,000 chance that a risk will occur is unlikely to take any action to further mitigate that risk. Yet, in mitigating spacecraft conjunctions, a 1-in-10,000 chance is considered a high probability of collision. The National Aeronautics and Space Administration (NASA), for example, always maneuvers crewed space vehicles when the collision probability for the space vehicle exceeds 1 chance in 10,000 (25; 26:14).

Conjunction predictions between Earth-orbiting objects utilize covariance matrices to characterize the positional uncertainty of the objects in space and time. Typical uncertainty ranges from hundreds of meters to several kilometers. A predicted close approach distance of 0 meters—i.e., a direct collision—between two satellites with 1 square meter cross sections each and a positional uncertainty of 1 kilometer provides less than a 1-in-1,000,000 chance the objects will actually collide. Avoiding a possible collision is not as simple as just performing a maneuver. Spacecraft operators must also consider the reduced lifetime caused by expending propellant to maneuver and the amount of time the spacecraft will need to be offline until it can maneuver back to the nominal orbit. When faced with the consequences of performing an avoidance maneuver, 1 chance in 1,000,000 is not worth the loss in operation time and mission life.

The uncertainty in orbital position predictions stems from multiple sources, primarily fluctuations of the atmosphere, excluded gravitational perturbation terms in the dynamics model, and the intrinsic uncertainty in measurement data from radar and optical tracking equipment (23:1109). The primary orbit propagation model, Simplified General Perturbations 4 (SGP4), is known to provide, at best, kilometer-level accuracy with average error growth of 1 to 3 kilometers per day (33:30). In short, space operators simply do not currently have access to actionable information.

The commander of United States Strategic Command (USSTRATCOM) is directly responsible for space control and space surveillance. This Joint Functional Component Command for Space (JFCC Space) conducts this aspect of the USSTRATCOM mission, known as space situational awareness (SSA). One key element of SSA is to protect space capabilities, both from hostile attacks and orbit collisions. The Joint Space Operations Center (JSpOC), one of three operation centers within JFCC Space, performs SSA by operating the Space Surveillance Network (SSN) to detect, identify, and track objects in Earth orbit (17).

As of 2015, 11 nations have space launch capabilities and over 170 countries have access to assets in space (10). The JSpOC tracks over 23,000 objects in Earth orbit and the number of objects continues to grow every year. As the commanders of the aforementioned organizations say, space is increasingly becoming more congested, contested, and competitive (10; 11; 17; 36). Space-based capabilities are an indispensable component to military and civilian operations around the world. The United States in particular depends heavily on space assets both to maintain military superiority and to operate many civil and commercial aspects of the economy.

With such a critical dependence on space capabilities, protecting space-based assets from damage is of significant importance to the United States. The possibility of collision between Earth-orbiting objects is one of the primary threats to space assets. A collision would not only destroy an operational satellite, it would also create a significant amount of debris. The fragmented debris produced by one collision then greatly increases the probability of future collisions, potentially leading to the Kessler scenario in which the rate of collisions increases exponentially, culminating in a debris belt around Earth that renders one or more orbit regimes unusable (20).

In addition to detecting and tracking objects in Earth orbit, the JSpOC also identifies potential orbital collisions. The JSpOC utilizes two types of propagators to determine the predicted future location of orbiting objects: an analytical general perturbation propagator that can provide a position vector at any future time with one calculation and a numerical special perturbation propagator that is more accurate but must calculate several hundred or thousand positions between the current time and the future time of interest.

Position data of all cataloged objects is propagated forward in time with SGP4, the analytical propagator. Any detected close approaches—a miss distance of 1 kilometer for low Earth orbits (LEO) and 5 kilometers for geosynchronous[1] orbits (GEO)—are then

---

[1] The term GEO is used throughout this document to indicate low eccentricity orbits, regardless of inclination, with an orbital period equal or nearly equal to one sidereal day.

passed to Special Perturbations (SP), the numerical propagator (36). SP produces a more accurate position estimation than SGP4 and includes a covariance matrix, but the propagation process takes significantly more computation time than the analytical model. The details of a potential collision are then issued to spacecraft operators via a Conjunction Data Message (CDM).

The JSpOC issued 671,727 CDMs in 2014, resulting in 121 collision avoidance maneuvers (10; 24:2). The following year saw 1.2 million warnings and 148 avoidance maneuvers (11). If one assumed conservatively that those maneuvers would have resulted in a collision if a maneuver were not performed, then this means that less than 0.02% of predicted conjunctions would actually result in a collision, or that over 99% of CDMs are false-positive warnings.

Although more accurate than SGP4, SP still maintains simplifications in order to reduce computation time (26). Implementation of a high-fidelity numerical integrator is infeasible given the large quantity of objects in Earth orbit and the number of predicted close approaches, yet a higher fidelity model is clearly necessary in order to reduce the false-positive collision warnings. Less orbits would need to be analyzed if the initial close approach estimate were more accurate. Time spent analyzing meaningful conjunction possibilities could then increase, allowing for higher fidelity numerical integration.

Problem Statement

Given the continual increase in space launches and the expected growth of the satellite catalog by an order of magnitude when the upcoming Space Fence system is activated, there exists a clear need for a fast and accurate analytical method of orbit propagation (10; 30). There are simply too many objects in space to perform special perturbation predictions for each object. The quantity of close approaches predicted by SGP4 already exceeds the capability of SP to perform an appropriately detailed analysis for each close approach. Numerical analysis cannot sustain the current rate of false positive conjunction predictions with the forecasted growth of the satellite catalog.

Higher fidelity special perturbation propagators could be implemented if the number of predicted close approaches were lessened, resulting in a significantly lower rate of false positive conjunction predictions. A fast analytical model with increased accuracy and reduced error growth over time is necessary in order to minimize the number of predicted close approaches and identify possible conjunctions with a reasonable probability of occurrence. An improved analytical propagator that could provide position estimates with errors on the order of hundreds of meters or less, instead of the thousands of meters currently achieved by SGP4, is necessary.

Research Objective

Kolmogorov, Arnold, and Moser introduced and verified a theory that the path traced by the solution to a nearly-integrable system lies on the surface of an invariant—albeit deformed—torus, known now as a KAM torus. This research examines whether or not the KAM torus orbit model can utilize SGP4 data to provide a better analytical orbit determination than SGP4. Specifically, this research aims to determine if the two-line element (TLE) sets produced by SGP4 can be used as pseudo observation data to generate a KAM torus model of the orbit capable of predicting the future position of the object more consistently than SGP4 and for a longer period of time into the future. In order to perform this comparison, this research addresses the following questions:

1. How do the position predictions of SGP4 from one TLE diverge from the position predictions of subsequent TLEs?
2. How do the position predictions of a reference orbit on a KAM torus diverge if the orbit is not updated with additional observation data?
3. How do the position predictions of a KAM torus orbit model differ from the position predictions of SGP4?

If the results show that the torus position predictions are more consistent than the SGP4 position predictions, then this research will indicate that TLEs can be utilized as pseudo observation data for the KAM torus model. This result would also indicate that the torus model requires fewer updates than SGP4 and possibly provides better accuracy, though the exact accuracy of the orbit prediction cannot be determined by the work of this research alone. If the results instead show that SGP4 position predictions are more consistent than the torus predictions, then this research will indicate that TLEs may not be a useful source of data for the KAM torus orbit model.

Research Approach

This effort utilizes three software packages to achieve the research objectives. The first software package, developed by Wiesel (41), builds a KAM torus model of an orbit that includes air drag, eccentricity, and gravitational perturbations. The gravitational perturbations include zonal, sectoral, tesseral harmonics of the geopotential through an order and degree specified by the user. The software accepts orbit period and inclination as inputs to specify an orbit with desired torus basis frequencies. The second package is the publically available SGP4 code compiled and released by Vallado (32). The software package accepts TLEs as inputs in order to output position and velocity vectors at a user-defined time before or after the TLE epoch. The final software package, also developed by Wiesel, performs a least squares fit to match position vectors to the surface of a KAM torus with minimal residuals. This software outputs a state vector that specifies an epoch time, perturbations to the torus action variables, angle variables that define a position on the surface of the torus, and a ballistic coefficient that averages the effects of air drag over the timespan of the input position vectors.

This research makes the following assumptions in order to achieve the research objectives. First, the publicly available version of SGP4 released by Vallado is assumed to be a close enough representation of the Air Force Space Command (AFSPC) classified version. Significant documentation is included with this public version of SGP4 to validate the accuracy of the software, yet no comparison is available to determine how closely it resembles the classified operational version. Second, this research assumes that a TLE released less than 1 hour after the preceding TLE indicates an update to the previous TLE. TLEs are generally released several hours or days apart, but on occasion two sequential TLEs will be released with identical or nearly identical epoch dates. The other elements all differ when this occurs, thus the two TLEs cannot both be valid. Finally, this research assumes TLEs are statistically independent and equally reliable. This assumption provides a covariance matrix equal to the identity matrix when using TLEs as pseudo observation data. Although the covariance matrix for TLEs is known to not be equal to the identity matrix, the true covariance cannot be known because the true accuracy of the measurement data is unknown. The identity matrix is the best guess for the unknown covariance matrix.

Thesis Overview

This document contains five chapters. This first chapter provided motivation for and an overview of this research. Chapter I has also outlined how this research will be performed, provided the assumptions of this research, and summarized the possible outcomes that can be drawn from the results. Chapter II expands upon the concepts presented in Chapter I and provides the operational, theoretical, and mathematical background necessary to understand the current methods utilized to track Earth-orbiting objects. Chapter II also presents as a summary of similar research and the intended contributions of this research. Chapter III details the methodology and process performed to acquire data and answer the research questions posed in Chapter I. Chapter IV presents and discusses the results of the procedure outlined in Chapter III for one of the eight test cases and concludes with a summary of the overall results of this research effort. Chapter V answers the questions posed in Chapter I, presents suggestions for future study, and summarizes the conclusions drawn from this research. The appendices contain source code for the custom MATLAB[2] scripts written in support of this research as well as the results for the additional seven test cases that are not presented in Chapter IV.

---

[2] MATLAB is a registered trademark of The MathWorks, Inc. MATLAB release R2015b was used for this research.

II. Background

Space Surveillance Network

The SSN has been tasked to actively detect and track objects in Earth orbit since 1957. Of the approximately 23,000 cataloged objects currently tracked by the SSN, only about 5 percent are active satellites; the remaining 95 percent are inactive satellites, rocket bodies, and debris (31). The network is capable of tracking objects 5 centimeters across or larger in LEO and 1 meter across in GEO (25). The Department of Defense (DoD) and NASA estimate an additional one million pieces of debris too small to be tracked by the SSN are currently in orbit around Earth. The upcoming Space Fence system will provide the ability to track objects 2 centimeters across and larger. The number of cataloged objects is expected to increase astronomically the day the Space Fence is activated, growing to over 200,000 objects (10; 30).

The SSN operates via a worldwide network of 30 radar and optical sensors positioned both on Earth and in orbit (31). Due to the limited number of sensors in comparison to the quantity of orbital objects, the SSN is incapable of simultaneously tracking every object in real time. Instead, the network combines a predictive technique with observation data to periodically track each object. Past observations are propagated forward in time via the SGP4 dynamics model, and the SSN looks for the objects at the predicted future locations. The SSN sensors perform approximately 400,000 total observations each day and the JSpOC must correlate the observations to the predicted positions of cataloged objects.

Orbit Propagation Models

Although the orbital dynamicists in the late 1950s and early 1960s knew of the effects due to the nonhomogeneity of Earth, atmospheric drag, and other perturbations that affect an orbit, computers of that era were incapable of incorporating such perturbations into the calculations necessary to integrate trajectories for all objects in Earth orbit. The most computationally powerful computer in 1958 required as little as 15 minutes and as much as several hours to update a single orbit with a simplified second-order special perturbation model (16:175). An analytical orbit prediction model was necessary in order to maintain what would soon become a vast catalog of Earth-orbiting objects.

Two Body Problem.

Kepler's three laws of planetary motion, and Newton's later mathematical derivation of those laws, provide the fundamental analytical model of periodic orbits. The two-body solution[3] results in the six classical orbital elements, which together completely define a periodic orbit:

a	semi-major axis
e	eccentricity
i	inclination
Ω	right ascension of the ascending node
ω	argument of perigee
ν	true anomaly

---

[3] See Vallado (32) or other introductory astrodynamics texts for additional information on and the derivation of the two-body solution.

Figure 1 shows four of the six classical orbital elements. The two elements missing in Figure 1 are the semi-major axis and eccentricity, which together define the shape of the orbit. The classical orbital elements can be transformed to Earth-centered inertial position and velocity vectors and vice versa. In this solution, all elements are constant save the true anomaly, which continually increases with time. An additional parameter, M, the mean anomaly, can be used in place of the true anomaly to described where the satellite is in its orbit relative to perigee. One benefit of the mean anomaly is that it increases at a constant rate, n, the mean motion, whereas the rate of the true anomaly is dependent on the position of the satellite in the orbit.

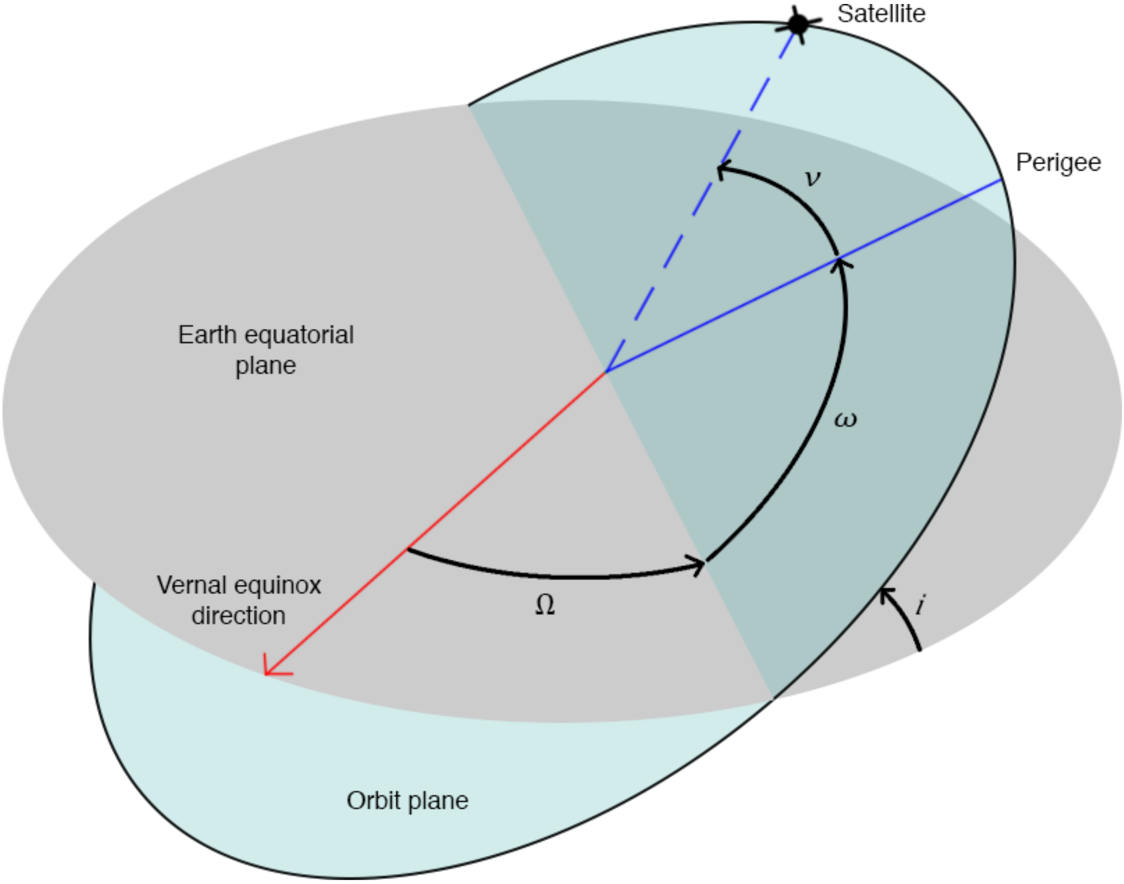

Figure 1. Classical Orbital Elements Angles

The classical orbital elements have some distinct disadvantages. The argument of perigee and true anomaly become undefined for circular orbits, and the right ascension of the ascending node is undefined for zero inclination orbits. These shortcomings can be overcome by transforming to a different coordinate system, such as the equinoctial elements, but one flaw of the two-body solution cannot be overcome: the equations of motion in the solution fail to account for any perturbations on an orbit. The lack of perturbations makes the two-body solution unacceptable for real-world application to satellite tracking.

Gravitational Perturbations.

The oblate spheroidal shape and non-homogenous mass distribution of Earth causes a non-uniform gravitational field. The gravitational acceleration at any point on or above the surface of Earth is expressed as a geopotential function. Wiesel (38:91) presents an expansion of the geopotential in spherical harmonics as

$$V(r,\theta,\varphi) = -\frac{\mu_\oplus}{r}\sum_{n=0}^{\infty}\sum_{m=0}^{n}\left(\frac{r}{R_\oplus}\right)^{-n} P_n^m(\cos\theta)[C_{nm}\cos(m\varphi) + S_{nm}\sin(m\varphi)] \qquad (1)$$

where r is the distance from the center of Earth to the point of interest, θ is the latitude, φ is the east longitude, $\mu_\oplus$ is the gravitational parameter of Earth, $R_\oplus$ is the radius of Earth, $P_n^m(\cos\theta)$ are Legendre polynomials in $\cos\theta$, and the coefficients C_{nm} and S_{nm} are dimensionless coefficients that specify the shape of the gravitational field. The values of

n and m specify the order and degree of a term in the geopotential, respectively. A set of values for C_{nm} and S_{nm} is called a gravitational model[4].

The terms in the geopotential of degree $m = 0$ are called zonal harmonics and depend solely on the latitude of an object. The first nonzero zonal harmonic is the J_2 term, which is three orders of magnitude smaller than the Newtonian point mass gravitation and three orders of magnitude larger than the J_3 and J_4 terms. The effects of the zonal harmonics are small but noticeable, and higher order zonal terms rapidly diminish as the distance from Earth increases (38:96). Terms with equal order and degree, $n = m$, are called sectoral harmonics and depend solely on the longitude of an object. The largest sectoral harmonics, C_{22} and S_{22}, are on the order of 10^{-6}, or about the same order of magnitude as J_3 and J_4. Finally, terms of degree $m \neq 0$ and order $n \neq m$ are called tesseral harmonics. These terms are dependent on both latitude and longitude. The largest tesseral harmonic terms are again roughly the same order of magnitude as J_3 and J_4, but their effect on an object rapidly decrease with only a slight increase in distance from Earth.

Wiesel (38:119) also demonstrates how gravitational perturbations due to Earth's oblateness, the J_2 term, affect the two-body solution. The non-periodic disturbances due to J_2 cause the right ascension of the ascending node, argument of perigee, and mean anomaly at epoch, M_0, to change at the constant rates

$$\dot{\Omega} = -\frac{3nJ_2{R_\oplus}^2}{2a^2(1-e^2)^2}\cos i \tag{2}$$

---

[4] This research utilizes the World Geodetic Survey 84 (WGS 84) gravitational model through order 4 and degree 0 for implementation of SGP4. All other applications in this research utilize Earth Gravitational Model 1996 (EGM96) through order and degree 20.

$$\dot{\omega} = -\frac{3nJ_2R_{\oplus} \quad {}_{\oplus}{}^{2}}{2a^2(1-e^2)^2}\left(\frac{5}{2}\sin^2(i) - 2\right) \tag{3}$$

$$\dot{M}_0 = -\frac{3nJ_2{R_{\oplus}}^2}{2a^2(1-e^2)^{1.5}}\left(\frac{3}{2}\sin^2(i) - 2\right) \tag{4}$$

The remaining two-body orbital elements are constants when periodic disturbances are excluded, therefore Equations (2)-(4) can be integrated with respect to time in order to solve for the right ascension of the ascending node, argument of perigee, and mean anomaly at any point in time as

$$\Omega = \Omega_0 + \dot{\Omega}t \tag{5}$$

$$\omega = \omega_0 + \dot{\omega}t \tag{6}$$

$$M = M_0 + \left(n + \dot{M}_0\right)t \tag{7}$$

where M_0 indicates an initial known value of mean anomaly at some epoch time and t is the time elapsed since that known condition.

These equations can also reveal some other information specific to the perturbations caused by Earth's oblateness. Equation (3), for example, reveals the critical inclination, i.e., the orbit inclination at which Earth's oblateness will not cause the location of perigee to change within the orbit plane. The value of $\dot{\omega}$ equals zero when the inclination is approximately 63.435 or 116.565 degrees.

History of Orbit Propagators.

Dynamicists developed several different analytical theories in the 1950s to include the geopotential in the solution for motion of an object in Earth orbit. The majority of solutions revolved around adding perturbations to the two-body solution. Four noteworthy solutions were developed by Vinti, Kolmogorov, Brouwer, and Kozai to partially account for the influence of zonal harmonics.

Vinti Solution.

Vinti approximated drag-free motion of a satellite under the influence of the second-, third-, and partial fourth-order zonal harmonics. Unlike many other solutions available at this time, Vinti's solution had no singularities for small eccentricity, zero inclination, or critical inclination orbits; however, Vinti's solution was difficult to formulate due to the need to compute elliptical integrals in an oblate spheroidal coordinate system (34). This difficulty may be the reason Vinti's solution has remained virtually unutilized for decades. Despite the notoriety, Vinti continued to extend his solution through the late 1900s to incorporate additional perturbation forces. Vinti's efforts are documented in his published textbook (35).

Kolmogorov Solution.

Another relatively unutilized model for satellite motion in Earth orbit is the KAM torus. The solutions to integrable Hamiltonian systems[5]—i.e., systems with a number of constants of motion equal to the number of degrees of freedom—lie on the surfaces of invariant tori in the phase space. Kolmogorov published a theory in 1954 that stated what happens to the solutions of integrable systems when subjected to small perturbations, thereby rendering the systems non-integrable. Kolmogorov's theory postulated that the solutions for a nearly-integrable system also lie on the surfaces of invariant yet deformed tori that are near the tori solutions of the integrable system. Arnold and Moser provided

---

[5] See Greenwood (14) or other analytical dynamics texts for a description of Hamiltonian systems and their solutions.

additional proofs of Kolmogorov's theory in the early 1960s, hence the name Kolmogorov-Arnold-Moser (KAM) torus. Additional research efforts have provided further mathematical and numerical proofs for the KAM theorem and are documented by Celletti and Chierchia (4). Wiesel has also shown that the KAM torus is the exact solution for objects in Earth orbit subjected to the geopotential (38:202).

Action-angle variables best describe the path along the surface of a torus. The action variables are constants that designate the spatial dimensions of the torus in the phase space. The angle variables increment linearly in time and designate the trajectory along the surface of the torus. A trajectory with angular rates that are integer multiples of each other results in periodic motion on the surface of the torus, i.e., the trajectory retraces the same path indefinitely. For a trajectory with non-commensurate angular rates, the trajectory will never retrace the same path twice, but the trajectory will eventually pass arbitrarily close to every point on the torus. Both periodic and quasi-periodic phase trajectories lie on the surfaces of N-dimensional tori in a 2N-dimensional phase space, where N is the number of independent coordinates (28:212-303). The dimension of the torus specifies the degrees of freedom, e.g., a 2-dimensional torus in a 4-dimensional phase space has two degrees of freedom.

Figure 2 (a) shows an example 1-dimensional torus. Figure 2 (b) and (c) show a 2-dimensional torus from a top-down view and cross-sectional view, respectively. In both examples, J are the action variables and Q are the angle variables. Phase trajectories for the solutions to an integrable system lie on the surfaces of actual tori in the phase space, such as those shown in Figure 2; deformations to the tori occur only when a system is subjected to small perturbations and rendered non-integrable. Both integrable and non-integrable systems may have multiple tori solutions dependent on the initial conditions of the system.

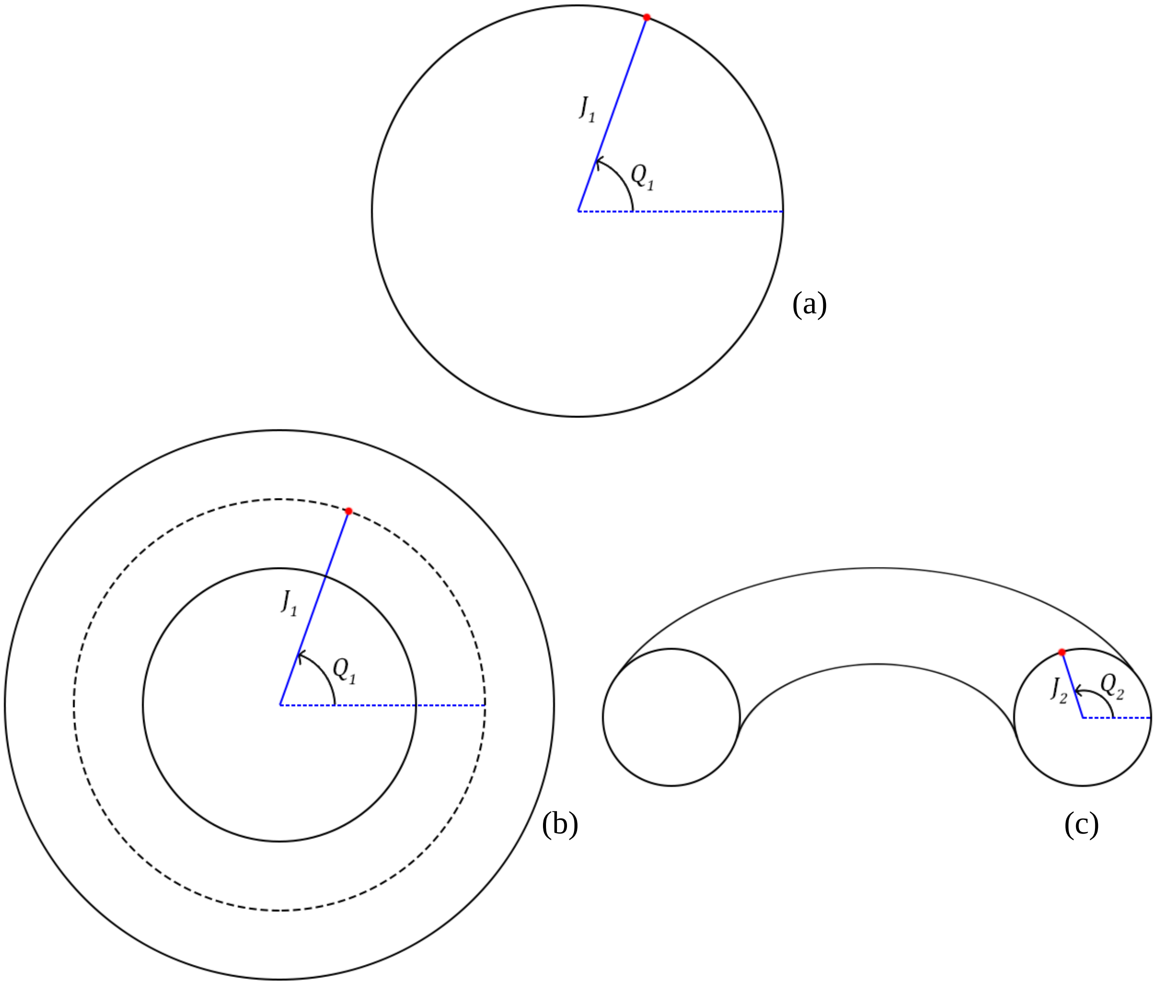

Figure 2. Example of 1-Dimensional and 2-Dimensional Tori

KAM theorem explains the effects of small perturbations on integrable systems. The small perturbations cause the system to become non-integrable, but the system does remain nearly integrable with solutions that are near the solutions of the integrable system. When an integrable system is subjected to perturbations, the periodic tori trajectories of the integrable system are usually rendered invalid but the tori of quasi-periodic trajectories persist with deformation to the tori actions (38:193). In the case of the periodic solutions, the resonances may lead to perturbations that potentially do not remain small, which violates the underlying premise of KAM theorem that states the system must be subject to small perturbations. For the non-resonant solutions of an integrable system subjected to perturbations, most of the tori solutions are preserved and the new solutions for the non-integrable system may show either periodic or quasi-periodic motion on the surfaces of deformed tori (7:416-417).

Brouwer and Kozai Solutions.

Both Brouwer's and Kozai's solutions modeled drag-free motion under the influence of zonal harmonics J_2, J_3, J_4, and J_5 as a function of mean orbital elements and time (32:692-696). Both of these solutions had singularities for circular orbits, zero inclination orbits, and orbits near the critical inclination. Despite the singularities, these models, particularly Brouwer's solution, became the foundation for most space surveillance systems in the United States (16:175).

Updates to analytical orbital theory over the subsequent few decades primarily consisted of modifying the Brouwer and Kozai solutions. In 1961, Brouwer and Hori incorporated atmospheric drag with a static exponential representation of the atmosphere (16:175). The United States Air Force's initial general perturbations model, Simplified General Perturbations (SGP), was based on a modified version of Brouwer's and Kozai's solutions and included an empirical atmospheric model but excluded terms that caused singularities due to eccentricity. By 1964, SGP had become the predominant prediction model for satellite tracking sites around the world (16:176).

Lyddane (22) performed a change of variables in 1963 to remove the singularities in SGP for zero eccentricity and zero inclination orbits. Lane and Crawford developed an improved analytical atmospheric density model in 1969; however, the computers of that time proved incapable of managing the number of terms in the atmospheric model for all of the satellites in the catalog (16:176).

Simplifications to SGP were implemented in 1970 to balance the growing number of satellites with the limited capability of computers, resulting in SGP4. Lyddanne's work to remove singularities and a simplified version of the Lane and Crawford atmospheric model were incorporated into SGP4 (16:176). The gravitational model was likewise shortened for SGP4 to retain only periodic terms that lacked eccentricity as a factor.

Whereas SGP approximated atmospheric drag via the rate of change of mean motion, the newer SGP4 encapsulated the secular effects of drag in a single term as a quadratic function in time. The SGP4 ballistic coefficient, B*, relates to the aerodynamic ballistic coefficient by

$$B^* = \frac{B\rho_0}{2} \tag{8}$$

where ρ_0 is a reference value for atmospheric density and $B = C_D A/m$, the traditional definition for the aerodynamic ballistic coefficient in terms of drag coefficient, C_D; cross-sectional area, A; and mass, m (18). The simplified model of the ballistic coefficient in SGP4 inadvertently captures other forcing effects not modeled by SGP4, sometimes resulting in a negative value that erroneously indicates energy added to the system (33).

The Soviets launched Molniya-1, the first highly eccentric satellite with a 12-hour period, in 1965. Soon after, the United States space community realized that a new general perturbations model that accounted for third body gravitation and additional Earth gravitational harmonics was necessary for this class of orbit. Bowman modeled lunar and solar gravity as well as partial resonance effects of Earth tesseral harmonics in 1967. By 1977, Hujsak managed to incorporate a first-order model of Bowman’s work into an updated model for both near-Earth and geosynchronous satellites (16:176). This model became Simplified Deep Space Perturbations 4 (SDP4) and is utilized for satellites with a period greater than 225 minutes, which corresponds to an altitude of 5,877 kilometers for circular orbits.

Over the next few years, many users of SGP4 and SDP4 incorporated their own customizations. Hoots and Roehrich released Spacetrack Report No. 3 in 1980 in an effort to synchronize code implementation among all users. The report did not include equations but did contain source code for the propagation models. The user community adopted this first public release of SGP4 and SDP4, but the community again made subsequent refinements with little documentation of changes. NASA released a version of the code worldwide in 1990, at which point SGP4 and SDP4 were merged into a single model referred to as just SGP4 (33:2).

Hoots published a technical information package on SGP4 in 1998 that outlined the history of the equations. In 2004, Hoots et al. (16) published complete documentation of all equations to incorporate resonances, third-body forces, drag, and other perturbations in SGP4. This release appears to have standardized SGP4 for all users as no subsequent updates have been publically documented.

Current Orbit Perturbation Models.

The JSpOC operates with two orbit propagators: SGP4 and SP. SGP4 propagates orbits for all tracked objects and, if a close approach is detected, SP performs a higher fidelity propagation. Table 1 lists some key features and differences of SGP4 and SP.

Table 1. Comparison of SGP4 and SP Propagation Models

Perturbation Feature	SGP4	SP
Atmospheric drag	Simplified analytic model	Empirical model
Solar radiation pressure	Not included	Constant reflectivity model
Earth tidal motion	Not included	Low-order model
Earth gravity	Low-degree zonal only	Through degree and order 36
Third body gravity	Semi-analytic model	Ephemerides model
Error estimation	Not distributed	Covariance propagation

General perturbation propagation methods produce orbit predictions that are qualitatively accurate over long periods of time whereas special perturbation propagation methods produce orbit predictions that are quantitatively accurate over short time periods. Numerical integration requires significantly more time to compute a prediction and is thus reserved only for detailed analysis of orbits rather than daily propagation.

The National Research Council (26:32-33) emphasized the importance of maintaining efficient analytic orbit propagators in 2012, yet little effort has been made since the late 1990s to update the analytical solutions; instead, efforts have focused primarily on improving accuracy and speed of numerical integration models in order to capitalize on the availability of faster computer processors. The constant increase of objects in Earth orbit makes an accurate general perturbations model vitally important for tracking the objects and predicting collisions with a reasonable level of accuracy, yet SGP4 has not received a software or hardware update for over 20 years despite modern advancements in astrodynamics systems research (26:46).

Two-Line Element Sets

The JSpOC publishes TLEs to report SSN observation and tracking data. The values reported in a TLE represent the mean values of many observations calculated to fit the SGP4 dynamic model (19). The JSpOC issues new TLEs as needed rather than on a set schedule. Objects with the ability to maneuver and objects in LEO where atmospheric drag is significant will have TLEs updated more frequently than non-maneuvering objects or objects in GEO. In general, the JSpOC releases a new TLE when the position predicted by SGP4 based on the current element set differs by 5 kilometers or more from the predicted position of a new element set based on recent observations.

A TLE consists of two 69-character lines of alpha numeric values. Figure 3 shows a TLE with an epoch date of 1 January 2016 for the Hubble Space Telescope and identifies the content of each field. The subsequent paragraph provides additional detail for clarity. See Kelso (18) for a further description of each field with significant detail.

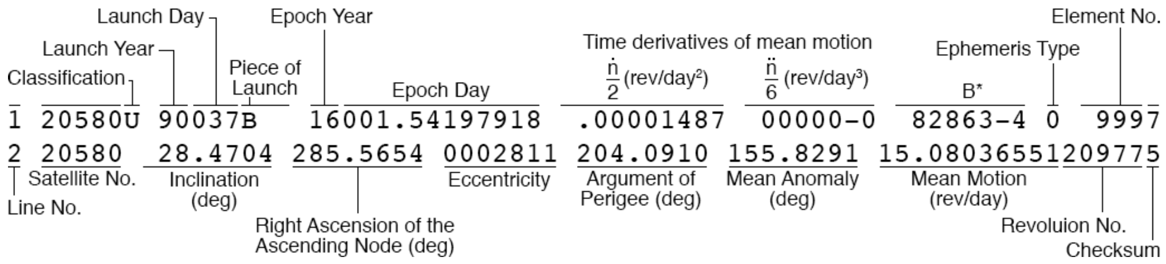

Figure 3. Hubble Space Telescope Two-Line Element Set

The epoch year and day increment at midnight in Coordinated Universal Time (UTC). An epoch of 16001.50000000 corresponds to 2016 January 1 12:00:00.000. Units of days are reported as 24-hour days rather than sidereal days. The final two characters in the second derivative of mean motion and B* indicate an applicable power of 10. In the B* value of Figure 3, for example, the -4 corresponds to 10^{-4}. The true value of B* is unknown for objects in orbit; instead the dynamics model adjusts the B* term as necessary to account for non-linear changes in mean anomaly. B* has units of inverse Earth radii. The second derivative of mean motion, B*, and eccentricity all have an assumed leading decimal before the first digit. The orbit revolution number normally increments each time the object passes the ascending node in orbit; however, the value occasionally does not increment correctly, erroneously failing to increment.

The TLE format arbitrarily limits the precision of the data. An ideal format would report a number of digits in the output equal to the number of digits used to calculate the data in order to minimize precision loss. The eight digits after the decimal in the epoch day allow for precision within 4.32×10^{-4} seconds. At an orbital speed in LEO of 7.6 kilometers per second, a satellite will travel approximately 4 meters in that time. The seven decimal places in eccentricity limit position of a satellite in GEO to approximately 2 meters. The four decimal places in argument of perigee and mean anomaly create uncertainty of 6 meters at LEO and 35 meters at GEO (32:108).

In addition to the loss of precision, the method to generate TLEs and report orbit data compounds errors into the reported values. The raw observation data includes inaccuracies dependent on the type and location of the sensor used to record the observation while the SGP4 dynamics model incorporates numerous simplifications in order to ease computational requirements. These errors vary for each observation and each generation of a new TLE, thus each TLE has a different yet unknown level of accuracy. No known method exists to report the independent accuracy of each TLE released by the JSpOC; however, TLE data from SGP4 is, on average, accurate to approximately 1 kilometer at the TLE epoch with average error growth of 3 kilometers per day (33:30).

Conjunction Assessment

The CDM is an international standardized format to exchange spacecraft conjunction information between the agency that detects a possible conjunction and the satellite operator. The JSpOC issues a CDM to satellite operators when an on-orbit collision is detected between an active satellite and any other object in orbit. The CDM replaced the conjunction summary message in 2014 following recommendations from the National Research Council and the Consultative Committee for Space Data Systems.

The CDM consists of a number of mandatory fields and allows for several optional fields to be populated depending on the amount of data available. Among the mandatory fields are the identification of the two objects that are predicted to collide, the predicted time of conjunction, the predicted close approach distance, the current position and velocity vectors of each object, and the covariance matrix for each object (5). This information allows the spacecraft operators to independently calculate a probability of collision and determine whether or not to maneuver.

Related Research

Research into Vinti's solution shows that it is more accurate and less computationally intensive than Brouwer's and Kozai's methods (2). Vinti's solution can also be used in semi-analytic computations—i.e., a mixture of numerical and analytical techniques—to produce results with greater accuracy than SGP4 in the same or less time (42). This and similar research into other analytical and semi-analytical propagators identifies possible areas for improvement in how the JSpOC predicts future positions for objects in the satellite catalog.

Other research has examined the consistency and uncertainty of TLEs. Osweiler (27) found that TLEs displayed minor positive correlation to their immediate predecessors, indicating a consistency in the position predictions between subsequent TLEs. As expected, the correlation decreases over time. The correlation also decreases for objects in LEO where atmospheric and gravitational perturbations are more prevalent.

Flohrer, Krag, and Klinkrad (12) compared TLEs to high-accuracy ephemerides data to estimate the intrinsic uncertainties of TLEs. They found that TLEs for objects in orbits with high eccentricity will have greater uncertainty than TLEs for objects in low eccentricity orbits. Additionally, for non-circular orbits, TLEs for objects in low inclination orbits tended to have greater uncertainty than those for objects in higher inclination orbits.

KAM Theorem.

Much research effort has examined the application of KAM theorem on celestial bodies, but little research has examined the practical application for Earth satellite motion. Wiesel identified an exact KAM tori periodic orbit solution for Earth orbits utilizing the zonal harmonic subset of the geopotential. Much like the two-body solution, sectoral and tesseral harmonics, air drag, and other forces can be included in the model as perturbations from the periodic orbit. Expressed in an Earth-centered, Earth-fixed reference frame, the orbit plane of the periodic solution will precess at a rate that is unknown until the orbit has been constructed; therefore, the orbit must be defined in an Earth-centered inertial reference frame. In order to achieve a periodic orbit, the orbit must satisfy the function

$$\boldsymbol{G} = \begin{Bmatrix} z(\tau) \\ \boldsymbol{r}(\tau) \cdot \boldsymbol{p}(\tau) - x_0 \dot{x}_0 \\ \boldsymbol{r}(\tau) \cdot \boldsymbol{r}(\tau) - {x_0}^2 \end{Bmatrix} = \boldsymbol{0} \tag{9}$$

where $z(t)$ is the z-component of the Cartesian position vector, $\boldsymbol{r}(t)$ is the Cartesian position vector as a function of time, $\boldsymbol{p}(t)$ is the Hamiltonian momentum vector as a function of time, x_0 is the initial position at time zero, $\dot{x}_0$ is the initial radial velocity at time zero, and τ is the orbit period.

Equation (9) specifies that the satellite must have the same radial velocity and be at the same distance from Earth at each ascending equatorial crossing. The solution to this equation is documented in Wiesel (41). The result identifies two actions and two angles that define the solution as motion on a torus, where one angular rate is the orbital frequency and the other is the inertial nodal regression rate. These variables define a single orbit on the surface of a two-dimensional torus but fail to account for motion near the periodic orbit.

The Floquet solution[6], which examines stability of motion near the periodic orbit, adds a third pair of action-angle variables, where the rate of the third angle is the apsidal precession rate. Equation (9) and the accompanying Floquet solution result in a total of six variables—three actions and three angles—that define a position and trajectory on the surface of the torus.

Most, if not all, research into KAM theorem as it applies to objects in Earth orbit appears to rely on Wiesel's solution. Wiesel demonstrated that a reference torus generated from frequencies identified with a Fourier analysis deviates from a numerically integrated orbit by only a few meters over several years of propagation (37; 40). Various research efforts have applied Wiesel's torus solution and construction algorithm to observation data, Global Positioning System (GPS) ephemeris data, and numerically integrated data, all with varying levels of success (1; 3; 6; 8; 9; 13; 15; 21; 43).

Derbis (8) attempted to extract torus frequencies from ephemeris data for GPS satellites using a Laskar frequency analysis. She compared the resulting tori to numerically integrated data and discovered inconsistent basis frequencies between those extracted from the ephemeris data and those extracted from the numerical integration. These inconsistencies ultimately prevented her from identifying a third basis frequency. She suspected the discrepancy resulted from GPS satellites residing in a resonance orbit, which results in two commensurate frequencies. Bordner (3) expanded Derbis's research and attempted to identify the third basis frequency as a libration frequency associated with the resonance orbit instead of the traditional apsidal rate. Bordner identified a third frequency,

---

[6] See Wiesel (38:15-16) for a brief introduction on Floquet Theory or Wiesel (41) for a description of Floquet Theory as it pertains to this research.

but the long period of the frequency prevented the tori from providing valid orbit fits due to the frequent maneuvers of GPS satellites.

Little (21) also implemented a frequency analysis to identify torus frequencies from ephemeris data of the Jason-1 and Gravity Recovery and Climate Experience (GRACE) satellites. Little analyzed short periods of data between maneuvers in order to identify the torus frequencies. He successfully produced a KAM torus for the Jason-1 satellite that maintained residuals under 1 kilometer for over 30 days, but he failed to generate a torus for the GRACE satellite, likely because of the prevalence of atmospheric drag in the lower-altitude orbit. Little did not examine the possibility of extending the tori solutions for either satellite to determine if the tori remained valid after maneuvers.

Other researchers have produced tori strictly from numerically integrated orbits. Craft (6) integrated orbits for hypothetical satellites orbiting in formation and generated a torus for the satellites. He found that clusters of satellites spaced 100 meters apart and positioned on the same torus maintained their formation for over 60 days with deviations on the order of millimeters, indicating that satellites placed on the same torus will maintain their formation on the surface of that torus. However, the drift between satellites was proportional to the initial separation, resulting in a worse fit for satellites that started farther apart. Satellites experiencing high atmospheric drag and satellites near the critical inclination also displayed larger deviations.

Hagen (15) examined the deviations caused by perturbations unmodeled in the torus construction algorithms. Hagen began by generating a reference torus from an integrated orbit that contained perturbations only from Earth’s geopotential. He then integrated additional orbits, one including air drag and another including third body gravitation effects. He found that air drag caused an error of 3 kilometers after 4 days while lunar gravity effects caused an error of 10 kilometers in the same period of time. Both orbits displayed quadratic growth in error. Hagen's research identified the importance of modeling perturbation forces in the torus construction routine.

Dunk (9) attempted to apply KAM theorem to highly eccentric orbits. He numerically integrated several orbits of differing eccentricity and constant perigee altitude. Dunk was able to identify torus basis frequencies and generate a torus for eccentricities up to 0.5; however, the goodness of fit decreased as eccentricity increased, resulting in larger residuals as the orbits became more elliptical.

Yates (43) attempted to combine previous research methods by using observation data in conjunction with numerical analysis. Yates numerically integrated 1 year of orbit data based on the International Space Station (ISS) reference orbit parameters and created a reference torus based on the frequencies from that orbit. He then performed a least squares analysis to update the reference torus based on NASA ISS tracking and observation data. Yates found that the reference torus resulted in unbounded quadratic growth that reached 500 kilometers after 8 days. The updated torus, however, had residuals less than 3 kilometers that remained steady until a maneuver was performed.

Frey (13) examined a different approach to produce a torus. Frey was able to avoid the long numerical integration and frequency analysis by extracting basis frequencies directly from TLEs. He performed a non-linear least squares analysis on 18 months of TLE data to identify the rate of change in mean motion, argument of perigee, and right ascension of the ascending node. Frey attempted to fit a torus to four different orbiting objects but was only successful with one test case. He suspected the failed cases were due to the inability of the torus construction algorithm to handle air drag and near-zero eccentricity. He compared the successful torus to both SGP4 and an integrated orbit with matching frequencies. The torus remained within 60 meters of the integrated orbit after 6 months of propagation but rapidly deviated from the SGP4 predictions. Frey suspected the deviation from SGP4 was due to the inherent inaccuracies of SGP4 rather than a flaw in the torus construction.

Following Frey's research, Wiesel updated the torus construction algorithms to account for near-zero eccentricity and air drag in the torus construction routine. The updated algorithms create a torus that models perturbations due to air drag, Earth's geopotential, and second order terms in eccentricity (41).

Abay (1) examined how to convert the SSN satellite catalog to KAM tori using Frey's method of basis frequency identification from TLEs and Wiesel's updated torus construction algorithm. Abay pseudo-randomly chose 1,500 test cases with altitude above 300 kilometers, not in a resonance orbit, and not in critical inclination or polar orbit. He identified torus basis frequencies for all 1,500 test cases and attempted to perform a least squares fit to align the tori with SGP4 position vectors at TLE epoch times. He had moderate success but was unable to generate tori for many maneuvering satellites and objects near a resonance, near polar or critical inclination, and objects continuously in a high atmospheric drag environment.

Contributions of Current Work

The DoD, spacecraft owners, and much of the space user community operate software that relies on the TLE format in order to function. Following the National

Research Council's (26:42) recommendation, any new system must maintain the TLE format to support legacy systems. This research aims to validate or disprove the theory that a set of TLEs can be utilized as data for an alternative analytical propagator. The research into Vinti's theory of orbital motion and KAM theorem already demonstrates the possibility to develop analytical models with greater accuracy and speed than that of SGP4. The research of both Osweiler and Flohrer et al. into the consistency of TLEs appears to indicate a possibility to utilize a large set of TLEs as data to analyze the motion of Earth-orbiting objects. This research builds upon those findings and analyzes the possibility to implement an alternative analytical model that uses the consistency of a set of TLEs to generate the input data for the KAM torus analytical orbit model.

This research aims to determine if orbit propagation via KAM tori provides greater consistency than SGP4. Unlike previous research, this work does not attempt to fit a KAM torus to precision ephemeris or numerical data and instead generates a torus solely with basis frequencies extracted from TLE data sets. This research extends the work of Frey and Abay by examining how quickly motion on a torus diverges from the reference orbit and how the torus compares to SGP4. The results of this research will not indicate an accuracy for the KAM tori but rather will indicate if the torus created from TLE data can be updated less frequently than the JSpOC currently updates TLEs.

III. Methodology

Several test cases were selected in order to compare the SGP4 propagation method to the KAM torus propagation method. Results of previous research indicate difficulties in applying KAM theorem to certain orbit regimes, specifically orbits with a period near an integer multiple of the rotational period of Earth, orbits near zero inclination or the critical inclination, and orbits with an eccentricity greater than 0.1.

This research does not examine any objects that can perform impulsive station-keeping maneuvers. Each impulsive maneuver results in a slightly different orbit for the satellite, which alters the torus. Examining transitions to nearby tori is beyond the scope of this research, thus all test objects for this research are either non-maneuvering objects or objects that operate solely with reaction wheels for attitude control.

Table 2 lists approximate values for key orbital parameters of the test objects. Note that several test cases feature properties that cause difficulties in applying KAM theorem. The Delta 11 test case, for example, has a fairly eccentric orbit. These objects were selected specifically to see where KAM theorem fails. In the order listed in Table 2, the test objects are a Thor Ablestar rocket body, two Delta 1 rocket bodies, Hubble Space Telescope (HST), Geostationary Operational Environment Satellite (GOES) 9, two Russian rocket bodies, and a large piece of Iridium 33 debris. Each test case utilizes 1 year of TLE data from the year indicated in the rightmost column of the table.

Table 2. Orbit Properties of Test Objects

Name	Satellite Number	Period (min)	Inclination (deg)	Perigee Altitude (km)	Apogee Altitude (km)	Eccentricity (10^{-4})	Year
Thor 293	59	106.43	28.25	921	1,202	188.9	2009
Delta 11	341	157.51	44.79	951	5,615	2414	2009
Delta 114	8133	88.10	25.28	175	186	8.386	2009
HST	20580	95.45	28.47	539	542	2.168	2010
GOES-9	23581	1,457.47	10.61	36,185	36,223	4.462	2014
SL-14	26874	90.54	82.45	297	305	5.989	2014
SL-18	29080	91.42	97.60	342	346	2.975	2014
I33 debris	33874	100.70	86.29	731	852	84.39	2014

A least squares analysis was performed to extract torus basis frequencies for each test case. Then the KAM torus software package was run to generate a torus for each test case. SGP4 was utilized to create 100 position vectors between the epoch times of each TLE. These vectors were then fitted to the surface of the torus with another least squares analysis, which resulted in a state vector that specified an epoch time, perturbations to the action variables, angle variables that defined a position on the surface of the torus at the epoch time, and a B* value that averaged the effects of air drag for the fit interval. An updated state vector of action-angle variables was produced for each subsequent set of 100 SGP4 vectors. The action-angle variables were then utilized to acquire torus position vectors with the same time steps as the SGP4 position vectors. The first TLE and the first state vector of action-angle torus variables were also propagated forward to create position vectors throughout the full timespan of the data set. Finally, these four sets of position vectors were compared in order to determine how quickly they diverged.

Reference Frames

This research utilized two reference frames for position and velocity vectors, an Earth-centered inertial (ECI) reference frame and an orbit-oriented frame. The values from TLEs and SGP4 are defined relative to the True Equator Mean Equinox (TEME) ECI reference frame, which is the inertial frame used for this research. This frame is defined relative to Earth's true rotation axis—the geographic North pole—and the mean direction of the vernal equinox. Both the direction of Earth's rotation axis and the position of the vernal equinox relative to Earth's surface shift slightly as Earth precesses, nutates, and orbits around the sun. The mean equinox direction accounts for precession but not the nutation of Earth. Defining vectors relative to the TEME reference frame ensures all vectors are defined relative to the true equator. In Cartesian coordinates, the X-axis points in the mean direction of the vernal equinox, which coincides with the intersection of the ecliptic and equatorial planes. The Z-axis is the true rotation axis of Earth. The Y-axis completes the orthonormal set, defined positive by the right-hand rule.

The second reference frame is also Earth-centered but not inertial. This reference frame is defined by the ECI position and velocity vectors of a reference object. The first axis, U, points radially in the same direction as the ECI position vector. The third axis, W, points normal to the orbit plane and is defined by the cross product $\boldsymbol{r} \times \boldsymbol{v}$, where $\boldsymbol{r}$ and $\boldsymbol{v}$ are the ECI position and velocity vectors, respectively. The second axis, V, completes the orthonormal set, defined positive by the right-hand rule. This reference frame rotates as the reference object orbits Earth. The UVW reference frame is useful for comparing position vectors in order to quantify the difference between two vectors is in the radial, in-track, and orbit normal directions.

Figure 4 portrays both reference frames relative to Earth. The red axes are included for visual clarification only and show the orientation of the UVW basis vectors as if the reference frame were centered at the satellite instead of the center of Earth.

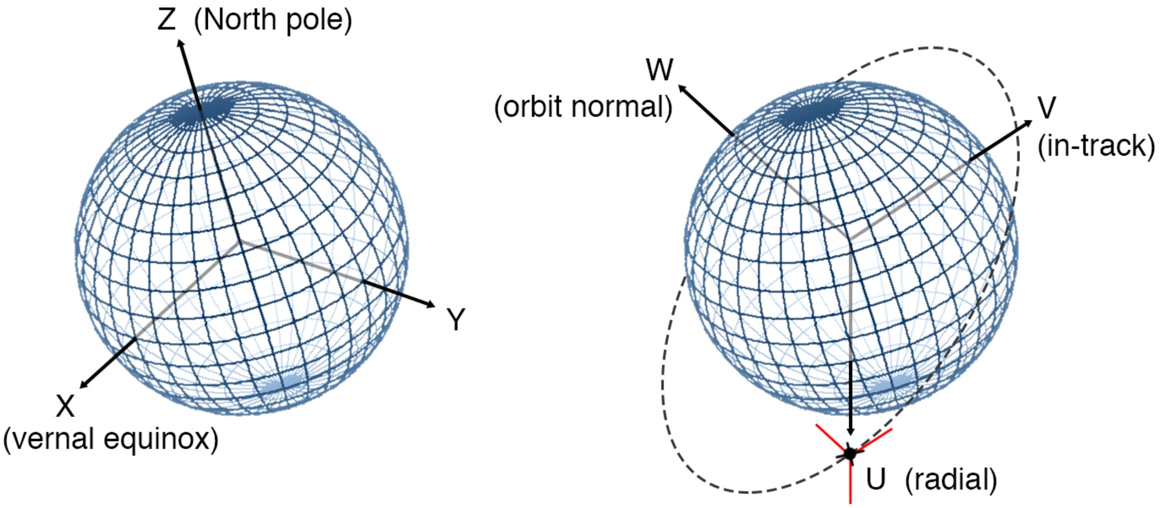

Figure 4. True Equator Mean Equinox and UVW Reference Frames

Process TLE Data

A custom MATLAB script was written to read TLE data and store the values in an array. This script is available in Appendix A. The TLEs were compared to determine if multiple TLEs were issued with the same epoch date. Any TLE issued within 1 hour of the previous TLE was assumed to be an update of the preceding TLE. In this case, the updated TLE was retained and the preceding TLE was removed from the data set.

Days and dates were converted to canonical time units (TU) and Julian dates. The duration of a TU is defined as

$$TU = \sqrt{\frac{{R_\oplus}^3}{\mu_\oplus}} \tag{10}$$

where

$R_\oplus$ = 6378137 m and

$\mu_\oplus$ = 3.986004418·10^{14} m^3/s^2, thus

$$1\,TU = 806.8111238242922\,s \tag{11}$$

All angular data was converted to radians. Absolute jumps exceeding 2π in right ascension of the ascending node, argument of perigee, and mean anomaly were adjusted to their appropriate 2π compliments, resulting in smooth angular data. However, mean anomaly cycles through 2π radians with each orbit and several orbits occur between TLE epoch times, therefore the number of revolutions was taken into account when adjusting mean anomaly to ensure the appropriate 2π compliment was used.

Frey noted that the revolution number in the TLE does not always increment correctly (13:45). He attempted to eliminate the 2π jumps in mean anomaly via

$$M(unwrapped) = M(TLE) + 2\pi \cdot (revnum) \tag{12}$$

where $M(unwrapped)$ indicates the value of M after the 2π jump has been eliminated, $M(TLE)$ is the value of mean anomaly from the TLE, and $revnum$ is the number of revolutions since the first TLE. This method resulted in non-linear curve fit residuals in excess of 20 radians for some of his test cases.

A new method was developed for this research in order to unwrap the mean anomaly values from the set of TLEs. This method assumes that the mean motion changes at an approximately quadratic rate between TLE epoch times, thus the mean anomaly at the next TLE epoch time is estimated by

$$M(i+1) = M(i) + n(i) \cdot \Delta t + \frac{\dot{n}}{2}(i) \cdot \Delta t^2 \tag{13}$$

where Δt is the time difference between the current and next TLE epochs; $M(i)$, $n(i)$, and $\dot{n}(i)/2$ are values of mean anomaly, mean motion, and first derivative of mean motion from the current TLE, respectively; and $M(i+1)$ is the expected unwrapped value of mean anomaly for the next TLE.

The mean anomaly result from Equation (12) was compared to the result from Equation (13). If the results differed by greater than 6 radians, or approximately 1 revolution, it was assumed that the revolution number in the TLE failed to increment correctly, in which case 1 revolution needed to be added to the current and all subsequent revolution numbers. Note, 6 radians was used as the error detection criterion instead of 2π radians in order to account for small changes to n and $\dot{n}$ not modeled by Equation (13). This process was repeated for every value in the array of TLE data. The correct unwrapped mean anomaly was then stored as

$$M(unwrapped) = M(TLE) + 2\pi \cdot (corrected\ revnum) \tag{14}$$

where $corrected\ revnum$ indicates the corrected number of revolutions since the first TLE. This method reduced the curve fit residuals to less than 2π radians, and in most cases reduced the residuals to less than 0.5 radians.

Identify Torus Frequencies

The first two basis frequencies for a torus, the orbital frequency and inertial nodal regression rate, are defined as

$$w_1 = \dot{M} + \dot{\omega} \tag{15}$$

$$w_2 = \dot{\Omega} \tag{16}$$

A non-linear least squares curve fit was performed to calculate the time rate of change of mean anomaly, right ascension of the ascending node, and argument of perigee. Let column vectors $\boldsymbol{d}$ and $\boldsymbol{t}$ represent the angular data to be fit and the associated epoch time of each value. The quadratic curve fit of the data is then

$$\boldsymbol{d} = a_0 + a_1\boldsymbol{t} + a_2\boldsymbol{t}^2 \tag{17}$$

where the a_i are the curve fit coefficients. The value of a_1 approximates the time rate of change of data $\boldsymbol{d}$.

Next define a n-by-3 matrix $\boldsymbol{T}$ as

$$\boldsymbol{T} = \frac{\partial \boldsymbol{d}}{\partial a_i} = \begin{bmatrix} \mathbf{1} & \boldsymbol{t} & \frac{1}{2}\boldsymbol{t}^2 \end{bmatrix} \tag{18}$$

where $\mathbf{1}$ indicates a column vector of ones with length n, and n is the length of the vectors $\boldsymbol{d}$ and $\boldsymbol{t}$.

The curve fit coefficients are then

$$\boldsymbol{a} = (\boldsymbol{T}^T\boldsymbol{Q}^{-1}\boldsymbol{T})^{-1}\,\boldsymbol{T}^T\boldsymbol{Q}^{-1}\boldsymbol{d} \tag{19}$$

where $\boldsymbol{a}$ is a 3-by-1 column vector of the coefficients a_0, a_1, and a_2 and $\boldsymbol{Q}$ is the n-by-n covariance matrix for the data. The covariance matrix, if known, provides a measure of accuracy and statistical independence for each value in the data set. However, the true covariance cannot be known from the data contained within the TLE because the true accuracy of the measurement data is unknown. Thus, it was assumed that each TLE was equally reliable and statistically independent, which gives $\boldsymbol{Q}$ as the identity matrix. Equation (19) then reduces to

$$\boldsymbol{a} = (\boldsymbol{T}^T\boldsymbol{T})^{-1}\,\boldsymbol{T}^T\boldsymbol{d} \tag{20}$$

The residuals of the curve fit are

$$\boldsymbol{r} = \boldsymbol{d} - \boldsymbol{T}\boldsymbol{a} \tag{21}$$

and the mean square error (MSE) of the residuals is

$$MSE = \frac{1}{n}\sum_{i=1}^{n} {r_i}^2 \tag{22}$$

where n is again the number of data points.

The 3-by-3 covariance matrix for the curve fit coefficients, $\boldsymbol{P}$, is

$$\boldsymbol{P} = (\boldsymbol{T}^T\boldsymbol{Q}^{-1}\boldsymbol{T})^{-1}(MSE)^2 \tag{23}$$

where $\boldsymbol{T}$ and $\boldsymbol{Q}$ retain the same values used to calculate the curve fit coefficients. The covariance matrix from Equation (23) provides a measure of accuracy for the curve fit.

The results from the curve fit were incorporated into Equations (15) and (16) to solve for the torus basis frequencies from the TLE data. The second order terms from the curve fit indicate perturbations and were not included in the basis frequency calculations. The resulting frequencies are calculated as

$$w_1 = a_{1,M} + a_{1,\omega} \pm \left(\sqrt{\boldsymbol{P}_M(2,2)} + \sqrt{\boldsymbol{P}_\omega(2,2)}\right) \tag{24}$$

$$w_2 = a_{1,\Omega} \pm \sqrt{\boldsymbol{P}_\Omega(2,2)} \tag{25}$$

where the a_1 terms are the linear coefficients from the curve fits and the $\boldsymbol{P}(2,2)$ terms are the values from the curve fit covariance matrices in the second row and second column.

This specific value from the covariance matrix provides an estimate of the accuracy of the a_1 coefficient and was incorporated into Equations (24) and (25) to provide a range of accuracy for the frequency calculation.

Generate Torus

The software package developed by Wiesel to generate torus data files accepts period, inclination, and a maximum geopotential order and degree as inputs rather than the two torus basis frequencies identified from Equations (24) and (25). The geopotential was limited to order and degree 20. The first torus frequency was converted to orbit period by

$$\tau = \frac{2\pi}{w_1} \tag{26}$$

Wiesel's torus software simultaneously solves Equation (9) and finds the Floquet solution through an iterative process, thus the inclination cannot be found directly from the basis frequencies. Instead, Equation (2) was used to acquire a suitable initial guess for the inclination. After algebraic manipulation, Equation (2) becomes

$$i = \cos^{-1}\left(\frac{2w_2a^2}{-3w_1J_2{R_\oplus}^2}\right) \tag{27}$$

where the two-body solution has been assumed for the semi-major axis and eccentricity has been assumed zero.

The inclination from Equation (27) was input into Wiesel's torus generation routine, and the output nodal regression rate was compared against the calculated second torus frequency. The input inclination was then manually adjusted and Wiesel's software rerun until the output nodal regression rate was within the range specified by Equation (25). The torus was assumed to be invalid for a test case if the inclination that resulted in the calculated nodal regression rate was more than 5 degrees outside the range of inclinations of the set of TLEs for that object. Based on this criterion, torus generation failed for the Thor 293, Delta 11, and GOES-9 test cases.

This process produced a set of data files for each successful test case that defined the surface of the torus and how motion propagates along the surface due to various perturbations. The data files include the periodic orbit, the Floquet modes, and perturbations due to the geopotential, air drag, and eccentricity. The atmospheric model used for the air drag perturbations is the model developed by Regan and Anandakrishnan (29). This atmospheric model divides the atmosphere into 20 layers such that temperature fluctuates approximately linearly within each layer. Air density is then estimated based on temperature fluctuations and molecular weight of atoms within the layers.

Create Position Vectors

Position vectors were defined in the ECI reference frame. Four sets of vectors were generated for each test case: the first TLE propagated forward for the full year, each TLE propagated forward to the epoch time of the next TLE, the first state vector of action-angle variables propagated forward for the full year, and each updated state vector of action-angle variables propagated forward to the epoch time of the next update. The time stamps for the position vectors in each set are identical, thus a total of four position vectors were acquired to define the position of the test object at any given time. The epoch times of the TLE were used to set the time steps for the position vectors. A total of 100 position vectors were generated between each TLE epoch time with the first and hundredth vector corresponding to the TLE epoch times. This resulted in a variable time step across the total data set but maintained the identical time stamps for the four sets of vectors.

TLE Position Vectors.

Vallado (32) provides software routines to implement SGP4 based on the work of Vallado, Crawford, Hujsak, and Kelso (33). The MATLAB version of this software package was utilized to produce SGP4 position vectors from TLEs. The software accepts as input a single TLE and a time in minutes from the epoch of that TLE. The software then implements SGP4 to propagate the TLE to the desired time and outputs a position and velocity vector. A custom MATLAB script was written that iteratively called Vallado's SGP4 program 100 times for each TLE and stored the resulting position and velocity vectors into arrays. The first TLE was called an additional 100 times for each subsequent TLE. The script to call SGP4 is available in Appendix B.

Torus Position Vectors.

The position vectors from SGP4 were fitted to the surface of the torus and converted to action-angle variables. Each set of 100 position vectors between TLE epoch times was fitted via Wiesel's least squares orbit fitting software, and a single set of 6 action-angle variables was produced for each set of 100 position vectors. The residuals of the least squares fit provided an indication of whether or not the TLE vectors could be fit to the surface of the torus. Any fit with residuals in tens of kilometers or more was considered as an invalid torus result. Based on this criterion, torus generation failed for the Delta 114 and Iridium 33 debris test cases.

The initial guess for Wiesel's least squares orbit fitting software consists of three action perturbations, three angle variables, and an associated epoch time. Values from the first TLE were used to create the initial guess for the actions and angles:

$$J_1 = J_2 = J_3 = Q_3 = 0 \tag{28}$$

$$Q_1 = \omega + M \tag{29}$$

$$Q_2 = \Omega - \theta_s \tag{30}$$

where here $J = 0$ indicates zero perturbation to the torus action variables and θ_s is the angle representation of Greenwich mean sidereal time (GMST). The subtraction of θ_s provides the ascending node with reference to Greenwich, which allows the software to perform calculations with respect to an Earth-centered rotating frame where the geopotential and atmospheric model do not rotate. GMST is calculated as

$$\begin{aligned} GMST = {} & -6.2 \cdot 10^{-6} \cdot T^3 + 0.093104 \cdot T^2 \\ & +(8.766 \cdot 10^5 \cdot 3600 + 8640184.812866) \cdot T + 67310.54841 \end{aligned} \tag{31}$$

where T is Julian centuries since 1 January 2000 12:00:00 Universal Time. Equation (31) gives the GMST in seconds. Recognizing that Earth rotates 2π radians in 1 Julian day and there are 86,400 seconds in 1 Julian day, GMST can be converted to an angle via

$$\theta_s = \frac{GMST \cdot 2\pi}{86400} \tag{32}$$

The result from Equation (32) was then reduced to a commensurate value between 0 and 2π radians.

The output from the least squares fitting routine was a state vector of six action-angle variables, a ballistic coefficient, and the epoch time of the angle variables that provided the best fit for the 100 position vectors used to perform the fit. The action perturbations were generally on the order of centimeters or less. The ballistic coefficient for the torus model shares the same definition as the SGP4 B* value in Equation (8) except that the reference atmospheric density, ρ_0, is the atmospheric density at perigee of the orbit.

Rather than repeating the calculations of Equations (28)-(32) for each fit, the action-angle values from one fit were used as the initial guess for the subsequent least squares fitting attempt. This process produced a number of torus state vectors equal to the number of TLEs. The epoch times of each torus state vector matched the epoch times of the TLEs.

The action variables are constant and the angle variables fluctuate linearly at a rate defined by the torus basis frequencies. Therefore, the angle variables can be propagated forward or backward to determine the state that defines the position on the surface of the torus at any time. The angle variables were propagated via

$$Q_i = Q_{i,0} + w_i t \tag{33}$$

where Q is the value of the angle variable at some time t before or after the epoch time of the known value Q_0 from the least squares fit. The subscript i indicates which angle variable is being updated.

Recall that the torus basis frequencies only account for first-order changes to mean anomaly, right ascension of the ascending node, and argument of perigee, yet the least squares fit identified these as quadratic functions of time. The second order effects were accounted for when the action-angle variables were converted to position vectors using the process outlined by Wiesel (41:635). Wiesel's process produces torus position vectors that account for three key elements: the period orbit, the Floquet modes, and the perturbations.

Compare Vectors

A root-mean-square error (RMSE) calculation was performed to quantify the differences between sets of vectors. Three comparisons were made: first, the vectors produced by propagating each TLE to the epoch of the next TLE with SGP4 were compared to the set of vectors produced by propagating the first TLE through the full data set; second, the torus vectors produced from the updated action-angle variables were compared to the vectors produced by the first state vector of action-angle variables; and third, the torus vectors produced from the updated state vectors of action-angle variables were compared to the vectors produced by propagating each TLE forward to the next TLE epoch time with SGP4. The RMSE was calculated for each set of 100 vectors, resulting in one RMSE calculation for each TLE or each state vector of action-angle variable used in the full data set. This provides a new RMSE corresponding to each time the orbit model was updated, either by the issuance of a new TLE or the update of the action-angle variables.

The RMSE was calculated for each Cartesian coordinate in the vector as

$$RMSE_i = \sqrt{\frac{\sum_1^{100} \Delta {x_i}^2}{100}} \tag{34}$$

where Δx_i indicates the difference between the two position vectors for one of the three Cartesian coordinates. The magnitude of the RMSE was then calculated as

$$RMSE = \sqrt{{RMSE_X}^2 + {RMSE_Y}^2 + {RMSE_Z}^2} \tag{35}$$

Note that Equations (34) and (35) also apply for the UVW coordinate system. The result from Equation (35) was then plotted against time to view how quickly the first position predictions diverged from subsequent updates and to view how quickly the torus model diverged from the SGP4 model.

Methodology Summary

The following process concisely summarizes the methodology implemented for this work:

1. A quadratic curve fit was performed to calculate the time rate of change of mean anomaly, right ascension of the ascending node, and argument of perigee from 1 year of TLE data. These rates identified the basis frequencies for a KAM torus.
2. Torus data files were generated with Wiesel's torus software. The files identified and included the periodic orbit, the Floquet modes, and perturbations due to the geopotential, air drag, and eccentricity.
3. Each TLE was propagated to the epoch time of the subsequent TLE to produce 100 position vectors. The first TLE was repeatedly propagated forward to produce an additional 100 position vectors between the epoch times of all subsequent TLEs.
4. The 100 position vectors from each TLE were fitted to the surface of the torus with a least squares analysis. This resulted in a set of action-angle variables that defined a location on the surface of the torus at a specific epoch time.
5. Each set of action-angle variables was propagated forward to the epoch time of the next set to produce 100 position vectors. The first set of action-angle variables was repeatedly propagated forward to produce an additional 100

position vectors between the epoch times of all subsequent sets of action-angle variables.

6. A RMSE calculation was performed and the magnitude of the RMSE was plotted against time to quantify and view the differences between the four sets of position vectors.

IV. Analysis and Results

This chapter provides a description of the results and relevant figures for one of the eight test cases. The results of the other seven test cases are included in Appendix C. Not all test cases were successful based on the criteria outlined in Chapter III, i.e., the inability to generate a valid torus for the orbit or residuals from Wiesel's least squares periodic orbit software in excess of tens of kilometers. The unsuccessful test cases are summarized in this chapter, and the data acquired up to the point of failure is included in Appendix C. A brief summary of the overall result of this research is provided at the end of this chapter.

Many plots contained in this chapter and Appendix C display only a portion of the data, not the full year. The first 2 weeks of data is the most critical to show the length of validity for a KAM torus. The error growth of SGP4 invalidates TLEs after at most a few days, thus a KAM torus model that remains accurate for a week or two would be a significant improvement over SGP4. Additionally, propagation of the action-angle variables reaches the limits of double precision accuracy as the propagation time increases beyond several months.

Unsuccessful Test Cases

Torus construction failed for three of the eight test cases. Wiesel's torus generation software required an inclination outside the range of inclinations from the TLEs for Thor 293, Delta 11, and GOES-9. The GOES-9 torus, for example, required an inclination of 31 degrees to get the desired nodal regression rate, yet the GOES-9 orbit remained inclined to 9.2 ± 1 degrees throughout the year. A possible reason that a torus could not be generated for these test cases is that the orbit was too eccentric or the inclination too near zero or the critical inclination.

An additional two test cases failed when the SGP4 position vectors could not be fit to the surface of the torus with acceptable residuals. When the position vectors were fitted to the surface of the torus, the piece of debris from Iridium 33 had residuals in excess of 300 kilometers and the Delta 114 rocket body had residuals above 20 kilometers. These large residuals demonstrate a poor fit of the SGP4 position vectors to the surface of the torus and appear to indicate that position vectors from SGP4 may not be a reliable source of pseudo observation data for the KAM torus model.

Hubble Space Telescope Results

The non-linear least squares curve fit results for right ascension of the ascending node, argument of perigee, and mean anomaly are presented in Table 3.

Table 3. Hubble Space Telescope TLE Curve Fit Results

Angle	a_0 (rad)	a_1 (rad/TU)	a_2 (rad/TU^2)
Ω	3.873573429531065e-02	-1.063801687612538e-03	-1.101680865868937e-09
ω	4.008390963534933e-02	1.733194011491032e-03	-4.002018700173017e-09
M	1.844358107584371e-02	8.806081679341767e-01	3.851875195433959e-07

Note. Curve fit of the form $X = a_0 + a_1 t + a_2 t^2$

Figures 5-7 plot the curve fit and associated residuals based on the results listed in Table 3. The days along the horizontal axis correspond to the number of days since the first TLE. These figures also provide some representation of the frequency of TLE updates, which can be discerned from the gaps between data points.

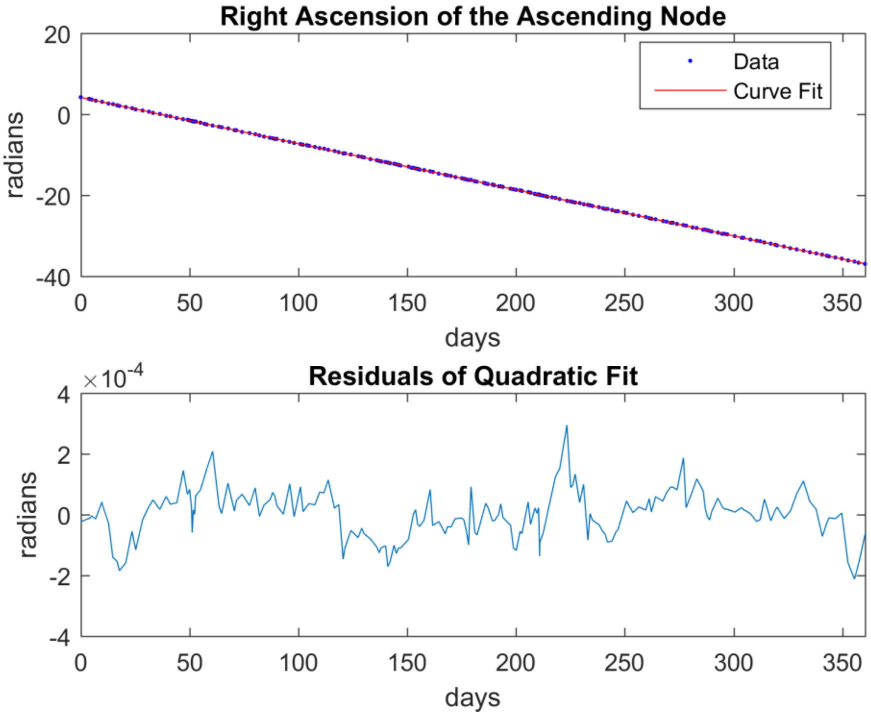

Figure 5. HST Right Ascension of the Ascending Node Curve Fit and Residuals

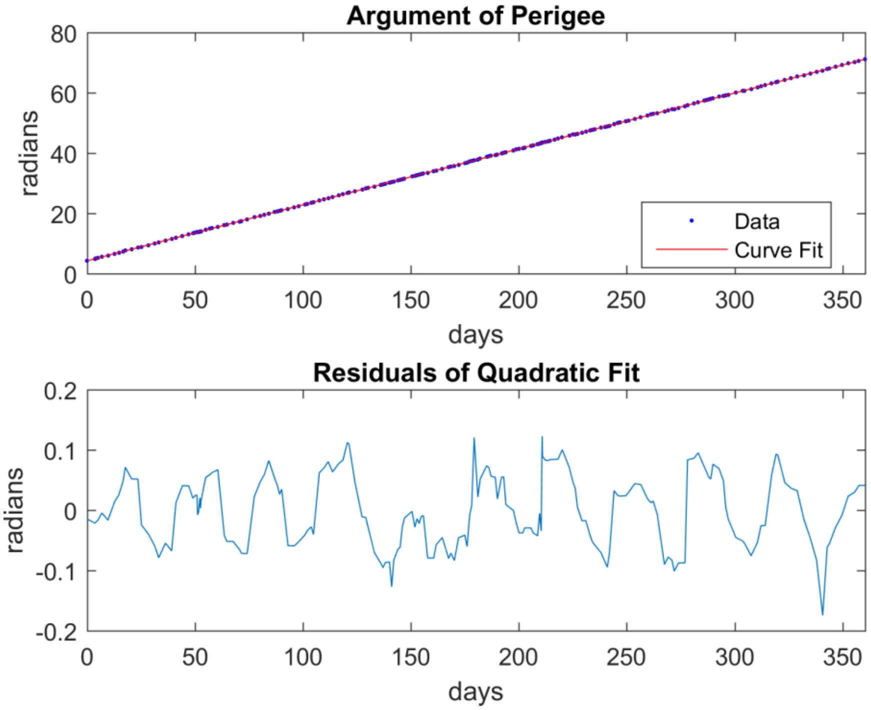

Figure 6. HST Argument of Perigee Curve Fit and Residuals

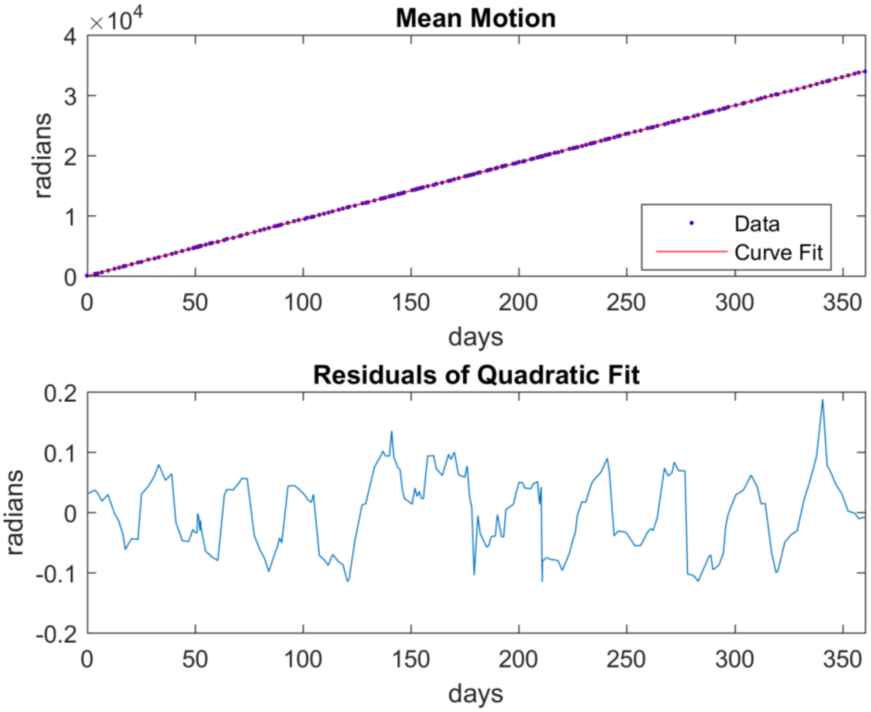

Figure 7. HST Mean Motion Curve Fit and Residuals

The linear terms from the curve fits resulted in the torus basis frequencies listed in Table 4. The nodal regression rate output by Wiesel's torus generation software for the second torus frequency was -1.06380222604781e-03 rad/TU, which is within the margin of error of the calculated frequency.

Table 4. Hubble Space Telescope Torus Basis Frequencies and Error

	Frequency (rad/TU)	± Error (rad/TU)
w_1	8.823413619456678e-01	3.057719441995443e-06
w_2	-1.063801687612538e-03	1.978932194728906e-09

The SGP4 position vectors fit to the surface of the torus with residuals under 2 kilometers for the full year, as shown in Figure 8. The error in the fit occurred primarily in the radial and in-track directions.

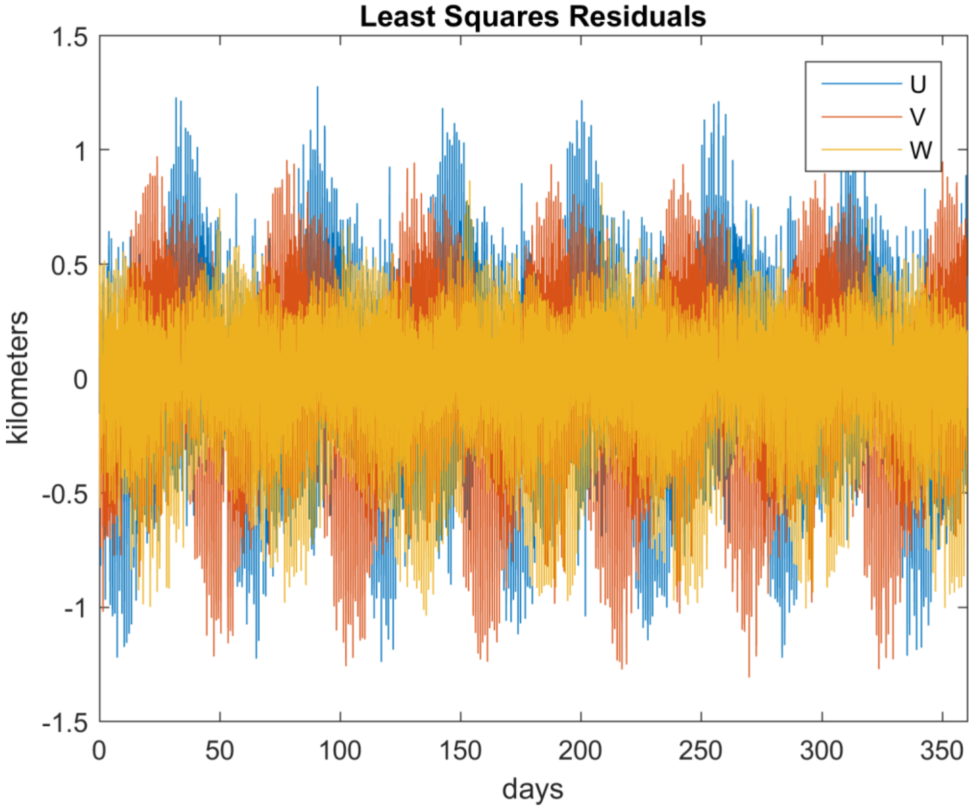

Figure 8. HST Vectors to Torus Action-Angle Least Squares Residuals

Figures 9-11 show the comparison between vector sets. Figure 9 shows the error growth between position vectors produced by SGP4 from the first TLE compared to position vectors from all subsequent TLEs. Figure 10 shows the error growth between position vectors produced from the first set of action-angle variables compared to all subsequent sets. Figures 9 and 10 (a) show the initial error growth after a few days. Figures 9 and 10 (b) show the same error growth curve but over a longer period of time. Figure 11 shows the error between position vectors produced by SGP4 from the full set of TLEs compared to position vectors produced by the torus model from the full set of updated action-angle variables.

Each figure show the magnitude of the RMSE as well as the components of the error in the radial, in-track, and orbit normal direction. Days on the horizontal axis indicate the number of days since the first TLE. Note that the straight lines connecting data points are included solely for ease of reading the plots; the lines connecting data points do not represent actual data.

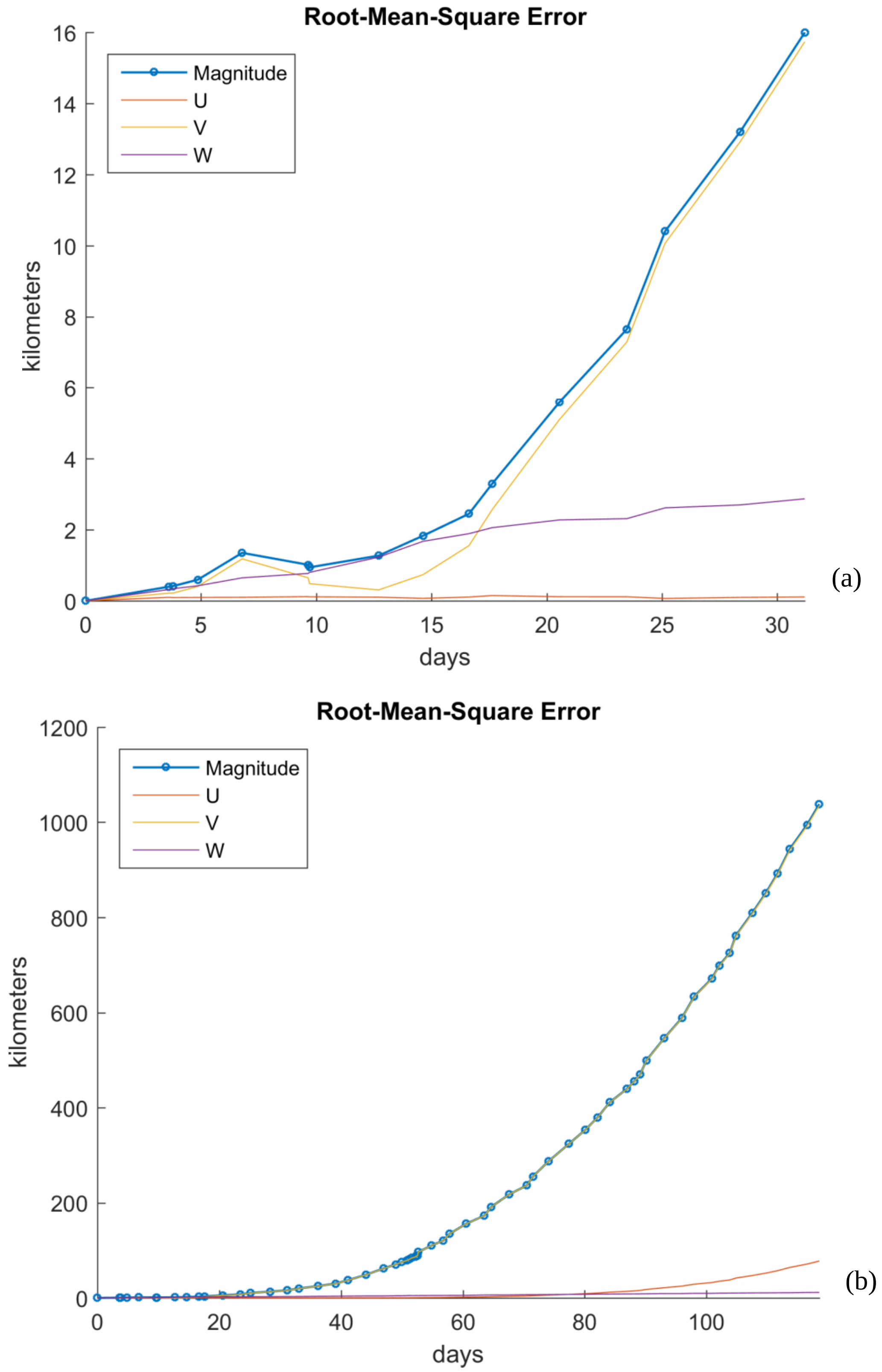

Figure 9. HST RMSE: All TLEs Compared to First TLE

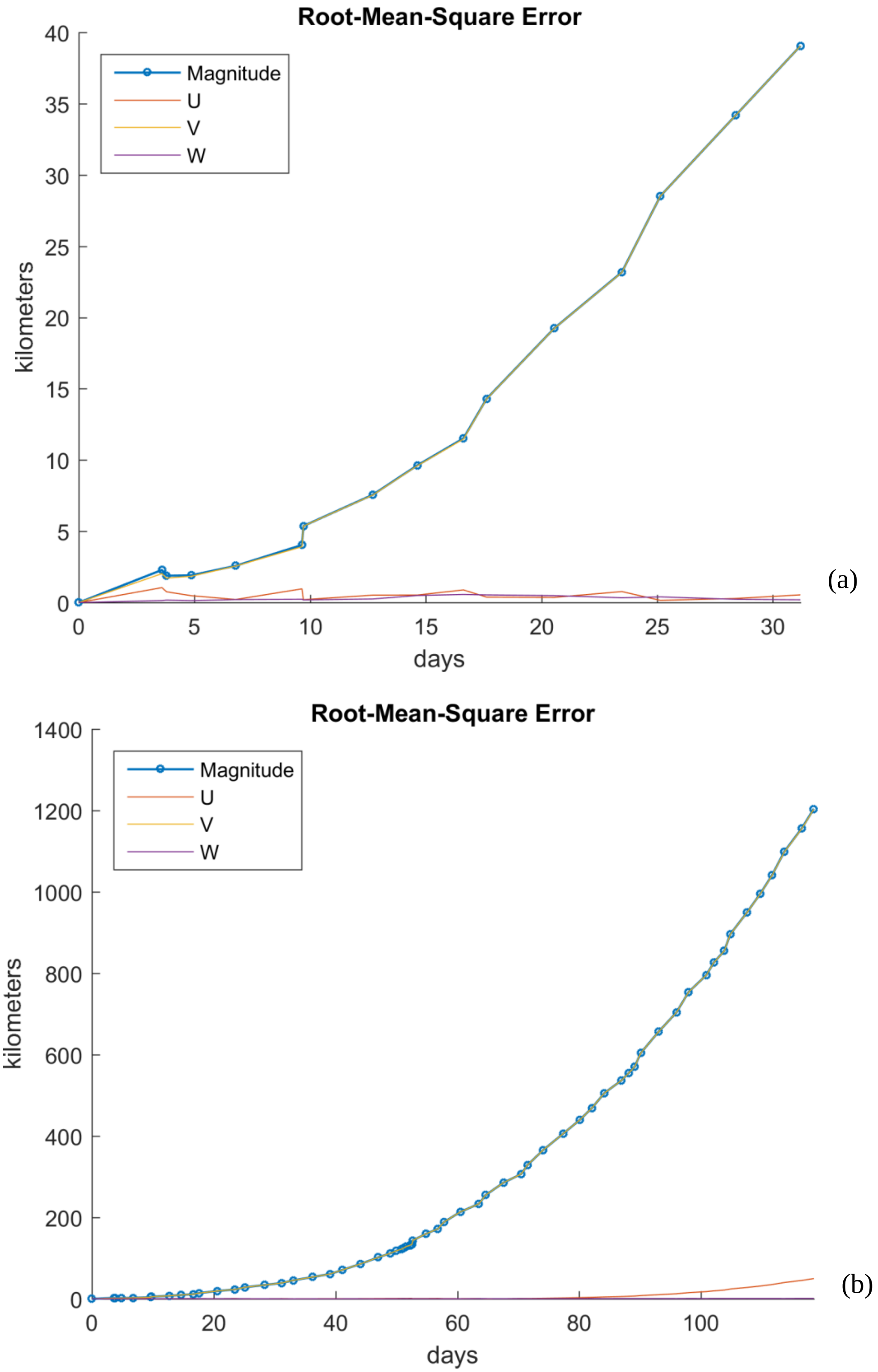

Figure 10. HST RMSE: Updated Action-Angle Sets Compared to First Set

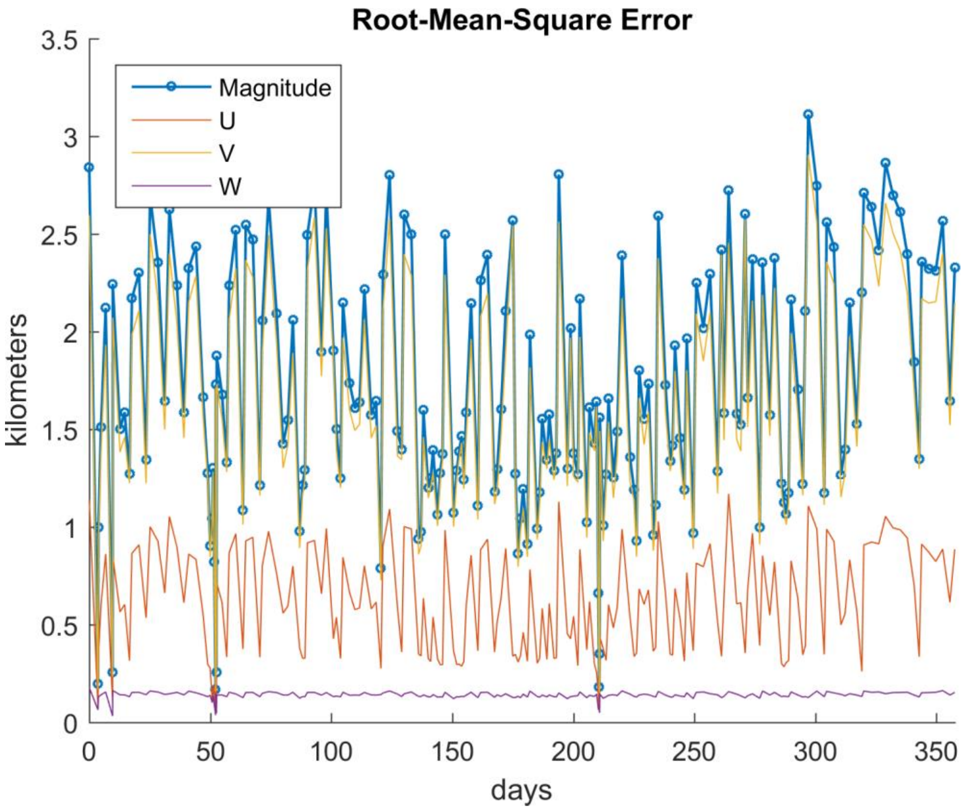

Figure 11. HST RMSE: Updated Action-Angle Sets Compared to All TLEs

As shown in Figure 9 (a), the position predictions from the TLEs exceed a RMSE of 1 kilometer after 5.9 days, which occurred between the fourth and fifth TLEs in the set. The RMSE exceeds 5 kilometers after 19.8 days, which was between the eleventh and twelfth TLEs in the set. The error continues to grow at a quadratic growth rate, as shown in Figure 9 (b), until the error reaches a maximum value approximately equal to double the orbit radius, at which point the error begins to cycle up and down. The maximum error corresponds to two orbit predictions that are on opposite sides of Earth.

The RMSE for the torus position predictions grow at a faster rate than the TLE predictions. Figure 10 (a) shows the RMSE exceeds 1 kilometer after 1.6 days, which occurred with the second action-angle set. The RMSE exceeds 5 kilometers after 9.7 days with the seventh action-angle set. As with the SGP4 model, Figure 10 (b) shows that the torus RMSE continues to grow at a quadratic growth rate.

Figure 11 shows the RMSE between the torus and SGP4 models for each set of 100 vectors over the full year. The torus and SGP4 position vectors differ primarily in the in-track direction for all predictions with a mean in-track difference of 1.59 kilometers. The vectors also differ by an average of 586 meters in the radial direction and have a nearly constant difference of 138 meters in the orbit-normal direction.

Although the torus action-angle variables were updated each time a new TLE was issued, the SGP4 vectors never fit well to the surface of the torus. Figure 12 presents the same data as Figure 11, but now the magnitude of the RMSE is plotted against the elapsed time before the next TLE was issued.

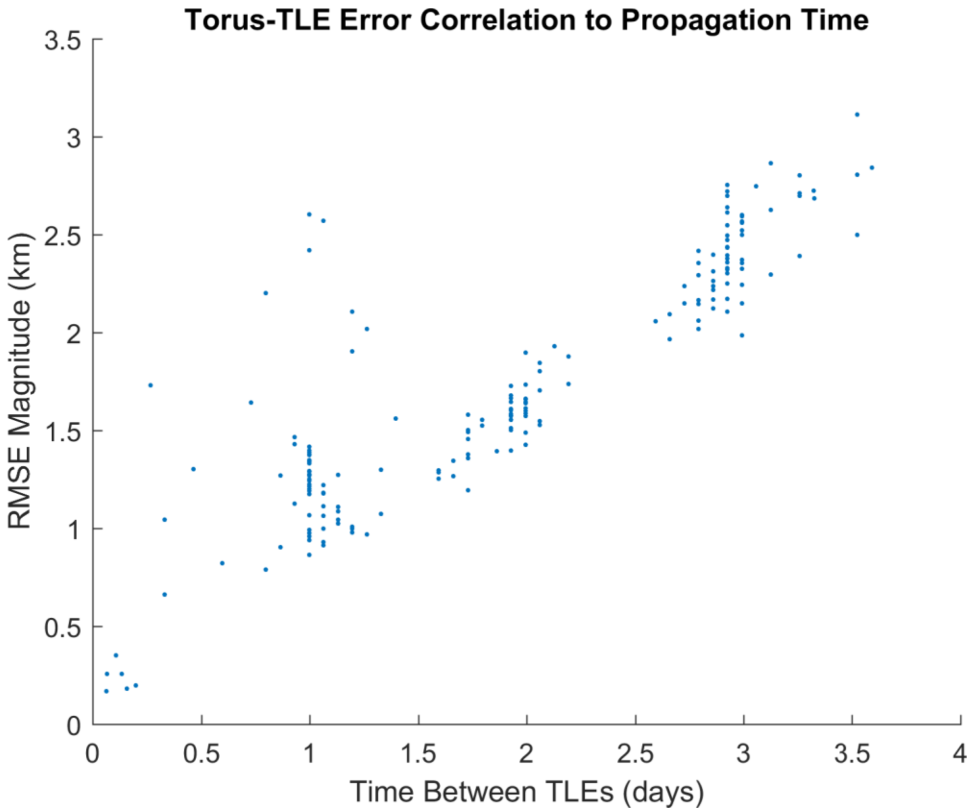

Figure 12. HST Torus-to-TLE RMSE Correlation to Elapsed Time

With the exception of a few outliers, the RMSE visually shows a strong correlation to the time between TLEs. The R^2 coefficient of a linear fit through the data is 0.711. Figure 12 shows that the position vectors from the torus model continuously diverged from the SGP4 model as each model propagated for longer periods of time, resulting in larger error as the propagation time was increased. This indicates that the two dynamics models propagate the orbit differently. The position predictions of the two models separate as the time of propagation increases. Previous research has shown the KAM torus to be far more accurate than SGP4, thus this divergence between the models is expected.

In both the SGP4 and torus prediction models, the majority of the RMSE is in the in-track direction, though the SGP4 model does show more error growth along the orbit normal than the torus model. This indicates that each new TLE updates the SGP4 model primarily to correct position predictions in the in-track direction of the orbit.

The action-angle variable updates generated from position vectors produced by SGP4 for each new TLE appear to follow the same pattern as the TLE updates, which makes sense considering the action-angle variables are produced by fitting SGP4 position vectors to the surface of the torus. As each new TLE causes an additional in-track error compared to the first TLE, each new action-angle variable set also causes an in-track error compared to the original set of action-angle variables.

Effects of Atmospheric Drag

There are three primary sources for in-track error. An incorrect mean anomaly at epoch offsets the orbit with a constant in-track error. An incorrect semi-major axis results in an error in the orbit period, causing linear in-track error growth. Lastly, an incorrect ballistic coefficient produces an unmodeled force on the object that results in quadratic in-track error growth over time (39:99).

Although not the sole source of error, atmospheric drag is the primary source of the quadratic in-track error growth shown in Figures 9-10, 32-33, and 40-41. The SL-14 rocket body, which resides at the lowest altitude out of the three successful test cases, showed the fastest error growth, while Hubble, which orbits much higher above Earth, showed the slowest error growth. For each day of propagation time, the RMSE between the SGP4 model and the torus model of the SL-14 rocket body orbit reached as much as 20 kilometers whereas the RMSE between the models of the Hubble orbit grew at most 2.6 kilometers.

Figure 13 shows a histogram of the B* values SGP4 used for each successful test case throughout the 1 year of TLE data. The histograms are superimposed to allow comparison between the different test cases.

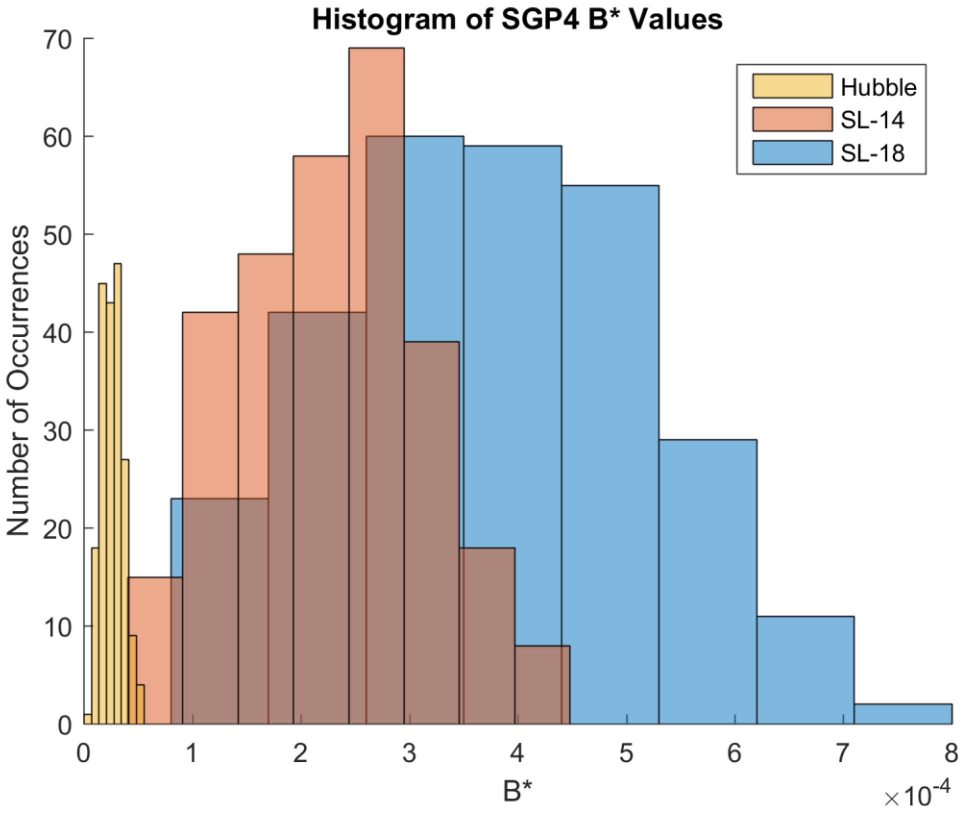

Figure 13. Histogram of Ballistic Coefficients

Each histogram in Figure 13 shows a nearly Gaussian distribution of B* values. The Gaussian distribution appears to indicates that the simplified analytical atmosphere model SGP4 uses to approximate drag follows a nearly random distribution about some average value. The true value of the ballistic coefficient fluctuates continuously as the object rotates and as the atmosphere expands or contracts, so a random distribution for B* is expected. However, the in-track error shown in Figures 9-10, 32-33, and 40-41 for the orbit propagations—which are worse for objects in lower orbit—and the Gaussian distributions of the B* values shown in Figure 13 indicate that atmospheric drag may not be appropriately modeled by the deterministic assumptions of SGP4 that B* is constant over a period of hours or days.

Results Summary

The increased rate of error growth for the torus model compared to the SGP4 error growth does not indicate that the torus is the inferior model. These results do not indicate which model provides a more accurate representation of the true orbit because the true orbit is unknown. Rather, the increased error between subsequent action-angle sets indicates that the torus model propagates along a different orbit trajectory or at a different rate around the orbit than the orbit propagated by SGP4. This difference in predicted orbit path results in a more drastic change for the torus model with each update to the action-angle set as the torus must adjust to account for the new TLE and reconverge to the SGP4 orbit. This result appears to indicate that, while the TLEs can be used to extract torus basis frequencies, the SGP4 position vectors produced from TLEs may not be a viable source of data for the KAM torus orbit propagator.

V. Conclusions and Recommendations

This research aimed to examine whether or not the KAM torus model was a viable alternative to SGP4 and could use TLEs as pseudo observation data by examining the rate at which orbit predictions diverge from an initial prediction. Other research efforts—outlined in Chapter II—have shown that the KAM torus diverges from a numerically integrated reference orbit by a few meters over a period of several months. This research successfully identified torus basis frequencies from TLEs and, for some test cases, generated a torus model to represent the position vectors corresponding to the TLE epoch times. However, the tori generated from SGP4 position vectors were poor predictors of the TLE data with errors averaging 1.7 kilometers for the best case and exceeding 50 kilometers for the worst case. Additionally, when using TLEs as pseudo observational data for the torus model, the KAM torus appears to require more updates to the action-angle variables than the number of updates SGP4 provides for TLEs.

Significance of Research

This research has identified three noteworthy contributions to research into KAM theorem. First, a new method was developed to successfully remove absolute jumps exceeding 2π radians in the mean anomaly angular data of TLEs. This new method enables researchers to examine the time history of mean anomaly as reported by SGP4 and perform accurate analysis on changes to an orbit. Second, this research confirmed that torus basis frequencies can be extracted from the mean orbital elements contained within TLEs. Although the accuracy of the extracted frequencies was not determined as the true orbit was unknown, the extracted frequencies were successfully utilized to generate tori for five of the eight test case. Finally, this research has identified that position vectors from SGP4 may not be suitable for use as pseudo observation data for the KAM torus model.

The concept of applying KAM theorem to Earth orbit determination is still in its infancy. As shown by this research, the current implementation of KAM theorem still needs additional work before it can apply to all orbit regimes. This research did not examine any orbiting objects with impulsive maneuver capabilities, yet a torus could not be generated using the basis frequencies extracted from the TLEs for three of the eight test cases. There clearly exists some subset of orbit regimes for which the torus model remains unusable, though further examination is required to identify specifically which orbit regimes are viable candidates to be modeled with the KAM torus.

The results of this research pose an interesting question for examination: what is the limiting factor of predictability? For the KAM torus model as it was generated in this research, the limiting factor was the way in which SGP4 produces position vectors. The KAM torus action-angles propagate along a different orbit path than the SGP4 TLEs despite using data from SGP4 to produce the action-angle variables. For SGP4, the limiting factor of predictability appears to be dominated by air drag. The simplified analytical model SGP4 implements for atmospheric drag fails to account for non-deterministic effects of the atmosphere. SGP4 is known to have at best an average error of 1 kilometer at the TLE epoch time. The lack of consistency with the position vectors produced by TLEs from the SGP4 model contributed to the significant divergence of the torus models produced in this research.

Recommendations for Future Research

The next step in this research process is to compare the orbit data produced in this research to actual observation data or, if available, GPS ephemeris data. TLEs provide an approximate position of a satellite as a best fit of available observation data to the SGP4 dynamic model. If the torus model was generated using raw observation data as reference vectors instead of vectors produced by SGP4, the model may show less divergence with each update to the action-angle variables, though the initial fit to the surface of the torus would likely have higher residuals to account for various sensor inaccuracies. This is an area of research that should be explored. If precise ephemeris data derived from GPS position data for the orbiting object is also available, then a comparison should be made to see how closely the KAM torus model resembles the true orbit of the object and determine for how long the KAM torus model can be used before the action-angle variables need to be updated. If further research can show that the KAM torus model resembles the true orbit to within a few kilometers or less after several days of propagation, then one could definitively conclude that the KAM torus is more accurate than SGP4.

If true observation data is not available, then observations could be simulated from a numerically integrated orbit. The position vectors from the numerically produced orbit can be converted into measures of azimuth, elevation, range, and range-rate to simulate radar tracking, or the vectors can be converted to azimuth and elevation or right ascension and declination to simulate optical tracking. Sensor error can be simulated by corrupting the numerically true measurement data with Gaussian noise.

Another area for examination is the possibility of modeling an orbit with B* as a random variable. Propagation models that maintain a constant B* for hours or more ignore the constant fluctuations of the atmosphere and any rotations of the orbiting object. A stochastic model of B* may reveal additional information about changes to an orbit between observation updates.

Further research in this field should also examine a potential change to the methodology implemented by this research. The SGP4 vectors showed large residuals when fit to the surface of the torus. Although the residuals provide a strong indication that the SGP4 vectors do not fit well to the surface of the torus, these residuals may also have been slightly influenced by the reference frame used. The residuals may, in part, indicate that the TEME reference frame is not sufficiently inertial for this application. The J2000 frame, which defines the Cartesian vectors according to the mean equator mean equinox as of noon Terrestrial Time on 1 January 2000, may be more suitable than the TEME frame. A future researcher should convert the SGP4 vectors to the J2000 inertial reference frame before fitting to the torus to check if the J2000 reference frame provides smaller residuals.

Another potential change to examine is to attempt to produce a better covariance matrix for the TLE data when identifying the torus basis frequencies. If the most recent TLE is assumed to be the best estimate of the true position, then one could iteratively examine the error between state vectors produced by earlier TLEs and the current TLEs to produce a covariance matrix. Although a covariance matrix produced in this manner still will not be the true covariance matrix, it may provide a better estimate of the covariance than the identity matrix.

Conclusions of Research

This research examined the rate at which new SGP4 position predictions diverge from previous SGP4 predictions. SGP4 position vectors were also used as pseudo observational data for the KAM torus orbit model. The rate at which SGP4 diverges from itself was then compared to the rate at which the KAM torus orbit model generated from SGP4 position vectors diverges. This research found that SGP4 position predictions remained more consistent with each TLE update than the KAM torus orbit predictions produced by fitting SGP4 position vectors to the surface of the torus.

The results of this research appear to indicate that the KAM torus model in its current state is not a viable alternative to SGP4 due to the fact that several test cases failed to produce valid torus models. However, part of that failure may be attributed to the position data from SGP4 used to generate the torus state vector. Two test cases showed residuals between the SGP4 vectors and the torus surface ranging from tens to hundreds of kilometers. This is a strong indicator that the inaccuracies of the SGP4 dynamics model may be prohibitive for constructing KAM tori.

If the results had shown that the position predictions of a KAM torus diverged slower than the position predictions of SGP4, then this research would have indicated not only that the KAM torus model is potentially a better alternative, but also that TLEs can provide more information than is immediately apparent by serving as pseudo observation data for an alternative analytical model. Since the results instead show that SGP4 predictions diverge slower than KAM torus predictions, this research fails to provide an indication either way about which general perturbations propagator is a better model. Instead, the research has shown that the KAM torus propagates along a different orbital path than SGP4 and that position vectors from SGP4 appear to be an unviable substitute for true observation data for the KAM torus model with the current methodology.

Appendix A. MATLAB Script to Identify Torus Basis Frequencies from TLEs

```
% ProcessRawTLE.m
% Author: Capt Kenneth Stuart
%
% This script reads a text file containing two-line element set data and
% stores epoch, bstar, inclination, right ascension of ascending node,
% eccentricity, argument of perigee, mean anomaly, mean motion, and first
% derivative of mean motion. Duplicate TLE data points are removed.
%
% Units are (mostly) converted to radians, TU, and DU. Angles are unwrapped
% to remove 2*Pi jumps.  Conversion factors are from EGM96.
%
% Quadratic curve-fits are found for RAAN, omega, and M.  Torus frequencies
% are found to create a periodic orbit.


%% Conversion factors, constants
format longE
mu = .3986004418e15;     % gravitational constant, m^3/s^2 (from EGM96)
DU = 6378137;            % radius of Earth, m (from EGM96)
TU = (DU^3/mu)^.5;       % time unit, s
MU = 1;                  % gravitational constant, DU^3/TU^2
wEarth_s = 7292115e-11;  % rad/s (from EGM96)
wEarth = wEarth_s*TU;    % rad/TU
dg2rd = pi/180;          % degrees to radians
dy2TU = 24*3600/TU;      % 24-hour day to TU
twopi = 2*pi;            % also used for revolutions to radians


%% Read TLE Data File
% File shall have TLE data beginning on line 1 and ending on the last line
% of the TLE text file.  There shall be no empty lines in the text file.
% Several values in the TLE are ignored.

fid=fopen('Hubble_1Jan10_31Dec10.txt');
% fid=fopen('SL14_1Jan14_31Dec14.txt');
% fid=fopen('SL18_1Jan14_31Dec14.txt');
% fid=fopen('Iridium33debris_1Jan14_31Dec14.txt');
% fid=fopen('GOES9_1Jan14_31Dec14.txt');
% fid=fopen('Delta114_1Jan09_31Dec09.txt');
% fid=fopen('Delta11_1Jan09_31Dec09.txt');
% fid=fopen('Thor293_1Jan09_31Dec09.txt');

% Determine number of TLEs in file
num_TLE=0;
while ~feof(fid)
    line1 = fgetl(fid);
    line2 = fgetl(fid);
    num_TLE=num_TLE+1;
end
fseek(fid,0,-1);

% Preallocate matrices
M=cell(num_TLE,1); epoch_raw=M; ndot2=M; bstar_raw=M; incl=M; RAAN=M;
ecc_raw=M; omega=M;
n=zeros(num_TLE,1); epoch=n; bstar=n; rev=n;
```

```
% Read data
for ii=1:num_TLE
    epoch_raw(ii) = textscan(fid,'%*n %*s %*s %s',1);
    ndot2(ii) = textscan(fid,'%f',1);
    bstar_raw(ii) = textscan(fid,'%*s %s %*[^\n]',1);
    incl(ii) = textscan(fid,'%*n %*n %f',1);
    RAAN(ii) = textscan(fid,'%f',1);
    ecc_raw(ii) = textscan(fid,'%f',1);
    omega(ii) = textscan(fid,'%f',1);
    M(ii) = textscan(fid,'%f',1);
    nrev = textscan(fid,'%16c %*[^\n]',1);%,'delimiter',';');
    nrev = nrev{1};
    n(ii) = str2double(nrev(1:11));
    rev(ii) = str2double(nrev(12:16));
end; fclose(fid);


%% Process Raw Data
% Convert cell data to numbers
ndot2 = cell2mat(ndot2); incl = cell2mat(incl); RAAN = cell2mat(RAAN);
omega = cell2mat(omega); M = cell2mat(M); ecc = cell2mat(ecc_raw)*1e-7;

% Process revnum
% The rev in the TLE has 5 digits. If the revnum goes over 99999, it resets
% to 0 in the TLE. The following loop corrects for that, then sets the rev
% to start at 0 so rev counts the revolutions since the first TLE.
for ii=2:num_TLE
    if rev(ii-1)>rev(ii)
        rev(ii:end) = rev(ii:end)+1e5;
    end
end; rev = rev-rev(1);

% Process epoch
% Epoch in TLE is solar time (24-hour days)
date1 = str2double(epoch_raw{1});
year1 = floor(date1/1000); day1 = date1-year1*1000;
if year1 < 57; year1 = year1+2000;
else year1 = year1+1900; end
jdate1 = jday(year1,1,day1,0,0,0);

for ii=1:num_TLE
    date = str2double(epoch_raw{ii});
    year = floor(date/1000); day = date-year*1000;
    if year < 57; year = year+2000;
    else year = year+1900; end
    jdate = jday(year,1,day,0,0,0);
    epoch(ii) = jdate-jdate1; % 24-hr days since first TLE

% Process bstar
    b_string = char(bstar_raw{ii});
    if length(b_string) == 7
        b_string = strcat('+',b_string);
    end
    bstar(ii) = str2double(b_string(1:6))*1e-
5*10^str2double(b_string(7:8));
end
```

```
% Remove duplicate TLE entries and any TLE issued less than 1 hour before
% the next TLE (this indicates a correction to a TLE).
data = [epoch,ndot2,bstar,incl,RAAN,ecc,omega,M,n,rev]; ii=2;
num_data=num_TLE;
while ii < num_data
    if abs(data(ii,1)-data(ii-1,1)) < .041667   % 1 hour = 0.041667 days
        data(ii-1,:)=[];
        num_data=num_data-1;
    end
    ii = ii+1;
end
epoch=data(:,1); ndot2=data(:,2); bstar=data(:,3);
incl=data(:,4);RAAN=data(:,5);
ecc=data(:,6); omega=data(:,7); M=data(:,8); n=data(:,9); rev=data(:,10);

% Convert revolutions or degrees to radians
ndot2 = ndot2*twopi; n = n*twopi;
incl = incl*dg2rd; RAAN = RAAN*dg2rd; omega = omega*dg2rd; M = M*dg2rd;

% Unwrap RAAN and omega
RAAN = unwrap(RAAN); omega = unwrap(omega);

% Unwrap M
% Rev number may be inaccurate, thus can't set M=M+2*pi*rev. Instead, use
% M=M+n*dt+ndot2*dt^2, compare to M=M+2*pi*rev, and adjust M to match value
% in TLE plus the appropriate 2*pi*rev adjustment.  Corrected rev number
% is stored in rev_adj.  Explanation of steps:
%   M(:,1) = raw data
%   M(:,2) = M_raw+2*pi*rev
%   M(:,3) = M_raw+2*pi*rev +/- 2*pi corrections
%   M(:,4) = corrected previous M(:,3) + n*dt + ndot/2*dt^2
M(:,2)=M+twopi*rev; M(:,3)=M(:,2); M(1,4)=M(1,1); M(1,5)=0; rev_adj = rev;
for ii=2:num_data
    dt=epoch(ii)-epoch(ii-1);
    M(ii,4) = M(ii-1,3) + n(ii-1)*dt + ndot2(ii-1)*dt^2;
    diff = M(ii,3)-M(ii,4);
    if abs(diff) > 6
        multiplier = round(diff/2/pi);
        M(ii:end,3) = M(ii:end,3)-twopi*multiplier;
        rev_adj(ii:end)=rev_adj(ii:end)-multiplier;
    end
end
M=M(:,3);

% Recompile data matrix with processed data
data = [epoch,ndot2,bstar,incl,RAAN,ecc,omega,M,n,rev,rev_adj];


%% Perform Least Squares Fit
% Data = a0 + a1*t + .5*a2*t^2
% Assuming all data points are equally reliable and statistically
% independent, i.e., data covariance matrix Q is the identity matrix
T=ones(num_data,3); T(:,2)=epoch; T(:,3) = .5*epoch.^2;
TtranT = T'*T; TtranT_inv = inv(TtranT); TtranT_inv_Ttran = TtranT\T';
```

```
% Quadratic curve-fit coefficients, a
% Units: a(1)=rad; a(2)=rad/day; a(3)=rad/day^2 (day=24hrs)
a_RAAN = TtranT_inv_Ttran*RAAN;
a_omega = TtranT_inv_Ttran*omega;
a_M = TtranT_inv_Ttran*M;

% Residuals, res
% Units: rad
res_RAAN = RAAN-T*a_RAAN;
res_omega = omega-T*a_omega;
res_M = M-T*a_M;

% Mean square error, sig2
% Units: rad^2
sig2_RAAN = 1/num_data*(res_RAAN'*res_RAAN);
sig2_omega = 1/num_data*(res_omega'*res_omega);
sig2_M = 1/num_data*(res_M'*res_M);

% Covariance of curve-fit, P
% Covariance matrix for state vector a
P_RAAN = TtranT_inv*sig2_RAAN;
P_omega = TtranT_inv*sig2_omega;
P_M = TtranT_inv*sig2_M;


%% Calculate Torus Frequencies
% Excluding second order terms in quadratic curve-fit (these are the
% perturbation terms).  Units converted to rad/TU.
% w1 = d/dt(M) + d/dt(omega)
% w2 = -w_Earth + d/dt(RAAN)
w1 = (a_M(2)+a_omega(2))/dy2TU;
w2 = a_RAAN(2)/dy2TU; %-wEarth;  % Earth rotation rate is already included
in the TEME frame, otherwise it would need to be subtracted.
w1_err = (sqrt(P_M(2,2))+sqrt(P_omega(2,2)))/dy2TU;
w2_err = sqrt(P_RAAN(2,2))/dy2TU;


%% Clear non-needed working variables
clearvars ans b_str* date* day* dg2rd diff dt DU dy2TU fid ii jdate* line*
mu MU mult* nrev *_raw result* sig2* Ttran* TU twopi wEar* year*
```

Appendix B. MATLAB Script to Produce Position Vectors with SGP4

```
% TLEPositionCompare.m
% Author: Capt Kenneth Stuart
%
% This script reads a text file containing at least 2 two-line element sets
% and creates N position vectors for each TLE forward to the next TLE and N
% position vectors backward to the previous TLE.  The position vectors are
% then compared to see how well SGP4 agrees with itself. (The value N is
% set by the variable Npts below.)
%
% The script also propagates the first TLE forward through all time steps
% in order to see how one TLE diverges from all subsequent TLEs.
%
% When the script encounters a set of TLEs with identical epoch dates,
% only the last TLE of the set is recorded, regardless of whether or not
% other elements in the TLEs are different.
%
% If you run ProcessRawTLE.m first, you can use a FOR loop in the Read TLE
% Data File section of this code instead of the WHILE loop for increased
% speed.  Comment/Uncomment the appropriate line to adjust.
%
% note: this program is heavily dependent on directory/sub-directory layout
% and will likely need revision if adapted for future use.
%
% All SGP4 code was downloaded from Vallado's software package at
% www.MicrocosmPress.com.  This software was used without modification.

Npts = 100;
format longE


%% Select data source
% 1 = Hubble, 2010
% 2 = SL-14, 2014
% 3 = SL-18, 2014
% 4 = Iridium 33 debris, 2014
% 5 = GOES-9, 2014 (fails next step)
% 6 = Delta 114, 2009
% 7 = Delta 11, 2009 (fails next step)
% 8 = Thor 293, 2009 (fails next step)
source = 1;


%% Read TLE Data File
% File shall have TLE data beginning on line 1 and ending on the last line
% of the TLE text file.  There shall be no empty lines in the text file.
switch source
    case 1; fid=fopen('../Hubble_1Jan10_31Dec10.txt');
    case 2; fid=fopen('../SL14_1Jan14_31Dec14.txt');
    case 3; fid=fopen('../SL18_1Jan14_31Dec14.txt');
    case 4; fid=fopen('../Iridium33debris_1Jan14_31Dec14.txt');
    case 5; fid=fopen('../GOES9_1Jan14_31Dec14.txt');
    case 6; fid=fopen('../Delta114_1Jan09_31Dec09.txt');
    case 7; fid=fopen('../Delta11_1Jan09_31Dec09.txt');
    case 8; fid=fopen('../Thor293_1Jan09_31Dec09.txt');
end
```

```
% Initialize variables for SGP4
% Each TLE set is stored as a nested structure: satrecs.TLE#
% For TLEs with identical epoch dates, only the later TLE is stored.
% Use FOR loop if length of TLE file is known from ProcessRawTLE.m,
% otherwise use WHILE loop.  Comment/Uncomment appropriate line.
satrecs.TLE1=struc([]); count='TLE1'; num_data=0; epoch_date_old = 0;
line1=cell(1); line2=line1;

% while ~feof(fid)      % Use WHILE LOOP if running as standalone code
for ii=1:num_TLE      % Use FOR LOOP if running after ProcessRawTLE
(num_TLE is defined)
    line1{1}=fgetl(fid);
    line2{1}=fgetl(fid);
    [~,~,~,satrec] = twoline2rv(line1{1},line2{1},'c','','',84);
    epoch_date_new = satrec.jdsatepoch+satrec.jdsatepochf;
    if abs(epoch_date_new-epoch_date_old) < .041667 % disregard TLE if the
next TLE is issued less than 1 hour later
        satrecs.(count)=satrec;
    else
        num_data=num_data+1;
        count=strcat('TLE',num2str(num_data)); satrecs.(count)=satrec;
        line1{num_data+1,1}=line1{1}; line2{num_data+1,1}=line2{1}; % store
TLEs that were not discarded
    end
    epoch_date_old = epoch_date_new;
end
fclose(fid); num_vec=(num_data-1)*Npts; line1(1,:)=[]; line2(1,:)=[];


%% Run SGP4
% Initialize loop variables
bwd='TLE1';
epoch_date=[0;satrecs.TLE1.jdsatepoch+satrecs.TLE1.jdsatepochf];
times_TLE=zeros(num_vec,1); ctr=1; t_1=0; r_TLE=zeros(num_vec,3);
r_TLE_bwd=r_TLE; r_TLE_1=r_TLE; v_TLE=r_TLE; v_TLE_1=r_TLE;
r_TLE_J2000=r_TLE; v_TLE_J2000=r_TLE; r_TLE_1_J2000=r_TLE;
v_TLE_1_J2000=r_TLE;

% Create position vectors
for ii=2:num_data
    % Load 2 TLEs, determine time between them
    fwd = bwd;
    bwd = strcat('TLE',num2str(ii));
    epoch_date(1) = epoch_date(2);
    epoch_date(2) = satrecs.(bwd).jdsatepoch+satrecs.(bwd).jdsatepochf;
    epoch_diff = epoch_date(2)-epoch_date(1);    % difference, days
    epoch_diff_min = epoch_diff*1440;            % difference, minutes

    % Create timestep parameters
    times_TLE(ctr) = epoch_date(1);          % time of data point, days
    tstep = epoch_diff/(Npts-1);             % time step, days
    tstep_min = epoch_diff_min/(Npts-1);     % time step, minutes
    t_fwd = 0:tstep_min:epoch_diff_min;      % times for SGP4, minutes
    t_bwd = t_fwd-epoch_diff_min;
    t_1 = t_1(end)+t_fwd;
```

```
    % Run SGP4
    for jj=1:Npts
        [~,r_TLE(ctr,:),v_TLE(ctr,:)] = sgp4(satrecs.(fwd),t_fwd(jj));
        [~,r_TLE_bwd(ctr,:),~] = sgp4(satrecs.(bwd),t_bwd(jj));
        % propagate first TLE through entire series
        [~,r_TLE_1(ctr,:),v_TLE_1(ctr,:)] = sgp4(satrecs.TLE1,t_1(jj));

    % Convert to J2000 reference frame
        ttt=epoch_date(1)/36525;

[r_TLE_J2000(ctr,:),v_TLE_J2000(ctr,:),~]=teme2eci(r_TLE(ctr,:)',v_TLE(ctr,
:)',[0 0 0]',ttt,50,2,'a');

[r_TLE_1_J2000(ctr,:),v_TLE_1_J2000(ctr,:),~]=teme2eci(r_TLE_1(ctr,:)',v_TL
E_1(ctr,:)',[0 0 0]',ttt,50,2,'a');

        ctr=ctr+1; times_TLE(ctr)=times_TLE(ctr-1)+tstep; % time of data
point, days
    end
end
times_TLE = times_TLE(1:end-1);   % remove extra data point created by loop
above

times_TLE_mod = times_TLE-2440000;          % Time, modified Julian date
times_TLE_zero = times_TLE-times_TLE(1);    % Time, counting up from zero


%% Clear non-needed working variables
clearvars ans bwd count ctr epoch_d* fid fwd ii jj satrec t_* ttt tstep*
```

Appendix C. Results for Additional Test Cases

Results for all test cases except Hubble are presented here without preamble. Note that for unsuccessful test cases, results are presented up to the point of failure. These results are presented here in the same order as the Hubble results are presented in Chapter IV. Refer to Chapter IV for an explanation of the data presented.

Delta 11 Rocket Body Results

Table 5. Delta 11 Rocket Body TLE Curve Fit Results

Angle	a_0 (rad)	a_1 (rad/TU)	a_2 (rad/TU^2)
Ω	3.752839679281807e-02	-3.039516009881237e-04	3.112042550028040e-11
ω	2.445364852700072e-02	3.248952437491975e-04	-4.240662362985422e-10
M	3.663427918133740e-02	5.363758166513375e-01	-3.841781684896315e-08

Note. Curve fit of the form $X = a_0 + a_1 t + a_2 t^2$

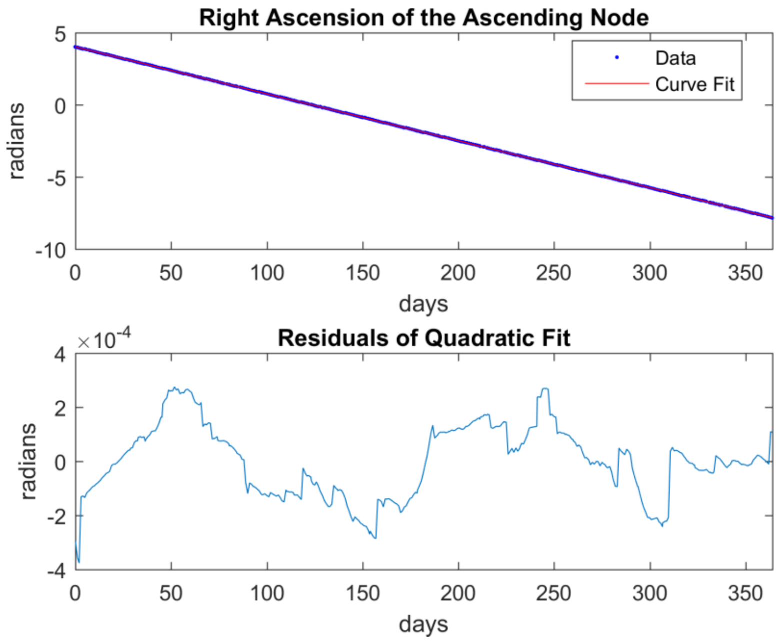

Figure 14. Delta 11 Right Ascension of the Ascending Node Curve Fit and Residuals

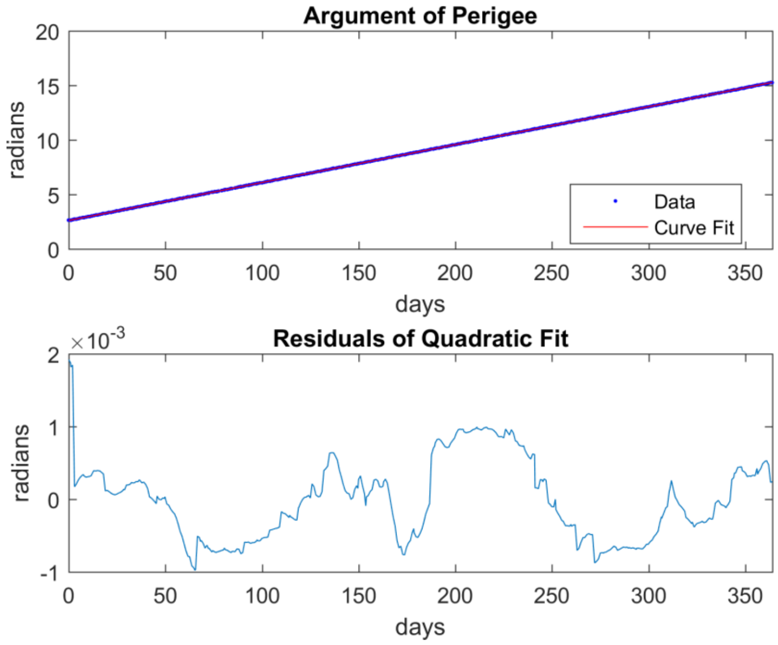

Figure 15. Delta 11 Argument of Perigee Curve Fit and Residuals

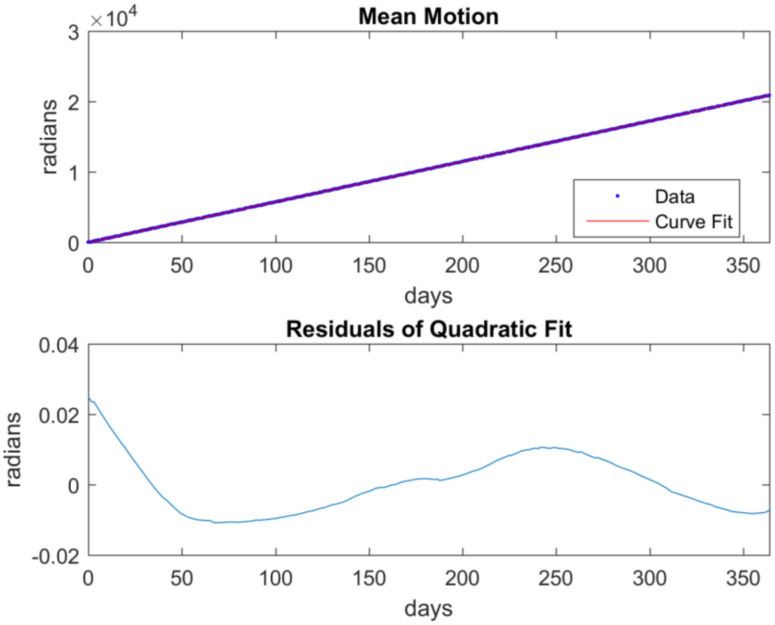

Figure 16. Delta 11 Mean Motion Curve Fit and Residuals

Table 6. Delta 11 Rocket Body Torus Basis Frequencies and Error

	Frequency (rad/TU)	± Error (rad/TU)
w_1	5367007118950867e-01	1.483034581406186e-07
w_2	-3.039516009881237e-04	2.254144125515855e-09

Torus construction failed for the Delta 11 test case. No further data was collected for this test case.

Delta 114 Rocket Body Results

Table 7. Delta 114 Rocket Body TLE Curve Fit Results

Angle	a_0 (rad)	a_1 (rad/TU)	a_2 (rad/TU^2)
Ω	3.441424379393487e-02	-1.103525303929862e-03	-1.055192694781698e-08
ω	1.608265718821470e-03	1.882824479292471e-03	1.823592831389637e-08
M	5.617886088083420e-02	8.831055129890579e-01	3.690266877701797e-06

Note. Curve fit of the form $X = a_0 + a_1 t + a_2 t^2$

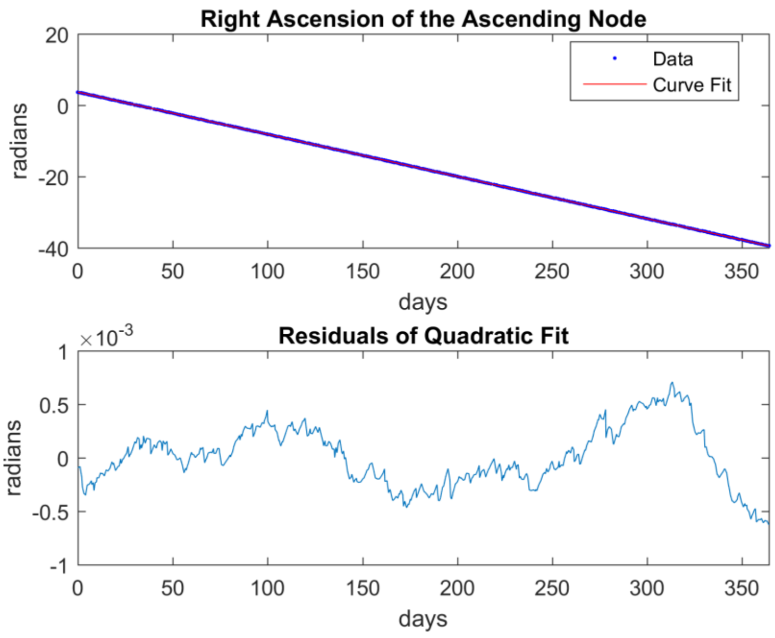

Figure 17. Delta 114 Right Ascension of the Ascending Node Curve Fit and Residuals

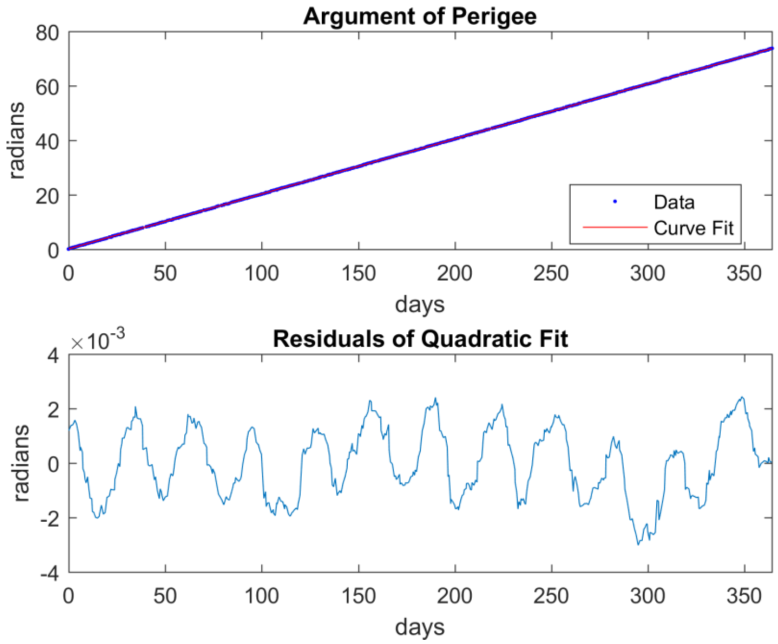

Figure 18. Delta 114 Argument of Perigee Curve Fit and Residuals

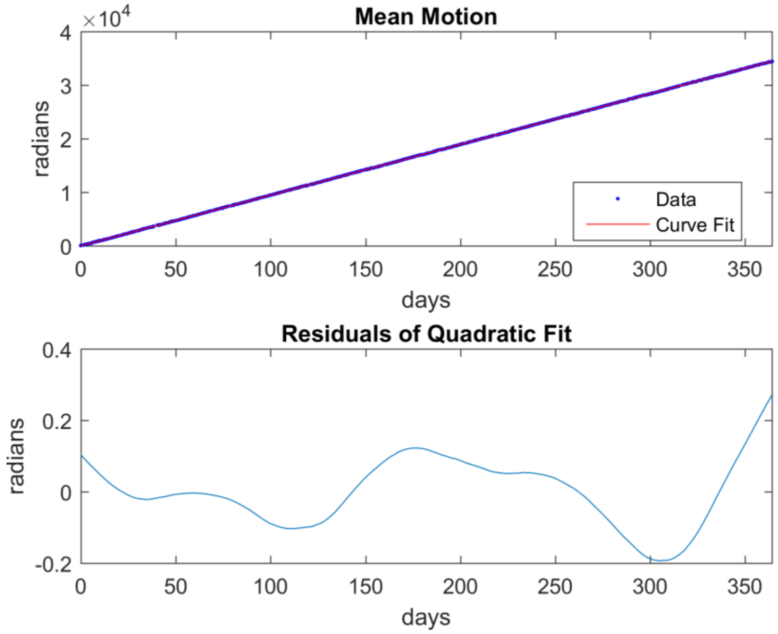

Figure 19. Delta 114 Mean Motion Curve Fit and Residuals

Table 8. Delta 114 Rocket Body Torus Basis Frequencies and Error

	Frequency (rad/TU)	± Error (rad/TU)
w_1	8.849883374683504e-01	1.446924275551539e-06
w_2	-1.103525303929862e-03	4.278440632676324e-09

The nodal regression rate used for the torus was -1.10352532368809e-03 rad/TU.

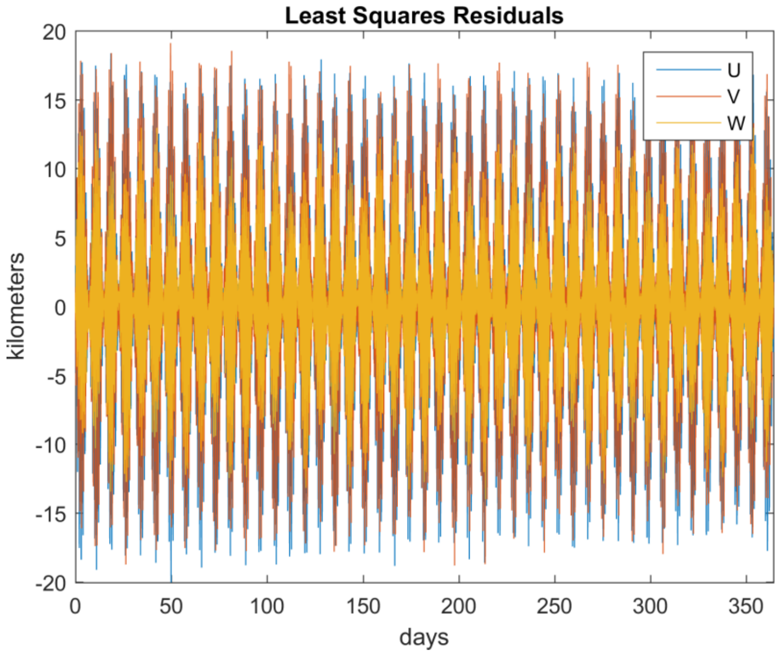

Figure 20. Delta 114 Vectors to Torus Action-Angle Least Squares Residuals

Large residuals from the least squares orbit fitting software indicate the SGP4 vectors did not fit well to the surface of the torus. The torus action-angle variables from this fit are a poor representation of the orbit and considered invalid. No further data was collected for this test case.

GOES-9 Results

Table 9. GOES-9 TLE Curve Fit Results

Angle	a_0 (rad)	a_1 (rad/TU)	a_2 (rad/TU^2)
Ω	8.306288025486594e-03	-1.804103127379547e-06	2.658400119870909e-10
ω	2.864403810083728e-03	2.564041341910887e-05	8.230356394557856e-08
M	5.769707985547703e-02	5.794617040746732e-02	-8.280782489298334e-08

Note. Curve fit of the form $X = a_0 + a_1 t + a_2 t^2$

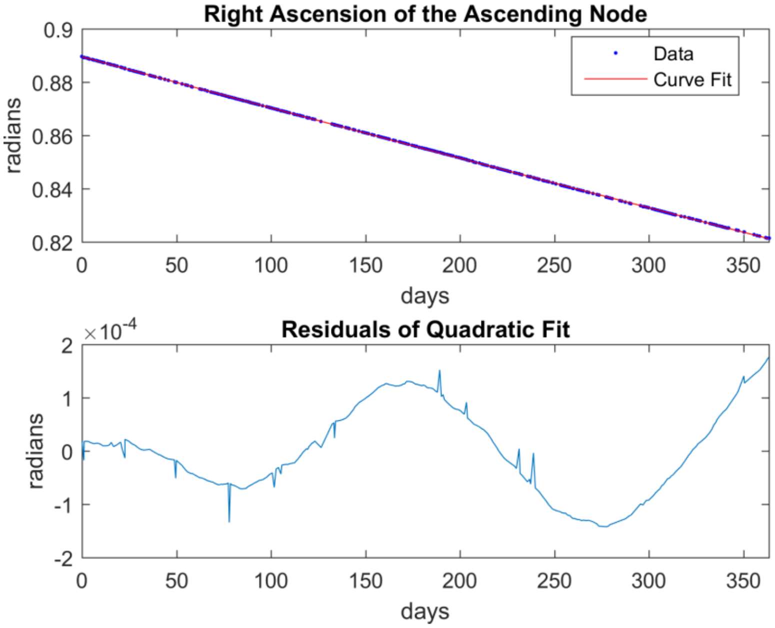

Figure 21. GOES-9 Right Ascension of the Ascending Node Curve Fit and Residuals

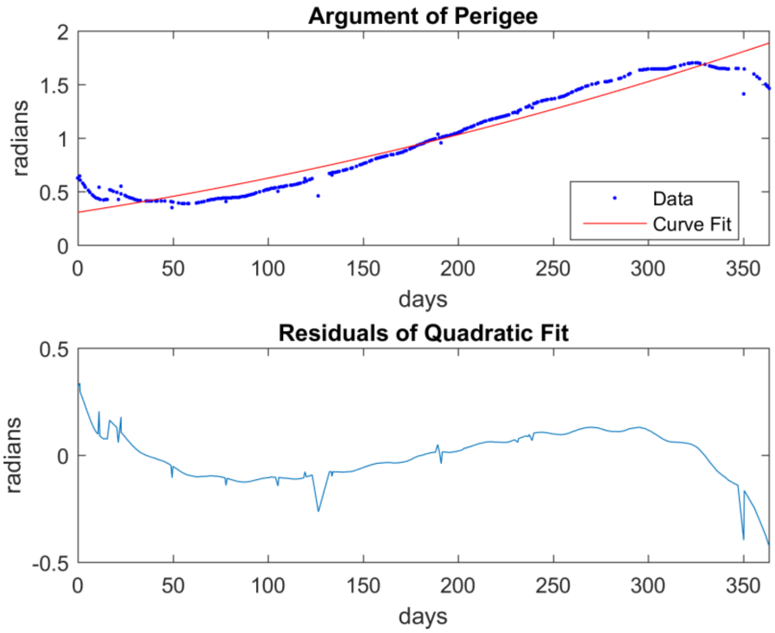

Figure 22. GOES-9 Argument of Perigee Curve Fit and Residuals

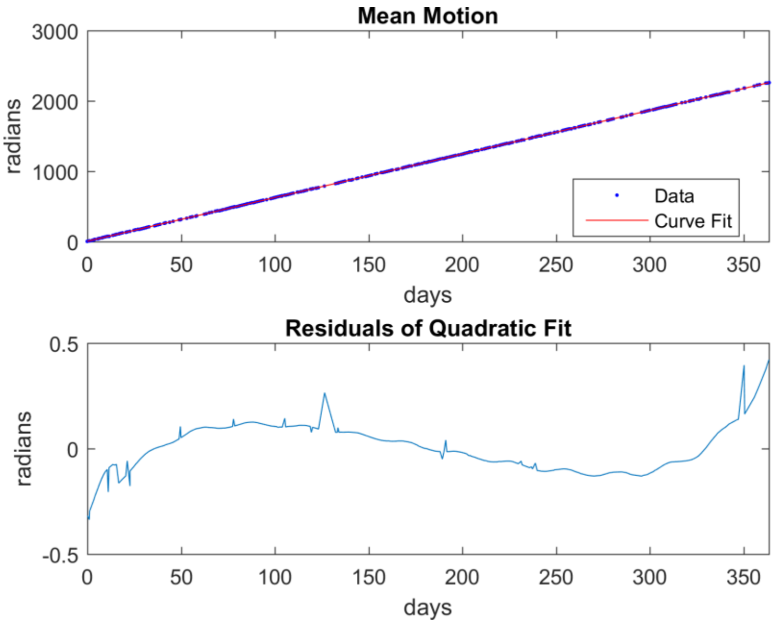

Figure 23. GOES-9 Mean Motion Curve Fit and Residuals

Table 10. GOES-9 Torus Basis Frequencies and Error

	Frequency (rad/TU)	± Error (rad/TU)
w_1	5.797181082088643e-02	4.265789282743295e-06
w_2	-1.804103127379547e-06	1.555111658141705e-09

Torus construction failed for the GOES-9 test case. No further data was collected for this test case.

Iridium 33 Debris Results

Table 11. Iridium 33 Debris TLE Curve Fit Results

Angle	a_0 (rad)	a_1 (rad/TU)	a_2 (rad/TU^2)
Ω	1.559474876829538e-02	-6.869113440559658e-05	-1.067517117562366e-09
ω	3.108816376446168e-02	-5.212606617146095e-04	-1.055160329396633e-08
M	3.223578156805461e-02	8.343064294416605e-01	5.270321967360674e-06

Note. Curve fit of the form $X = a_0 + a_1 t + a_2 t^2$

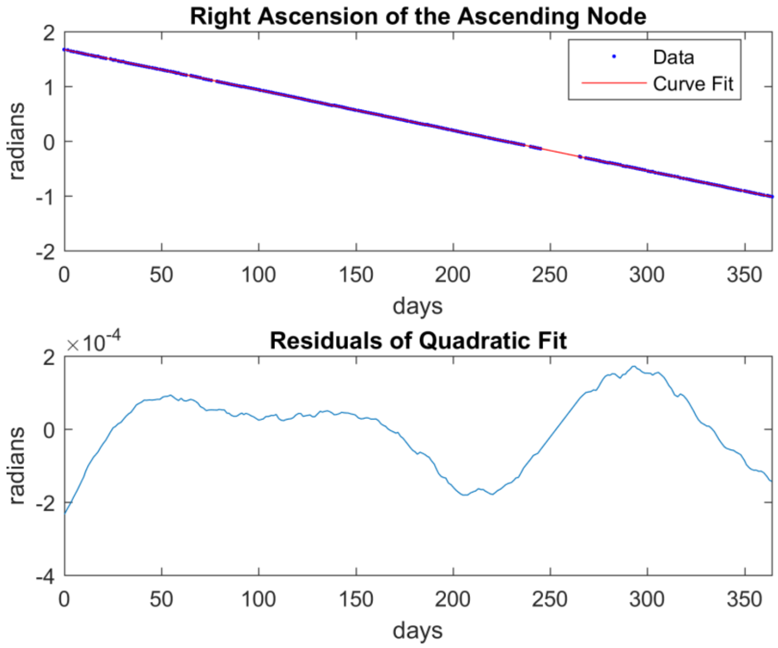
Right Ascension of the Ascending Node

Residuals of Quadratic Fit

Figure 24. I33 Debris Right Ascension of the Ascending Node Curve Fit and Residuals

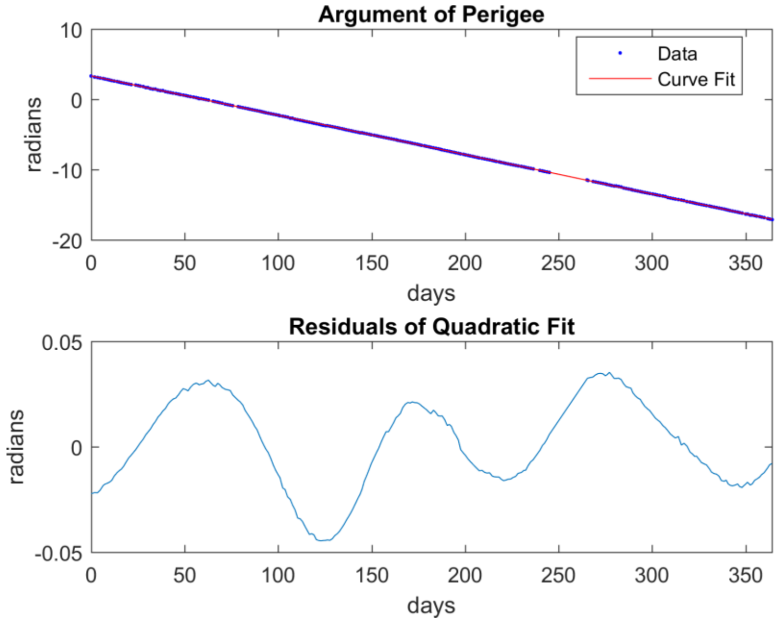
Argument of Perigee

Residuals of Quadratic Fit

Figure 25. I33 Debris Argument of Perigee Curve Fit and Residuals

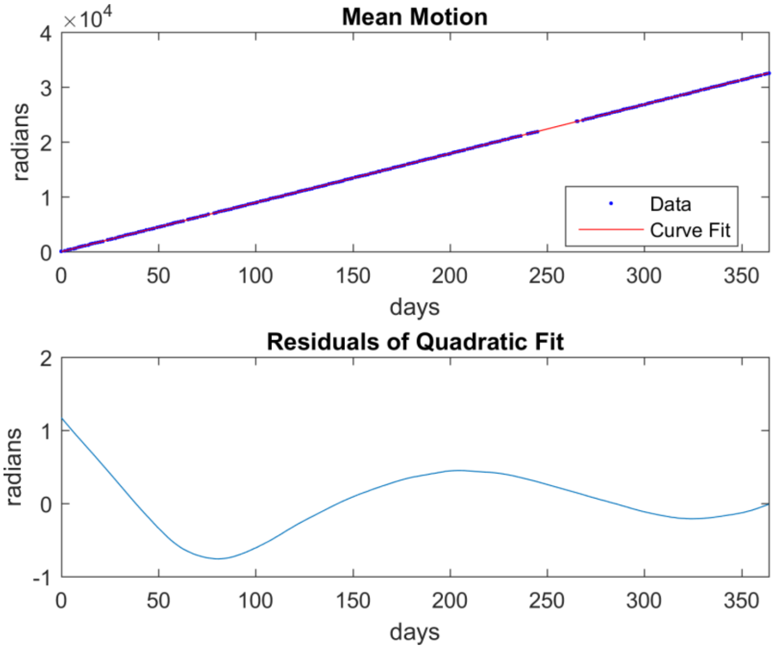

Figure 26. I33 Debris Mean Motion Curve Fit and Residuals

Table 12. Iridium 33 Debris Torus Basis Frequencies and Error

	Frequency (rad/TU)	± Error (rad/TU)
w_1	8.337851687799458e-01	9.372959316111540e-06
w_2	-6.869113440559658e-05	2.125088103220731e-09

The nodal regression rate used for the torus was -6.86911350750460e-05 rad/TU.

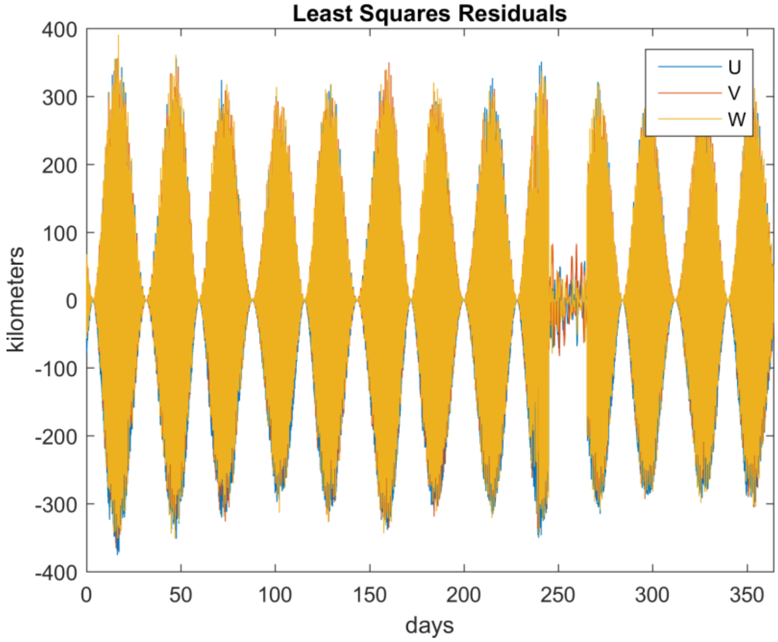

Figure 27. I33 Debris Vectors to Torus Action-Angle Least Squares Residuals

Large residuals from the least squares orbit fitting software indicate the SGP4 vectors did not fit well to the surface of the torus. The torus action-angle variables from this fit are a poor representation of the orbit and considered invalid. No further data was collected for this test case.

SL-14 Rocket Body Results

Table 13. SL-14 Rocket Body TLE Curve Fit Results

Angle	a_0 (rad)	a_1 (rad/TU)	a_2 (rad/TU^2)
Ω	2.550420838985319e-02	-1.696805309791247e-04	-6.319711037344882e-09
ω	4.876101343323117e-02	-5.899067935333994e-04	-4.420252504056470e-08
M	3.917328838329103e-03	9.083805904867033e-01	1.418456093475879e-05

Note. Curve fit of the form $X = a_0 + a_1 t + a_2 t^2$

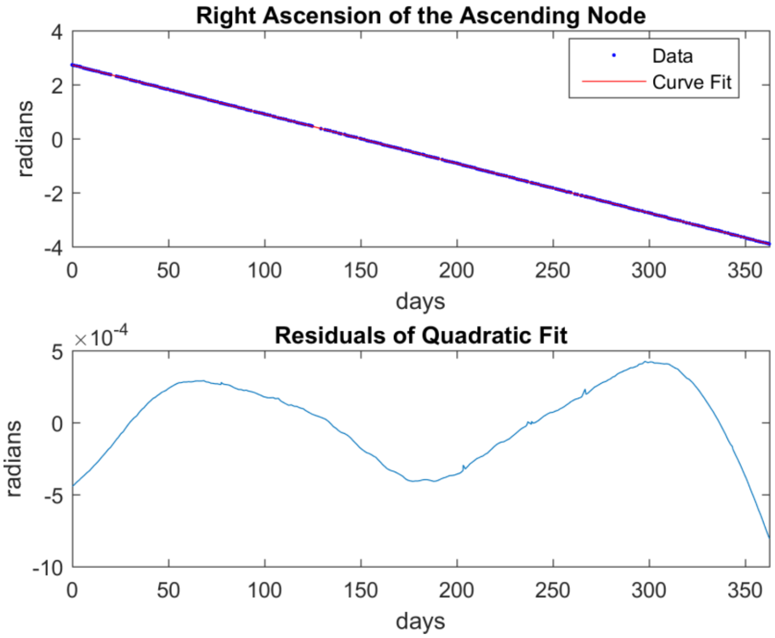

Figure 28. SL-14 Right Ascension of the Ascending Node Curve Fit and Residuals

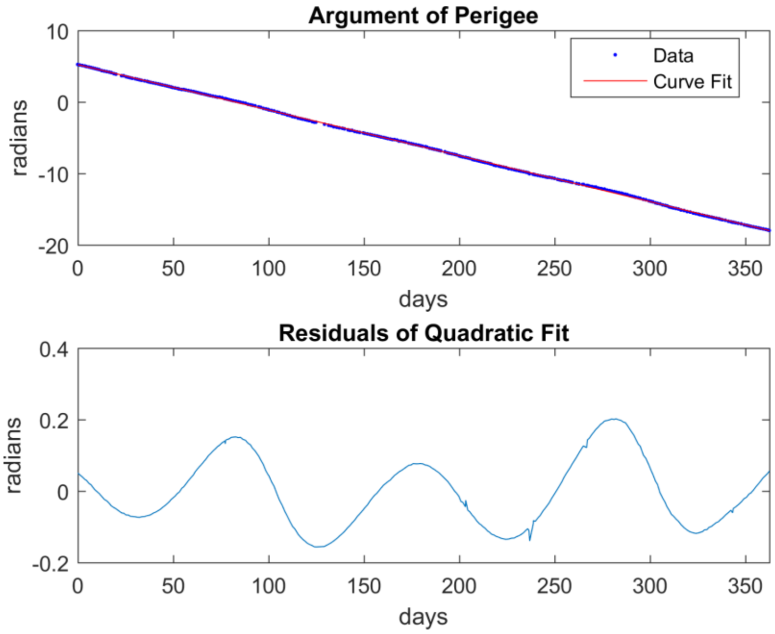

Figure 29. SL-14 Argument of Perigee Curve Fit and Residuals

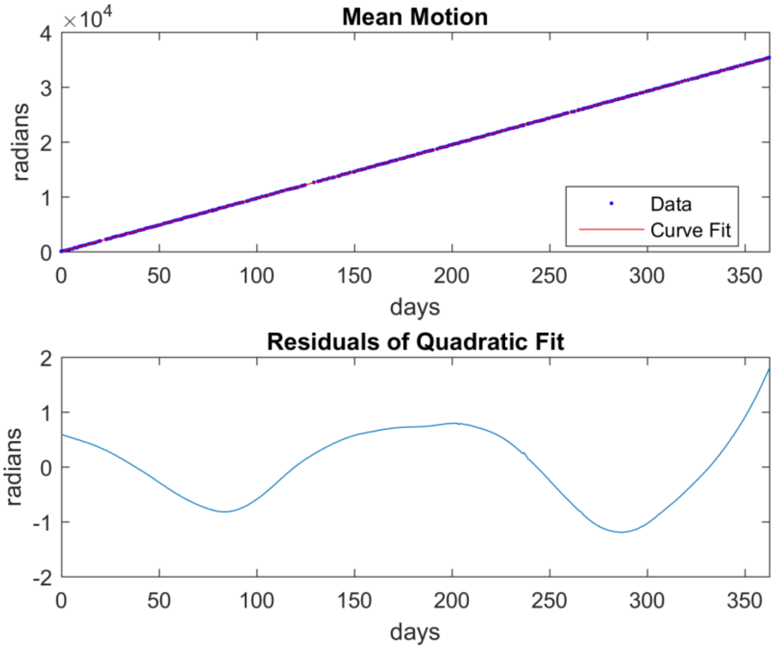

Figure 30. SL-14 Mean Motion Curve Fit and Residuals

Table 14. SL-14 Rocket Body Torus Basis Frequencies and Error

	Frequency (rad/TU)	± Error (rad/TU)
w_1	9.077906836931700e-01	1.585789863786196e-05
w_2	-1.696805309791247e-04	5.698164948718659e-09

The nodal regression rate used for the torus was -1.69680540178524e-04 rad/TU.

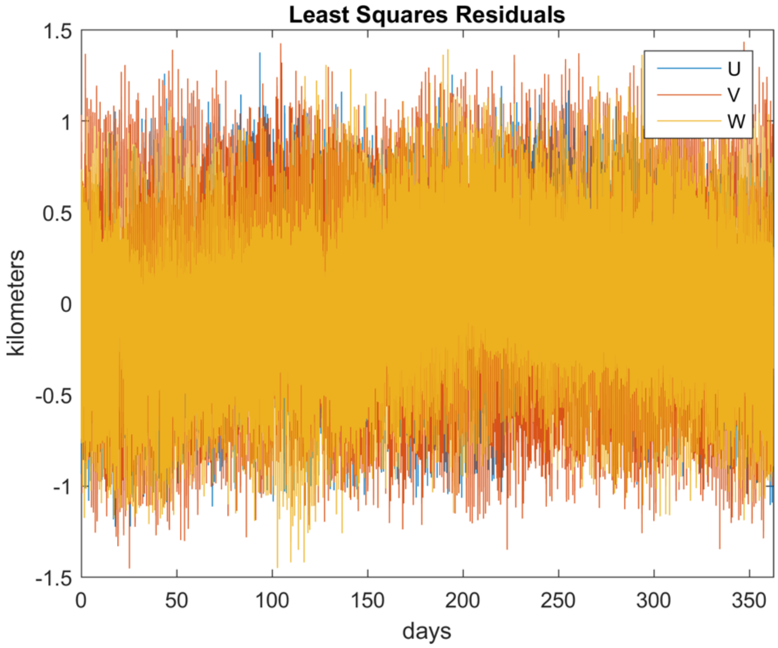

Figure 31. SL-14 Vectors to Torus Action-Angle Least Squares Residuals

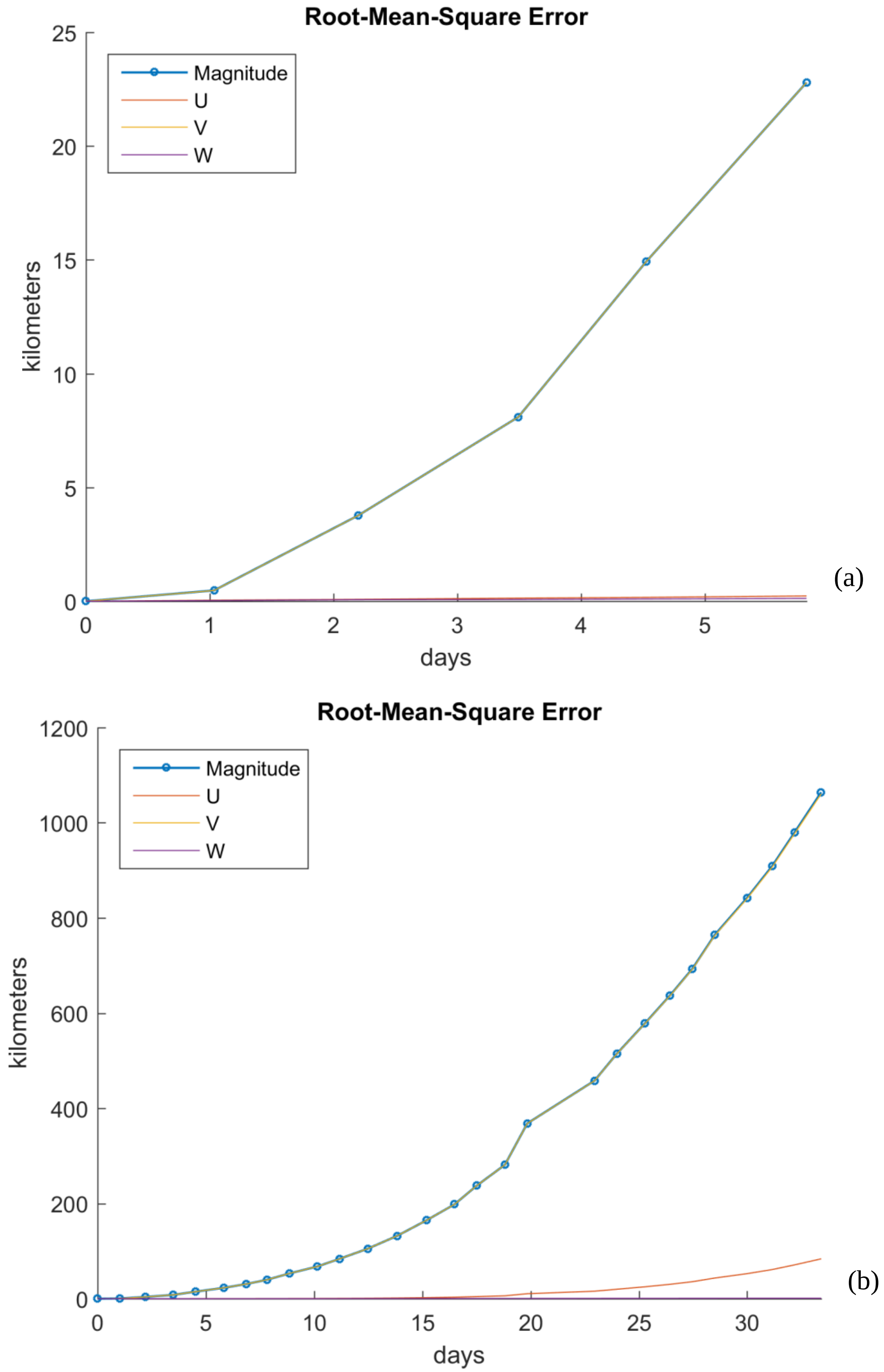

Figure 32. SL-14 RMSE: All TLEs Compared to First TLE

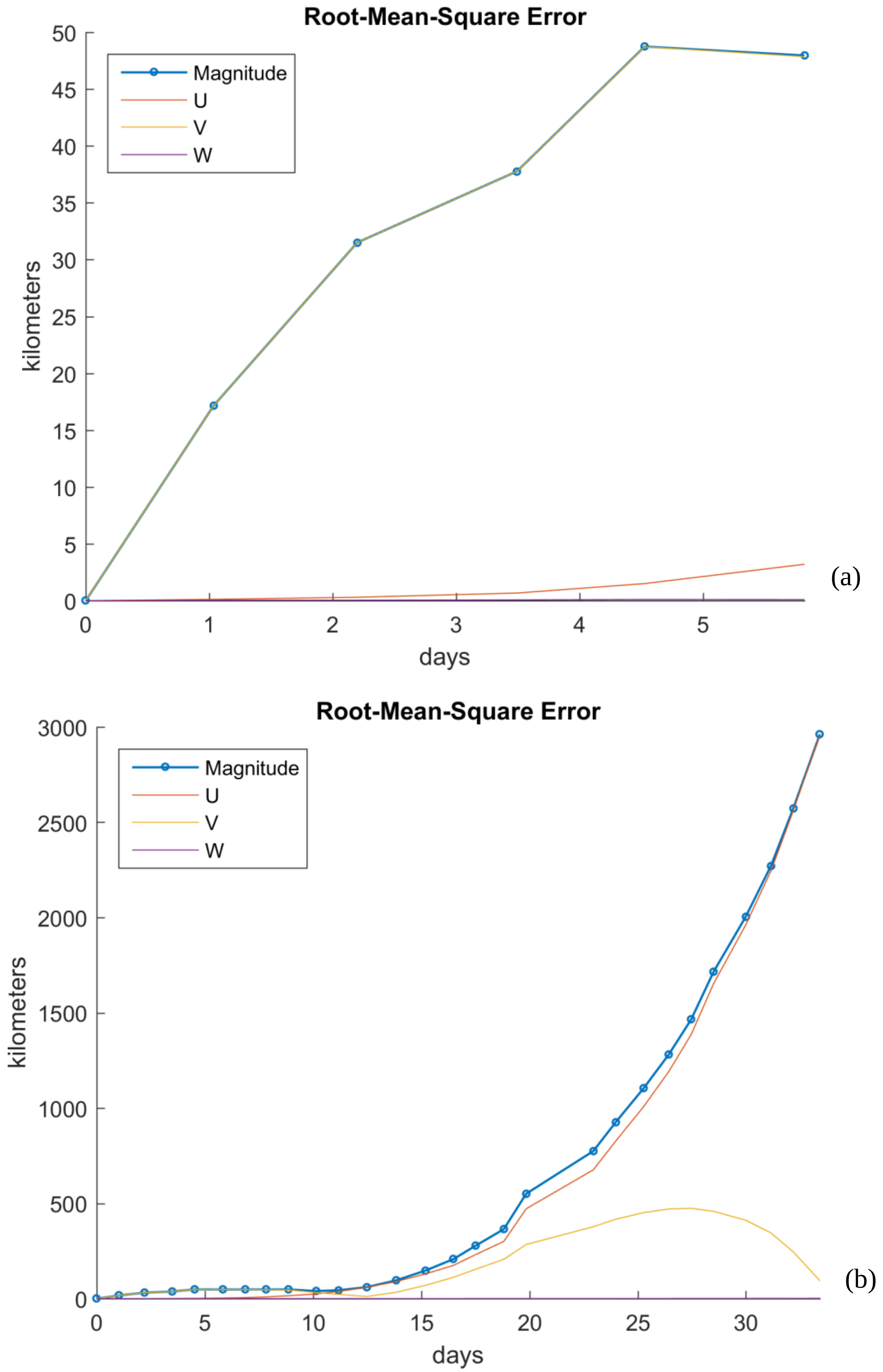

Figure 33. SL-14 RMSE: Updated Action-Angle Sets Compared to First Set

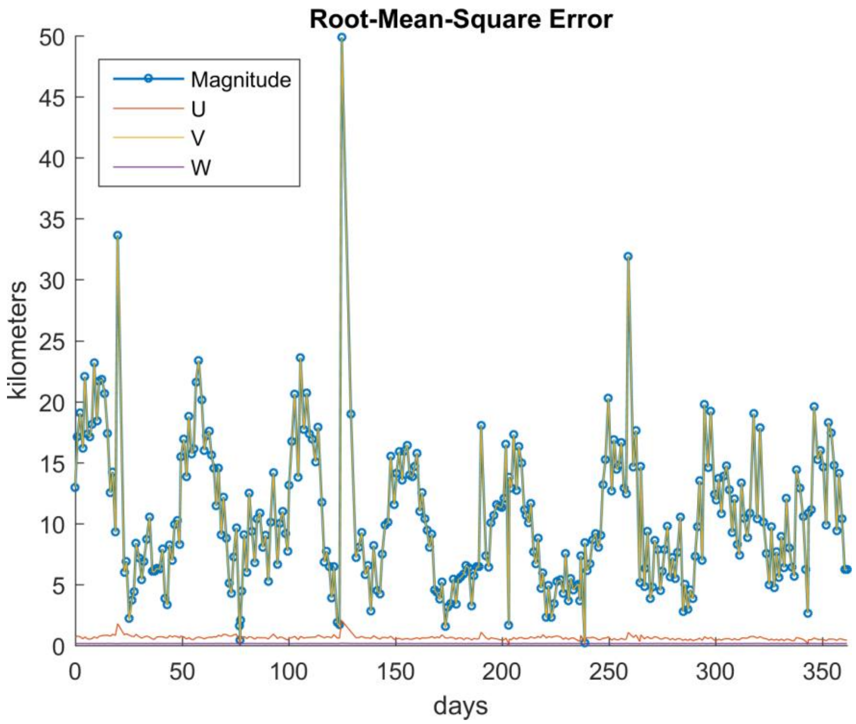

Figure 34. SL-14 RMSE: Updated Action-Angle Sets Compared to All TLEs

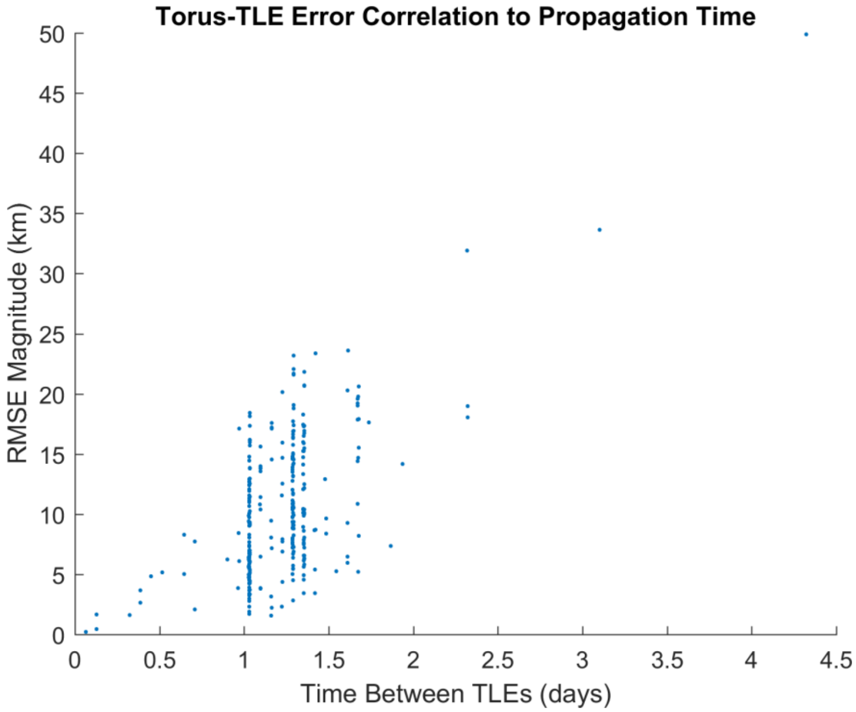

Figure 35. SL-14 Torus-to-TLE RMSE Correlation to Elapsed Time

Figure 32 (a) shows the SGP4 RMSE grows to 1 kilometers after 1.2 days, which occurs shortly after the epoch time of the second TLE in the set. The error reaches 5 kilometers at 2.6 days after the third TLE. Figure 33 (a) shows the torus RMSE grows beyond 5 kilometers after a matter of hours, reaching 17 kilometers with the first update to the action-angle variables. Figure 34 shows the RMSE between the torus and SGP4 models for each set of 100 vectors over the full year differ primarily in the in-track direction for all predictions with a mean in-track difference of 10.47 kilometers. The vectors differ by an average RMSE of 615 meters in the radial direction and 159 meters in the orbit-normal direction.

The SL-14 rocket body orbits at the lowest altitude of the three test cases with a valid torus model. Figure 35 shows the RMSE between the torus and SGP4 orbit models can reach as much as 20 kilometers over a one day period. Atmospheric drag is the most likely cause for this rapid divergence and may be the limiting factor affecting how well SGP4 position vectors will fit to the surface of the KAM torus. The R^2 coefficient of a linear fit through the data in Figure 43 is 0.377, indicating that the unpredictable atmospheric drag conditions greatly affect the divergence of the models.

SL-18 Rocket Body Results

Table 15. SL-18 Rocket Body TLE Curve Fit Results

Angle	a_0 (rad)	a_1 (rad/TU)	a_2 (rad/TU^2)
Ω	2.642468070258952e-02	1.692593162690922e-04	8.305364182764667e-09
ω	-1.794307885938283e-03	-5.831137479926340e-04	-4.431142126331949e-08
M	1.229010167779068e-02	9.008805514109712e-01	1.520471427642581e-05

Note. Curve fit of the form $X = a_0 + a_1 t + a_2 t^2$

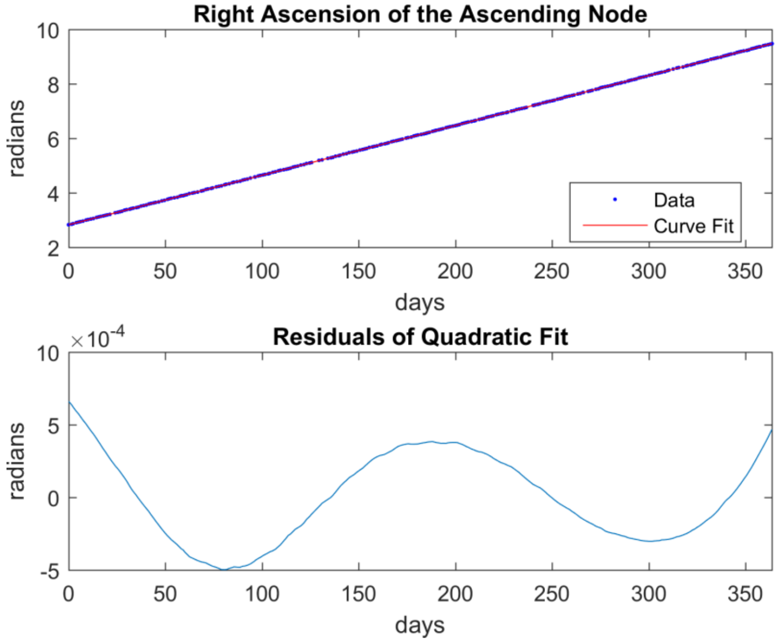

Figure 36. SL-18 Right Ascension of the Ascending Node Curve Fit and Residuals

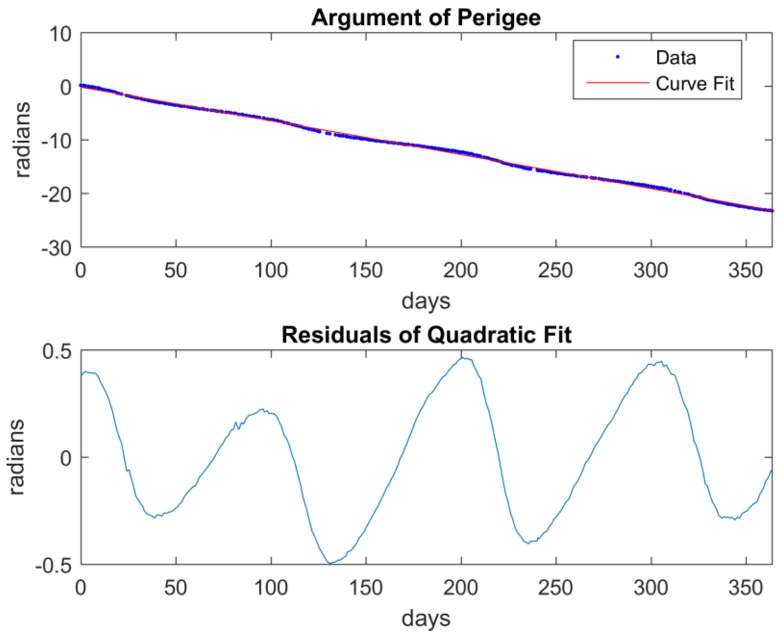

Figure 37. SL-18 Argument of Perigee Curve Fit and Residuals

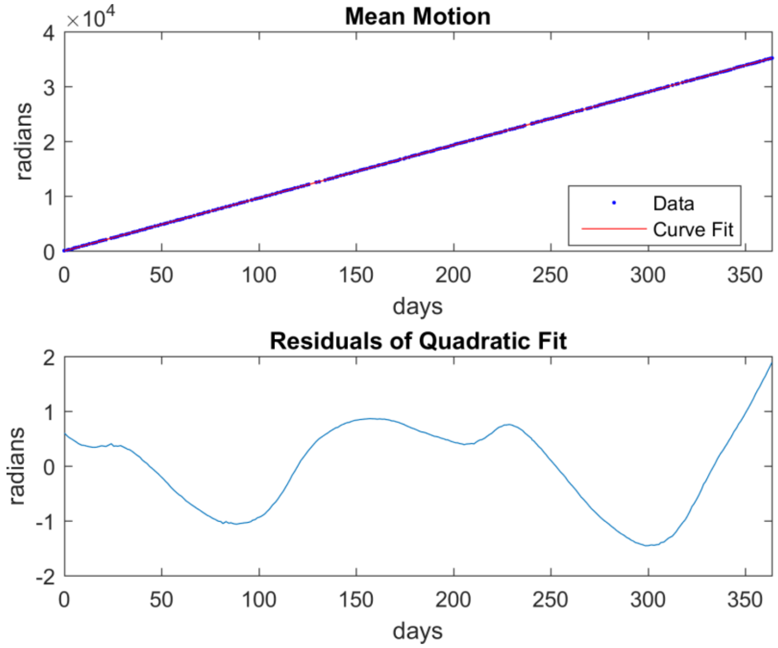

Figure 38. SL-18 Mean Motion Curve Fit and Residuals

Table 16. SL-18 Torus Basis Frequencies and Error

	Frequency (rad/TU)	± Error (rad/TU)
w_1	9.002974376629787e-01	2.196155792730019e-05
w_2	1.692593162690922e-04	6.233876829013437e-09

The nodal regression rate used for the torus was 1.69259318046536e-04 rad/TU.

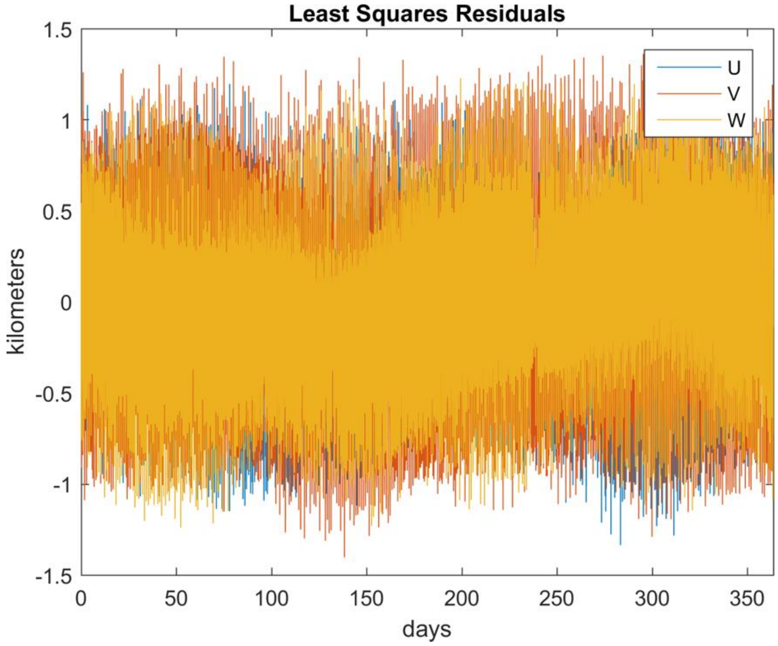

Figure 39. SL-18 Vectors to Torus Action-Angle Least Squares Residuals

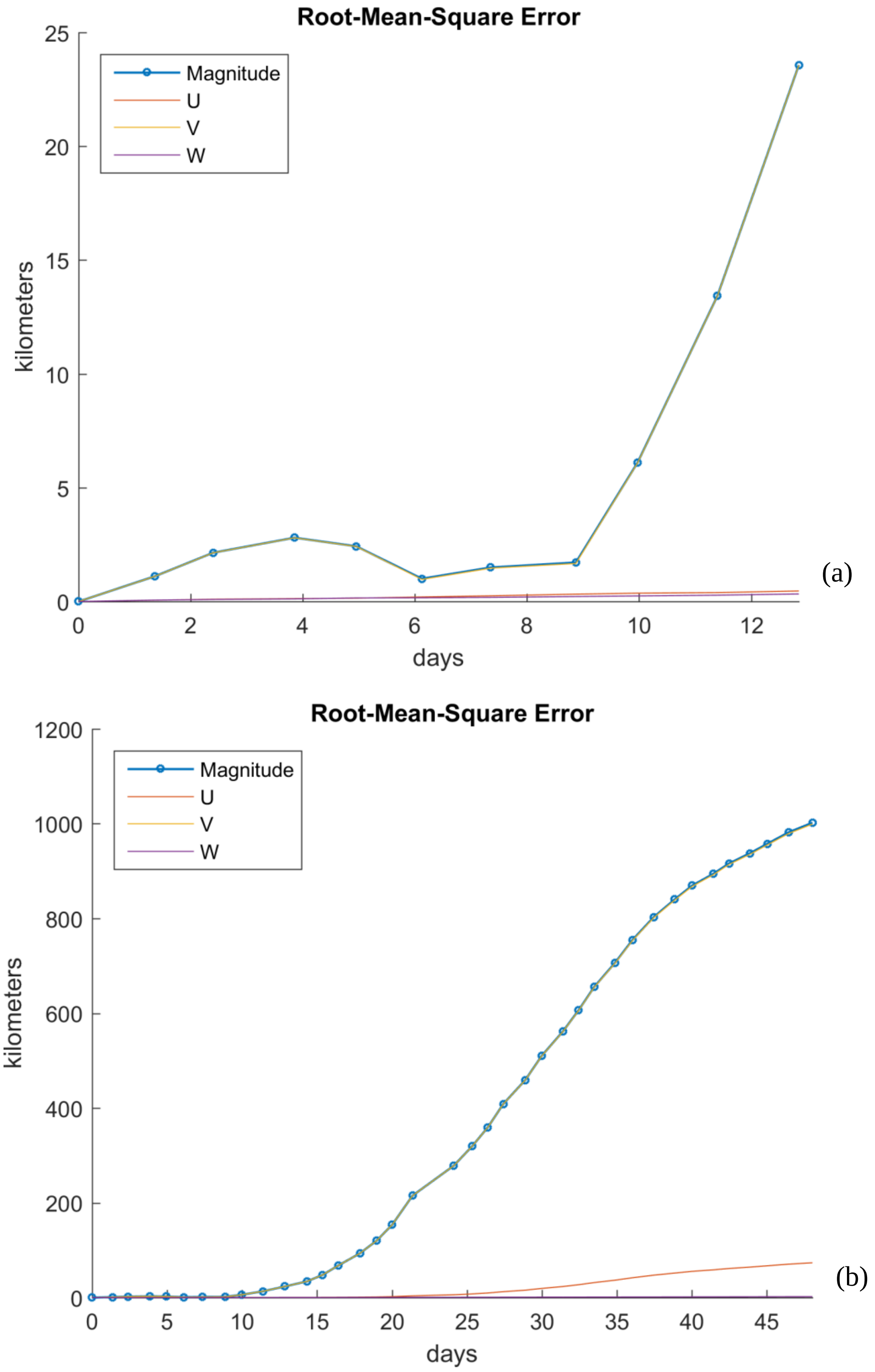

Figure 40. SL-18 RMSE: All TLEs Compared to First TLE

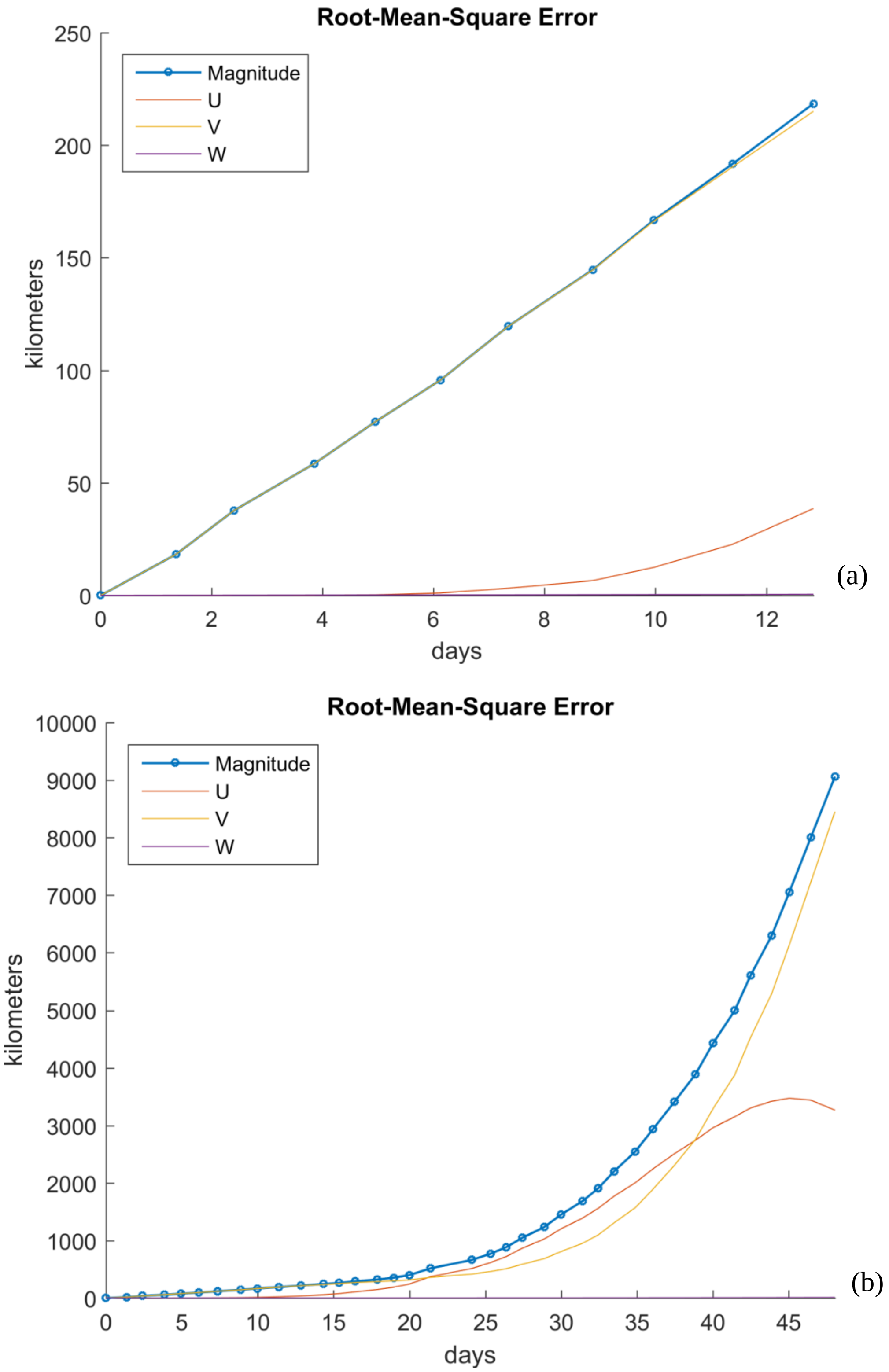

Figure 41. SL-18 RMSE: Updated Action-Angle Sets Compared to First Set

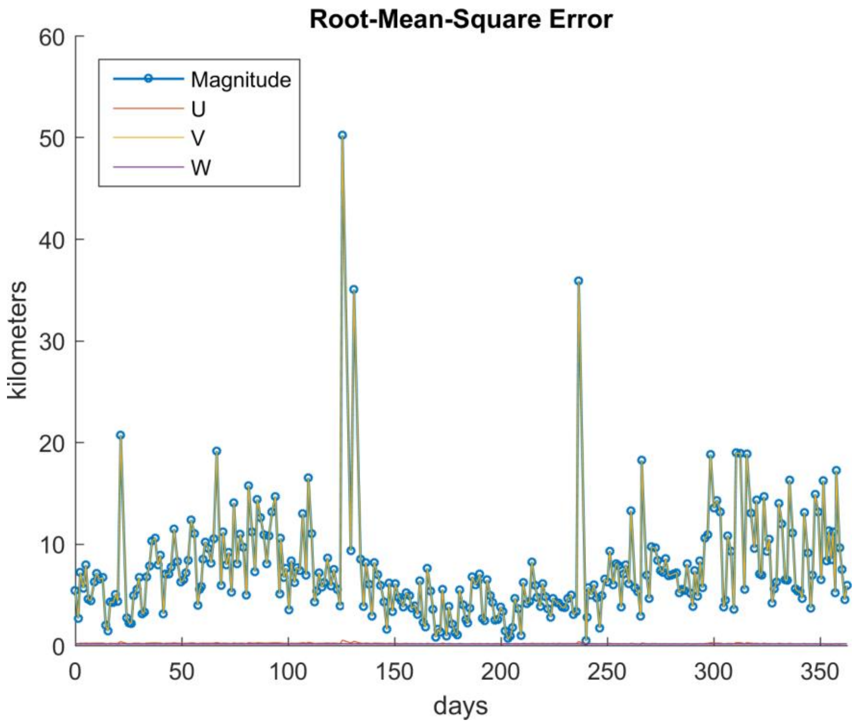

Figure 42. SL-18 RMSE: Updated Action-Angle Sets Compared to All TLEs

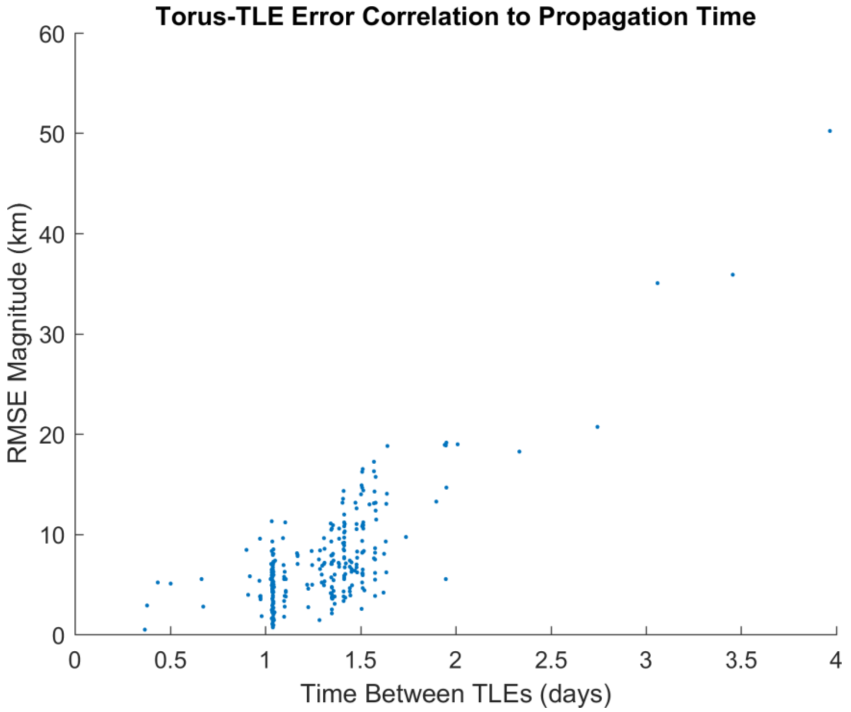

Figure 43. SL-18 Torus-to-TLE RMSE Correlation to Elapsed Time

Figure 40 (a) shows the SGP4 RMSE grows to 1 kilometers after 1.2 days, which occurs shortly after the epoch time of the second TLE in the set. The error reaches 5 kilometers at 9.7 days after the ninth TLE. Figure 41 (a) shows the torus RMSE grows beyond 5 kilometers after a matter of hours, reaching 17 kilometers with the first update to the action-angle variables. Figure 42 shows the RMSE between the torus and SGP4 models for each set of 100 vectors over the full year differ primarily in the in-track direction for all predictions with a mean in-track difference of 7.28 kilometers. The vectors differ by an average of 192 meters in the radial direction and 156 meters in the orbit-normal direction. The R^2 coefficient of a linear fit through the data in Figure 43 is 0.629. The correlation is not as strong as the Hubble RMSE correlation likely because the SL-18 rocket body is in a higher drag environment.

Thor 293 Rocket Body Results

Table 17. Thor 293 Rocket Body TLE Curve Fit Results

Angle	a_0 (rad)	a_1 (rad/TU)	a_2 (rad/TU^2)
Ω	1.826055416145551e-02	-8.369327449133814e-04	-3.432109406765128e-11
ω	1.404738190629151e-02	1.367514961815496e-03	-1.776467205688424e-11
M	4.497505790335756e-02	7.937256946477702e-01	1.237708899455352e-08

Note. Curve fit of the form $X = a_0 + a_1 t + a_2 t^2$

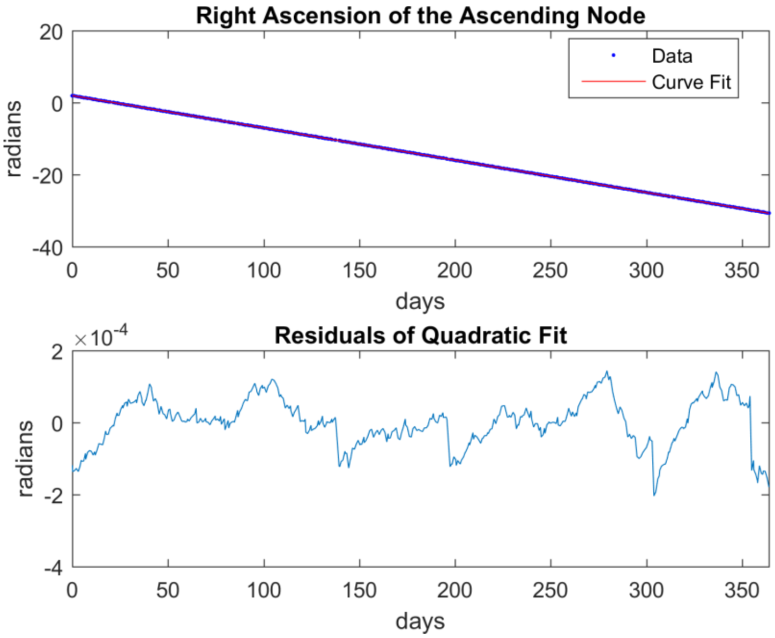

Figure 44. Thor 293 Right Ascension of the Ascending Node Curve Fit and Residuals

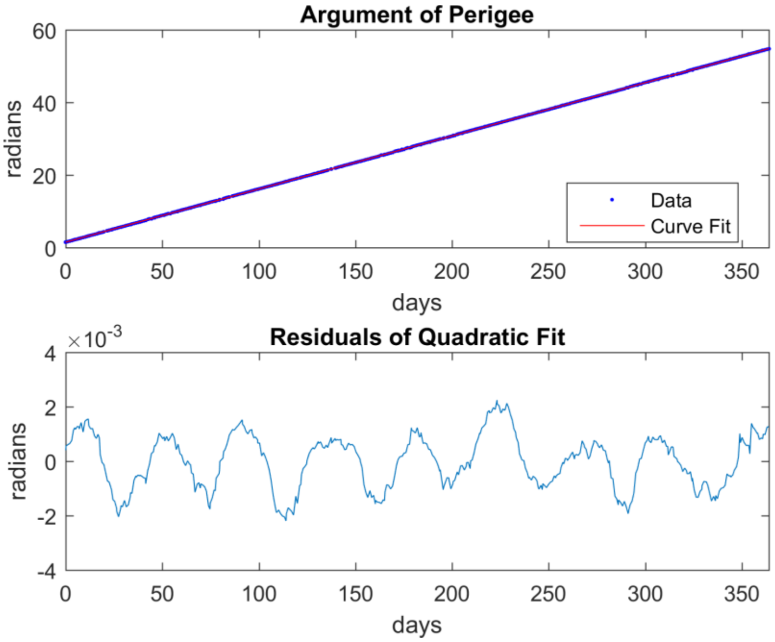

Figure 45. Thor 293 Argument of Perigee Curve Fit and Residuals

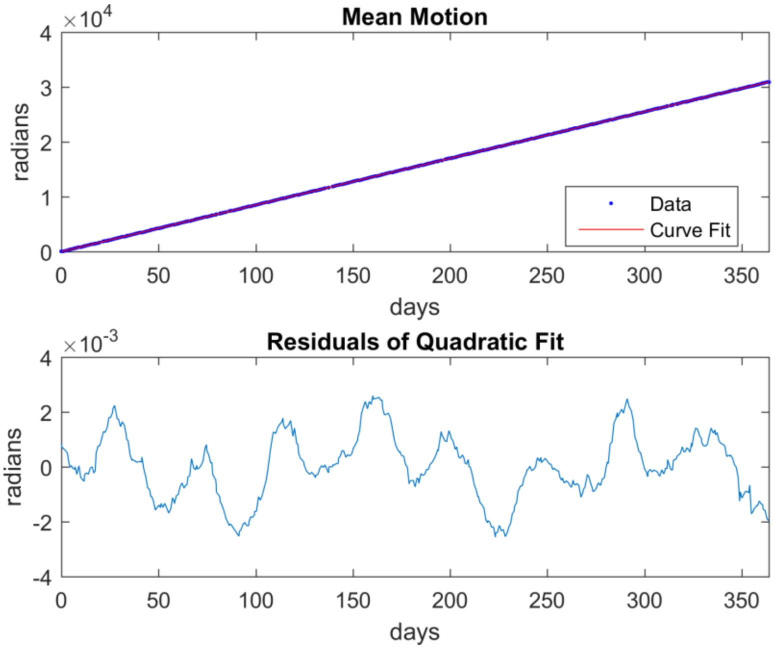

Figure 46. Thor 293 Mean Motion Curve Fit and Residuals

Table 18. Thor 293 Rocket Body Torus Basis Frequencies and Error

	Frequency (rad/TU)	± Error (rad/TU)
w_1	7.950932096095857e-01	3.456321706034434e-08
w_2	-8.369327449133814e-04	1.084015342511635e-09

Torus construction failed for the Thor 293 test case. No further data was collected for this test case.

Bibliography

1. Abay, R. (2014, March). *KAM Torus Orbit Prediction from Two Line Element Sets* (Master's thesis). Air Force Institute of Technology (AU), Wright-Patterson AFB OH. (AD-A596673)

2. Bonavito, N. L., Watson, J. S., & Walden, H. (1996). *An Accuracy and Speed Comparison of the Vinti and Brouwer Orbit Prediction Methods.* Goddard Space Flight Center.

3. Bordner III, R. E. (2010, September). *Orbital Tori Construction Using Trajectory Following Spectral Methods* (Doctoral dissertation). Air Force Institute of Technology (AU), Wright-Patterson AFB OH. (AD-A528586)

4. Celletti, A., & Chierchia, L. (2006). KAM tori for N-body problems: a brief history. *Celestial Mechanics and Dynamical Astronomy, 95*(1-4), 117-139. doi:10.1007/s10569-005-6215-x

5. Consultative Committee for Space Data Systems. (2013, June). Conjunction Data Message, Recommend Standard, BLUE BOOK. (CCSDS 508.0-B-1). Washington, DC. Retrieved from http://public.ccsds.org/publications/archive/508x0b1e1.pdf

6. Craft, C. T. (2007, September). *Formation Flight of Earth Satellites on KAM Tori* (Master's thesis). Air Force Institute of Technology (AU), Wright-Patterson AFB OH. (AD-A506247)

7. Delshams, A., & Gutiérrez, P. (1996). Effective stability and KAM theory. *Journal of Differential Equations, 128*(2), 415-490. doi:10.1006/jdeq.1996.0102

8. Derbis, R. M. (2008, March). *Modeling GPS Satellite Orbits Using KAM Tori* (Master's thesis). Air Force Institute of Technology (AU), Wright-Patterson AFB OH. (AD-A481056)

9. Dunk, A. B. (2014, March). *Applying KAM Theory to Highly Eccentric Orbits* (Master's thesis). Air Force Institute of Technology (AU), Wright-Patterson AFB OH. (AD-A599791)

10. *Fiscal Year 2016 National Security Space Hearing: Hearing before the Subcommittee on Strategic Forces, House of Representatives,* 114th Cong. 1 (2015, March 25). Retrieved from http://docs.house.gov/Committee/Calendar/ByEvent.aspx?EventID=103106

11. *Fiscal Year 2017 National Security Space Hearing: Hearing before the Subcommittee on Strategic Forces, House of Representatives*, 114th Cong. 1 (2016, March 15). Retrieved from http://docs.house.gov/Committee/Calendar/ByEvent.aspx?EventID=104620

12. Flohrer, T., Krag, H., Klinkrad, H. (2008, September 17-19). *Assessment and Categorization of TLE Orbit Errors for the US SSN Catalogue*. Presented at the Advanced Maui Optical and Space Surveillance Technologies Conference. Wailea, Maui, HI.

13. Frey, G. (2011, March). *KAM Torus Frequency Generation from Two-Line Element Sets* (Master's thesis). Air Force Institute of Technology (AU), Wright-Patterson AFB OH. (AD-A539261)

14. Greenwood, D.T. (1997). *Classical Dynamics*. Mineola, NY: Dover Publications.

15. Hagen, L. J. (2011, March). *Effects of Air Drag and Lunar Third-Body Perturbations on Motion Near a Reference KAM Torus* (Master's thesis). Air Force Institute of Technology (AU), Wright-Patterson AFB OH. (AD-A539443)

16. Hoots, F. R., Schumacher, P. W., & Glover, R. A. (2004). History of analytical orbit modeling in the U. S. space surveillance system. *Journal of Guidance, Control, and Dynamics, 27*(2), 174-185. doi:10.2514/1.9161

17. Joint Chiefs of Staff. (2013, May 29). *Space Operations*. (JP 3-14). Retrieved from http://www.dtic.mil/doctrine/new_pubs/jp3_14.pdf

18. Kelso, T. S. (2014, May 17). *Satellite Times: Frequently Asked Questions: Two-Line Element Set Format*. Retrieved from CelesTrak: https://celestrak.com/columns/v04n03/

19. Kelso, T. S. (2014, May 17). *Satellite Times: More Frequently Asked Questions*. Retrieved from CelesTrak: https://celestrak.com/columns/v04n05/

20. Kessler, D. J., & Cour-Palais, B. G. (1978). Collision frequency of artificial satellites: The creation of a debris belt. *Journal of Geophysical Research, 83*(A6), 2637-2646. doi:10.1029/JA083iA06p02637

21. Little, B. D. (2009, March). *Application of KAM Theorem to Earth Orbiting Satellites* (Master's thesis). Air Force Institute of Technology (AU), Wright-Patterson AFB OH. (AD-A496753)

22. Lyddane, R. H. (1963, October). Small eccentricies or inclinations in the Brouwer theory of the artificial satellite. *The Astronomical Journal, 68*(8), 555-558. doi:10.1086/109179

23. Matney, M., Anz-Meador, P., & Foster, J. (2004). Covariance correlations in collision avoidance probability calculations. *Advances in Space Research, 34*(5), 1109-1114. doi:10.1016/j.asr.2003.11.012

24. McCain, J., & Reed, J. (2015, October 8). *Space Situational Awareness: Status of Efforts and Planned Budgets*. (GAO-16-6R). Washington, DC. Retrieved from Government Accountability Office website http://www.gao.gov/products/GAO-16-6R

25. NASA. (2016, July 27). *Space Debris and Human Spacecraft*. (M. Garcia, Editor) Retrieved July 28, 2016, from http://www.nasa.gov/mission_pages/station/news/orbital_debris.html

26. National Research Council. (2012). *Continuing Kepler's Quest: Assessing Air Force Space Command's Astrodynamics Standards.* Washington, DC: The National Academic Press. doi:10.17226/13456

27. Osweiler, V. P. (2006). *Covariance Estimation and Autocorrelation of NORAD Two-Line Element Sets* (Master’s thesis). Air Force Institute of Technology (AU), Wright-Patterson AFB OH. (AD-A446817)

28. Ott, E. (2002). *Chaos in Dynamical Systems* (2nd ed.). College Park, MD: Cambridge University Press.

29. Regan, F. J., & Anandakrishnan, S. M. (1993). *Dynamics of Atmospheric Re-Entry*. Washington, DC: American Institute of Aeronautics and Astronautics, Inc.

30. Tegler, E. (2016, April 6). How the “Space Fence” will help keep orbital junk from killing satellites. *Popular Mechanics*. Retrieved from http://www.popularmechanics.com/space/satellites/a20285/air-force-space-fence-telescope-2018/

31. U.S. Strategic Command. (2014, January). *USSTRATCOM Space Control and Space Surveillance*. Retrieved July 28, 2016, from https://www.stratcom.mil/factsheets/11/Space_Control_and_Space_Surveillance/

32. Vallado, D. A. (2013). *Fundamentals of Astrodynamics and Applications* (4th ed.). Hawthorne, CA: Microcosm Press.

33. Vallado, D. A., Crawford, P., Hujsak, R., & Kelso, T. S. (2006, August 21-24). *Revisiting Spacetrack Report #3: Rev 2*. Presented at the AIAA/AAS Astrodynamics Specialist Conference. Keystone, CO. doi:10.2514/6.2006-6753

34. Vinti, J. P. (1959). New method of solution for unretarded satellite orbits. *Journal of Research of the National Bureau of Standards, 62B*(2), 105-116. doi:10.6028/jres.063B.012

35. Vinti, J. P. (1998). *Orbital and Celestial Mechanics.* Progress in Astronautics and Aeronautics (Vol. 177). Reston, VA: American Institute of Aeronautics and Astronautics, Inc. doi:10.2514/4.866487

36. Wagner, J. W. (2014, July). Beware the Situation: How JSpOC Tracks Space Debris. *Room*, *The Space Journal*. Retrieved from https://room.eu.com/article/Beware_the_situation_how_JSpOC_tracks_space_debris

37. Wiesel, W. E. (2008). Earth satellite orbits as KAM tori. *Journal of the Astronautical Sciences*, *56*(2), 151-162. doi:10.007/BF03256546

38. Wiesel, W. E. (2010). *Modern Astrodynamics* (2nd ed.). Beavercreek, OH: Aphelion Press.

39. Wiesel, W. E. (2010). *Modern Orbit Determination* (2nd ed.). Beavercreek, OH: Aphelion Press.

40. Wiesel, W. E. (2011). Earth satellite perturbation theories as approximate KAM tori. *Journal of the Astronautical Sciences*, *58*(2), 153-165. doi:10.007/BF03321163

41. Wiesel, W. E. (2014). A theory of low eccentricity Earth satellite motion. *Journal of the Astronautical Sciences*, *59*(4), 629-649. doi:10.1007/s40295-014-0007-z

42. Wright, S. P. (2016). *Orbit Determination Using Vinti's Solution* (Doctoral dissertation). Air Force Institute of Technology (AU), Wright-Patterson AFB OH.

43. Yates, M. W. (2011, March). *Stochastic Orbit Prediction Using KAM Tori* (Master’s thesis). Air Force Institute of Technology (AU), Wright-Patterson AFB OH. (AD-A540280)

Vita

Captain Kenneth J. Stuart graduated in May 2012 from Embry-Riddle Aeronautical University in Prescott, Arizona, where he graduated Cum Laude with dual Bachelor of Science degrees in Aerospace Engineering and Mechanical Engineering. Captain Stuart also received minors in Mathematics and Defense Studies. He received his commission through Detachment 28 Air Force Reserve Officer Training Corps upon graduation from Embry-Riddle. Captain Stuart then earned a Master of Business Administration degree in Project Management from Columbia Southern University in July 2015.

Captain Stuart's first assignment was at Cape Canaveral Air Force Station, Florida, in the 45th Launch Support Squadron where he served as a Spacecraft Responsible Engineer overseeing pre-launch preparations for Advanced Extremely High Frequency, Global Positioning System, Mobile User Objective System, Space-Based Infrared System, and Wideband Global Satellite Communications satellites.

In August 2015, Captain Stuart entered the Graduate School of Engineering and Management, Air Force Institute of Technology. Upon graduation, Captain Stuart will be assigned to the Remote Sensing Systems Directorate of the Space and Missiles Systems Center, Los Angeles Air Force Base, California.

REPORT DOCUMENTATION PAGE

Form Approved
OMB No. 0704-0188

1. REPORT DATE *(DD-MM-YYYY)* 23-03-2017	**2. REPORT TYPE** Master's Thesis	**3. DATES COVERED** *(From - To)* August 2015 – March 2017

4. TITLE AND SUBTITLE KAM Tori from Two-Line Element Sets: A Comparison to SGP4	**5a. CONTRACT NUMBER** **5b. GRANT NUMBER** **5c. PROGRAM ELEMENT NUMBER**
6. AUTHOR(S) Stuart, Kenneth J., Captain, USAF	**5d. PROJECT NUMBER** **5e. TASK NUMBER** **5f. WORK UNIT NUMBER**
7. PERFORMING ORGANIZATION NAME(S) AND ADDRESS(ES) Air Force Institute of Technology Graduate School of Engineering and Management (AFIT/ENY) 2950 Hobson Way, Building 640 Wright-Patterson AFB OH 45433-7765	**8. PERFORMING ORGANIZATION REPORT NUMBER** AFIT-ENY-MS-17-M-293
9. SPONSORING / MONITORING AGENCY NAME(S) AND ADDRESS(ES) Intentionally Left Blank	**10. SPONSOR/MONITOR'S ACRONYM(S)** **11. SPONSOR/MONITOR'S REPORT NUMBER(S)**

12. DISTRIBUTION / AVAILABILITY STATEMENT

DISTRIBUTION STATEMENT A. APPROVED FOR PUBLIC RELEASE; DISTRIBUTION UNLIMITED.

13. SUPPLEMENTARY NOTES

This material is declared a work of the U.S. Government as is not subject to copyright protection in the United States.

14. ABSTRACT

Simplified General Perturbations 4 (SGP4), the current analytical model for daily tracking of objects in Earth orbit, provides at best kilometer-level accuracy with an average error growth of 1 to 3 kilometers per day. An improved analytical model with increased accuracy is necessary to reliably track the ever-growing number of objects in Earth orbit. This research examines if a Kolmogorov-Arnold-Moser (KAM) torus constructed from SGP4 two-line element (TLE) sets provides a more consistent orbit prediction than SGP4. One year of TLEs are processed as pseudo observations to identify the time rate of change of orbital elements for eight objects in different Earth orbits. The rates are then used to calculate torus basis frequencies, and an attempt is made to construct a torus for each test case. A least squares algorithm is implemented to fit SGP4 position vectors to the surface of the derived torus. The orbit path along the surface of the torus is compared to the orbit produced by SGP4 via a root-mean-square analysis. The results show that KAM tori basis frequencies can be extracted from TLEs, but SGP4 position vectors are not valid sources of pseudo observation data for the KAM torus analytical model with the current methodology.

15. SUBJECT TERMS

KAM Torus, SGP4, Orbit Determination, Orbit Propagation, Perturbations

16. SECURITY CLASSIFICATION OF:			**17. LIMITATION OF ABSTRACT**	**18. NUMBER OF PAGES**	**19a. NAME OF RESPONSIBLE PERSON** Dr. William E. Wiesel, AFIT/ENY
a. REPORT U	**b. ABSTRACT** U	**c. THIS PAGE** U	UU	124	**19b. TELEPHONE NUMBER** *(include area code)* (937) 255-3636 x4312 william.wiesel@afit.edu

Standard Form 298 (Rev. 8-98)
Prescribed by ANSI Std. Z39.18